

Seismic and Electromagnetic  
Interferometry –  
Retrieval of the Earth's Reflection  
Response Using Crosscorrelation

**Proefschrift**

ter verkrijging van de graad van doctor  
aan de Technische Universiteit Delft,  
op gezag van de Rector Magnificus Prof. dr. ir. J.T. Fokkema,  
voorzitter van het College voor Promoties,  
in het openbaar te verdedigen,  
op maandag 10 december 2007 om 15.00 uur

door

Deyan DRAGANOV

geboren te Sofia, Bulgarije

*Dit proefschrift is goedgekeurd door de promotor:*

Prof. dr. ir. C.P.A. Wapenaar

*Samenstelling promotiecommissie:*

Rector Magnificus	voorzitter
Prof. dr. ir. C.P.A. Wapenaar,	Technische Universiteit Delft, promotor
Prof. dr. ir. G.E.W. Bauer,	Technische Universiteit Delft
Prof. dr. W.A. Mulder,	Technische Universiteit Delft
Prof. dr. ir. A. Gisolf,	Technische Universiteit Delft
Prof. dr. ir. A.J. Berkhout,	Technische Universiteit Delft
Drs. A. Verdel,	Shell International Exploration and Production
Dr. A. Curtis,	University of Edinburgh

Jan Thorbecke heeft als begeleider in belangrijke mate aan de totstandkoming van het proefschrift bijgedragen.

ISBN-978-90-9022528-9

Copyright ©2007, by D. Draganov, Delft University of Technology, Delft, The Netherlands.

All rights reserved. No part of this publication may be reproduced, stored in a retrieval system or transmitted in any form or by any means, electronic, mechanical, photocopying, recording or otherwise, without the prior written permission of the author.

**SUPPORT**

The research reported in this thesis was financially supported by the Netherlands Research Centre for Integrated Solid Earth Science ISES and by the Dutch Technology Foundation STW, applied science division of NWO, and the Technology Program of the Ministry of Economic Affairs (grant DTN.4915).

Cover: The amplitude spectrum of the transmission response from Figure 3.2(a) as it is seen in the temporal frequency domain.

Printed in The Netherlands by: Sieca Repro.



# Contents

---

<b>Table of Contents</b>	<b>iii</b>
<b>1 Introduction</b>	<b>1</b>
1.1 Why do we want to retrieve the reflection response? . . . . .	1
1.2 What are Seismic and Electromagnetic Interferometry? . . . . .	2
1.3 Outline of this thesis . . . . .	4
<b>2 Theory of Seismic and Electromagnetic Interferometry</b>	<b>7</b>
2.1 SI and EMI relations based on a two-way wavefield reciprocity	11
2.1.1 Reciprocity theorems . . . . .	11
2.1.2 SI relations for impulsive sources in an acoustic medium	16
2.1.3 SI relation for impulsive sources in an acoustic medium with a free surface . . . . .	22
2.1.4 SI relation for transient sources in acoustic medium .	22
2.1.5 SI relation for noise sources in acoustic medium . .	23
2.1.6 SI relations for impulsive sources in an elastic medium	24
2.1.7 SI relation for impulsive sources in an elastic medium with a free surface . . . . .	33
2.1.8 SI relation for transient sources in an elastic medium	33
2.1.9 SI relation for noise sources in an elastic medium . .	34
2.1.10 EMI relations for impulsive sources . . . . .	35



2.1.11	EMI relations for transient sources . . . . .	41
2.1.12	EMI relations for noise sources . . . . .	42
2.2	SI relations based on a one-way wavefield reciprocity . . . . .	43
2.2.1	Reciprocity theorems . . . . .	43
2.2.2	SI relations for impulsive sources in an acoustic medium . . . . .	48
2.2.3	SI relation for transient sources in an acoustic medium . . . . .	51
2.2.4	SI relation for noise sources in an acoustic medium . . . . .	51
2.2.5	SI relations for a direct migration of noise recordings . . . . .	52
2.2.6	SI relations for impulsive sources in an elastic medium . . . . .	54
2.2.7	SI relation for transient sources in an elastic medium . . . . .	55
2.2.8	SI relation for noise sources in an elastic medium . . . . .	56
<b>3</b>	<b>Retrieval of the reflection response: numerical modelling results</b>	<b>59</b>
3.1	Retrieval of the acoustic reflection response . . . . .	61
3.1.1	Retrieval of the acoustic reflection response from recordings from transient subsurface sources . . . . .	61
3.1.2	Retrieval of the acoustic reflection response from recordings from white-noise subsurface sources . . . . .	77
3.2	Retrieval of the elastodynamic reflection response . . . . .	85
3.2.1	Retrieval of the elastodynamic reflection response from recordings from transient subsurface sources . . . . .	85
3.2.2	Retrieval of the elastodynamic reflection response from recordings from white-noise subsurface sources . . . . .	92
3.3	Retrieval of the electromagnetic reflection response . . . . .	96
<b>4</b>	<b>Retrieval of the seismic reflection response: application to laboratory and field data</b>	<b>101</b>
4.1	Application to laboratory data from transient sources . . . . .	102
4.2	Application to field data from background-noise sources . . . . .	111
<b>5</b>	<b>Conclusions</b>	<b>125</b>
	<b>Bibliography</b>	<b>129</b>
	<b>Summary</b>	<b>137</b>

CONTENTS

---

v

**Samenvatting** 141

**Acknowledgements** 145

**Curriculum Vitae** 147



# Introduction

---

## 1.1 Why do we want to retrieve the reflection response?

One of the goals in seismic exploration and in seismology is to obtain an image of the Earth's interior. This can be best achieved by using seismic reflection imaging. To obtain a good image, one requires high-quality seismic recordings from a regular and dense distribution of seismic sources. But it is not always possible to have a dense source distribution. The need to find new oil and gas fields has pushed exploration to new frontier areas where very limited exploration information is available. As a consequence, it is very costly to "shoot in the dark" with standard exploration sources (dynamite, vibrators, air guns) on a dense grid. Another problem arises when exploring in naturally sensitive areas, urban areas, or areas with very difficult surface terrain conditions, where the use of the active sources might be very limited or might not even be permitted due to the sources' destructive potential. In regional seismology, the problem with man-made seismic sources at the surface, when their use is desired for obtaining a higher-resolution image of

a subsurface structure, is even larger as the imaging of the deep subsurface structures requires very powerful sources.

The above-mentioned problems imply that certain areas of the Earth are not accessible for imaging or that we should look for alternative methods of obtaining seismic reflection recordings. Such an alternative is (passive) Seismic Interferometry, the subject of this thesis. It can be applied at all scales - laboratory, exploration, regional, and global (for the later see [Ruigrok \[2006\]](#)).

## 1.2 What are Seismic and Electromagnetic Interferometry?

In the most general sense, Seismic Interferometry (SI) can be defined as the process of generating new seismic or electromagnetic data from the cross-correlation of existing data. This possibility was first proposed by [Claerbout \[1968\]](#). He showed that for layered acoustic media, the reflection response at the free surface can be obtained from the autocorrelation of the observed passive transmission response at the free surface. He called this method Acoustic Daylight Imaging. Later, he conjectured that for a 3D medium, one should crosscorrelate the (passively acquired) seismic transmission responses at two points at the free surface to retrieve the seismic reflection response between these two points (as if one of the points acts as the source and the other as the receiver). This idea was first tested in the field by [Baskir and Weller \[1975\]](#), but the results were inconclusive. [Scherbaum \[1987a,b\]](#) and [Daneshvar et al. \[1995\]](#) applied the acoustic daylight imaging technique to seismological data. They autocorrelated earthquake records from several seismological stations to retrieve the reflection response, subsequently applied seismic inversion, and compared the inverted results with the geology inferred from standard seismological methods. The obtained results were encouraging. Since the late 1980s, the geophysical research group at Stanford started to investigate the possibility to apply the daylight imaging technique to exploration-scale data. Even though the application to real data did not deliver conclusive results [[Cole, 1995](#)], the modelling results gave very good insights into the type of passive white noise data that one should record [[Rickett and Claerbout, 1996](#); [Rickett, 1996](#)].

[Schuster \[2001\]](#) and [Schuster et al. \[2004\]](#) introduced the concept of Interferometric Imaging for the process of constructing a migrated seismic image from crosscorrelated results. Based on stationary-phase arguments, the authors showed that the method is applicable not only to passively acquired seismic noise data from subsurface noise sources, but also to conventional reflection data shot and recorded at the surface. Using a one-way reciprocity theorem of the correlation type, [Wapenaar et al. \[2002, 2004b\]](#) proved Claerbout's conjecture for any 3D inhomogeneous acoustic or elastic medium for both impulsive and white-noise sources, where the sources could be at depth or at the surface. [Berkhout and Verschuur \[2003, 2006\]](#) proposed a scheme for turning multiple reflections into primaries based on a weighted correlation process. [Slob et al. \[2006a,b\]](#) showed how one can retrieve electromagnetic recordings from crosscorrelation or crossconvolution of electromagnetic fields. They named this process Electromagnetic Interferometry (EMI). Later, the concept of retrieval of new responses through crosscorrelation was extended to any type of field [[Wapenaar et al., 2006](#)].

Independently, researchers in different fields of science started arriving at similar results. In the late 1980s and 1990s, Fink and his group introduced the concept of time-reversal acoustics. With this technique, an acoustic signal is emitted by a source and recorded at a receiver; then the recorded signal is reversed back in time and emitted from the location of the receiver to focus at the source point [[Fink et al., 1989](#); [Fink, 1992](#); [Draeger and Fink, 1997](#)]. They showed that a highly scattered field will focus at its origin when it is reversed in time and propagated back. Recently, they showed that this focusing results in images with super resolution (focal spots as small as one thirtieth of a wavelength [[Lerosey et al., 2007](#)]). The principle of time reversal was used by [Bakulin and Calvert \[2004\]](#) to develop a scheme for redatuming of surface reflection data, which scheme they called "virtual source method". Such redatuming methods are very close to the Common Focus Point (CFP) method [[Berkhout, 1997](#); [Thorbecke, 1997](#)], but here the Virtual Source method measures the CFP operator. [Weaver and Lobkis \[2001\]](#) and [Lobkis and Weaver \[2001\]](#) proved that the crosscorrelation of an acoustic diffuse wavefield, observed at two points, retrieves the Green's function (i.e, the impulse response) between these two points and demonstrated this with ultrasonic examples. [Campillo and Paul \[2003\]](#) applied this method to diffuse seismic coda waves and retrieved surface waves

arrivals between different seismological stations in Mexico. [Derode et al. \[2003\]](#) showed by physical reasoning how the time-reversal principle can be applied to retrieve the Green's function between two points. This result is very closely connected to Green's function retrieval through crosscorrelation since a crosscorrelation is nothing but a convolution of a signal with a second signal which is reversed in time. [Snieder \[2004, 2006\]](#) showed that the main contribution to the retrieved Green's function comes from sources around the stationary point. [Curtis et al. \[2006\]](#) showed the connection between the different methods in the different fields in a comprehensive way.

Because of the independent developments of the methods in the different fields, different names appeared for the same process of retrieval of a signal between two points from crosscorrelation or time reversal. Examples are: acoustic daylight imaging, Green's function retrieval, interferometric imaging, virtual source method, and passive seismics. To avoid confusion, the term "Seismic Interferometry" was adopted for a special issue of *Geophysics* (July-August, 2006) to describe the application of these methods to seismic exploration and seismology. Later, the term "Electromagnetic Interferometry" was adopted to describe the retrieval of electromagnetic fields for electromagnetic exploration.

### 1.3 Outline of this thesis

Chapter 2 gives the derivations of relations for SI and EMI. These derivations are based on two-way and one-way wavefield reciprocity relations of the correlation type.

Chapter 3 shows results from numerical modelling examples that serve to illustrate the SI and EMI relations and to investigate the applicability of SI and EMI relations to practical situations. Using finite-difference acoustic and finite-element elastic modelling codes, recordings at the surface were modelled from deterministic as well as noise sources in the subsurface. These recordings were then crosscorrelated in accordance with the derived SI and EMI relations to retrieve recordings at the surface as if from sources at the surface.

Chapter 4 shows the results from the application of the elastic SI relations to measured laboratory and field data. The showed results are extended versions of the results published by [Draganov et al. \[2007a\]](#) and [Draganov et](#)

[al. \[2007b\]](#). The laboratory data represent recordings from separate transient sources on an inhomogeneous granite sample. The field data were recorded in the Middle East and represent 2D surface recordings from noise sources. Chapter 5 gives conclusions based on the theoretical descriptions, the numerical tests and the laboratory and field-data examples.





# Theory of Seismic and Electromagnetic Interferometry

---

Seismic Interferometry (SI) relations can be derived using different theoretical bases. The starting point and the underlying theory for the derivation of a specific SI relation depends on the specific application it is intended for. In this chapter, SI relations are derived for the retrieval of Green's functions in an open system, based on seismic reciprocity theorems. Using electromagnetic reciprocity theorems, also Electromagnetic Interferometry (EMI) relations are derived. In general, a reciprocity theorem formulates a relation between two independent states of a domain - acoustic, elastic, or electromagnetic - in one and the same domain. A reciprocity relation can be formulated in terms of time-convolutions between the field quantities of the two states. Such a relation is called a convolution-type reciprocity theorem. A reciprocity relation can also be formulated in terms of time-correlations between the field quantities of the two states. In such a case, the relation is called a correlation-type reciprocity theorem.

The reciprocity theorems can describe relations between two-way wavefields or between one-way wavefields. Such relations are called two-way wavefield reciprocity theorems and one-way wavefield reciprocity theorems, respectively.

In section 2.1, following Wapenaar and Fokkema [2006], Slob et al. [2007], and Slob and Wapenaar [2007], derivations are presented of the SI and EMI relations using two-way wavefield reciprocity theorems. Section 2.2, following Wapenaar et al. [2004b], is dedicated to derivations of the SI relations using one-way wavefield reciprocity theorems. Even though the end results look very similar, there are some basic differences in the relations in the two sections, which make them useful in different practical applications.

The SI and EMI relations are derived under the assumption of a lossless medium. Of course in practice there are always losses in the medium. As shown by Slob et al. [2007]; Slob and Wapenaar [2007], in case of losses in the medium, the derived SI and EMI relations can still be used, but later arrivals, i.e., primaries and multiples with long travel paths, may not be reconstructed. Furthermore, as shown in Section 3.1.1, big losses in the medium may give rise to ghost events.

In both sections the derivations of the SI and EMI relations follow the same basic workflow:

- defining the system of two equations describing the wave propagation in a matrix-vector form;
- choosing an interaction quantity and deriving from it a reciprocity theorem;
- for each of the cases (acoustic, elastic, or electromagnetic) deriving the relationship for seismic (electromagnetic) interferometry in the case of
  - impulsive sources,
  - transient sources,
  - and noise sources.

The relations presented in this chapter are given in the frequency domain. A time-Fourier transform of a time- and space-dependent quantity is defined as  $\hat{\mathbf{u}}(\mathbf{x}, \omega) = \int_{t=0}^{\infty} \mathbf{u}(\mathbf{x}, t) e^{-j\omega t} dt$ , where  $\mathbf{x} = (x_1, x_2, x_3)$ . Throughout this

thesis, Einstein's summation convention applies to repeated lowercase Latin subscripts from 1 to 3, unless stated otherwise.

The list below describes in short all the symbols used in the this chapter in the order they appear in the text.

<u>Symbol</u>	<u>Meaning</u>
$\mathbb{D}$	Domain
$\partial\mathbb{D}$	Surface bounding the domain $\mathbb{D}$
$\mathbf{n} = n_m \mathbf{i}_m$	Outward-pointing vector normal to $\partial\mathbb{D}$ ; and the vectors $\mathbf{i}_m$ denote the base vectors of a Cartesian reference frame in a three-dimensional Euclidian space in the $m^{th}$ -direction.
$\mathbf{x} = x_m \mathbf{i}_m$	Cartesian coordinates vector (m)
$\rho$	Volume density of mass ( $\text{kg}/\text{m}^3$ )
$\kappa$	Compressibility ( $1/\text{Pa}=\text{m}^2/\text{N}$ )
$s_{pqkl}$	Compliance tensor ( $1/\text{Pa}$ )
$c_{ijkl}$	Stiffness tensor ( $\text{Pa}$ )
$\varepsilon_{kr}$	Electric permittivity ( $\text{s}/(\Omega \text{ m})$ )
$\mu_{ji}$	Magnetic permeability ( $\Omega \text{ s}/\text{m}$ )
$j$	Imaginary unit
$\omega$	Angular frequency ( $\text{rad}$ )
<b>u</b>	Wavefield vector
<b>s</b>	Source vector
<b>A</b>	Material properties matrix
<b>D</b>	Differentiation operator matrix
$p$	Acoustic pressure (Pa)
$v_i$	Particle velocity vector (m/s)
$\tau_{ij}$	stress tensor (Pa)
$E_r$	Electric field vector (V/m)
$H_i$	Magnetic field vector (A/m)
$q$	Source distribution in terms of density of volume injection rate (1/s)
$f_i$	Source distribution in terms of external volume density of force ( $\text{N}/\text{m}^3$ )

$h_{pq}$	Source distribution in terms of external deformation-rate density (1/s)
$J_k^e$	External source volume densities of electric currents (A/m <sup>2</sup> )
$J_j^m$	External source volume densities of magnetic currents (V/m <sup>2</sup> )
$\mathcal{A}, \mathcal{B}$	Two states of the domain $\mathbb{D}$
$\mathbf{K}$	Operator matrix = $diag(-1, 1)$
$T$	Vector or matrix transposition
$\delta_{ik}$	Kronecker delta function
$\Delta_{ijkl}$	= $\frac{1}{2} (\delta_{ik}\delta_{jl} + \delta_{jk}\delta_{il})$
$\epsilon_{kmi}$	The antisymmetric (Levi-Civita) tensor of rank three
$\mathbf{N}_x$	Operator matrix = $antidiag(n_i, n_i)$
$\dagger$	Vector or matrix complex conjugation and transposition
*	Complex conjugation
$G$	Green's function (1/m)
$\delta$	Dirac Delta function
$\Re$	Real part of a parameter
$c$	Propagation velocity (m/s)
$\alpha$	ray angle (degr)
$s$	Wavefield source
$S$	Source power spectrum
$F$	Shaping filter
$N$	Source noise spectrum
$c_P$	Propagation velocity for P-waves (m/s)
$c_S$	Propagation velocity for S-waves (m/s)
$\zeta_{ij}$	Inverse of the magnetic permeability (m/( $\Omega$ s))
$\xi_{ij}$	Inverse of the electric permittivity ( $\Omega$ m/s)
$\mathbf{P}$	Flux-normalized one-way wavefield quantity vector
$\mathbf{B}$	One-way pseudo-differential operator matrix
$\mathbf{S}$	Flux-normalized one-way source quantity vector
$\Lambda$	Vertical slowness operator matrix
$\Theta$	Vertical scattering operator matrix

<b>L</b>	Composition operator
<b>L</b> <sup>-1</sup>	Decomposition operator
<b>P</b> <sup>+(-)</sup>	Downgoing(upgoing) one-way wavefield
<b>S</b> <sup>+(-)</sup>	Downgoing(upgoing) one-way source field
<b>Φ</b> <sup>+(-)</sup>	Downgoing(upgoing) P-wave potential
<b>Ψ</b> <sup>+(-)</sup>	Downgoing(upgoing) S-wave potential
<b>N</b>	Operator matrix = <i>antidiag</i> (1, -1)
<b>J</b>	Operator matrix = <i>diag</i> (1, -1)
<b>R</b>	Flux-normalized reflection response of a medium
<b>T</b>	Flux-normalized transmission response of a medium
<b>r</b> <sup>-</sup>	Reflection coefficient of the free surface
<b>W</b> <sup>+(-)</sup>	Forward extrapolation operator
<b>R</b>	Flux-normalized reflection response matrix
<b>T</b>	Flux-normalized transmission response matrix
<b>r</b> <sup>-</sup>	Matrix with reflection coefficient of the free surface
<b>I</b>	Identity matrix
<b>F</b>	Shaping filter matrix
<b>N</b>	Noise spectra matrix

## 2.1 SI and EMI relations based on a two-way wavefield reciprocity

### ■ 2.1.1 Reciprocity theorems

Consider a 3D inhomogeneous, lossless medium with a bounded domain  $\mathbb{D}$  in it. Three different cases are looked at for the medium - acoustic, elastic, or electromagnetic. In the acoustic case, the medium is described with the material properties mass density  $\rho(\mathbf{x})$  and compressibility  $\kappa(\mathbf{x})$ ; in the elastic case, the material properties are mass density  $\rho(\mathbf{x})$  and compliance  $s_{pqkl}(\mathbf{x})$ ; in the electromagnetic case the medium is described by electric permittivity  $\varepsilon_{kr}(\mathbf{x})$  and magnetic permeability  $\mu_{ji}(\mathbf{x})$ . It is assumed that the time dependence of the electric permittivity and the magnetic permeability can be incorporated in the electric and magnetic conductivities, respectively.

However, because the medium is taken lossless, the electric and magnetic conductivities are set to zero. Domain  $\mathbb{D}$  is enclosed by a boundary  $\partial\mathbb{D}$  with an outward-pointing normal vector  $\mathbf{n}$ . For the medium, inside as well as outside  $\mathbb{D}$ , in the frequency domain the system of two equations defining the wave propagation can be written in matrix-vector form as

$$j\omega\mathbf{A}(\mathbf{x})\hat{\mathbf{u}}(\mathbf{x},\omega) + \mathbf{D}\hat{\mathbf{u}}(\mathbf{x},\omega) = \hat{\mathbf{s}}(\mathbf{x},\omega). \quad (2.1)$$

In the above equation, the variable  $\hat{\mathbf{u}}(\mathbf{x},\omega)$  represents the wave fields,  $\hat{\mathbf{s}}(\mathbf{x},\omega)$  - the source vector,  $\mathbf{A}(\mathbf{x})$  - the frequency-independent material properties, and  $\mathbf{D}$  is an operator matrix representing differentiation with respect to the three spatial dimensions. Table 2.1 shows the expansion of these variables in the acoustic, elastic, and electromagnetic case.

To obtain reciprocity relations, two independent states  $\mathcal{A}$  and  $\mathcal{B}$  are considered in domain  $\mathbb{D}$ . State  $\mathcal{A}$  is described by the wave quantity  $\hat{\mathbf{u}}_{\mathcal{A}}(\mathbf{x},\omega)$ , by the source quantity  $\hat{\mathbf{s}}_{\mathcal{A}}(\mathbf{x},\omega)$  and by the material matrix  $\mathbf{A}(\mathbf{x})$ . State  $\mathcal{B}$  is characterized by the same quantities, but the corresponding subscripts  $\mathcal{A}$  are replaced by subscripts  $\mathcal{B}$ . Further, to arrive at a reciprocity relation between the wavefields in the two states, wavefield interactions are considered in domain  $\mathbb{D}$ .

One wavefield interaction can be described by a local convolution between the wavefields in the two states [de Hoop, 1995] and can be written as

$$\hat{\mathbf{u}}_{\mathcal{A}}^T(\mathbf{x},\omega)\mathbf{K}\left(\underline{\mathbf{D}} + \mathbf{D}\right)\hat{\mathbf{u}}_{\mathcal{B}}(\mathbf{x},\omega) = -\left(\mathbf{D}\hat{\mathbf{u}}_{\mathcal{A}}(\mathbf{x},\omega)\right)^T\mathbf{K}\hat{\mathbf{u}}_{\mathcal{B}}(\mathbf{x},\omega) + \hat{\mathbf{u}}_{\mathcal{A}}^T(\mathbf{x},\omega)\mathbf{K}\left(\mathbf{D}\hat{\mathbf{u}}_{\mathcal{B}}(\mathbf{x},\omega)\right). \quad (2.2)$$

In the above equation, the superscript  $T$  denotes matrix transposition,  $\underline{\mathbf{D}}$  means that the differentiation operator  $\mathbf{D}$  acts on the wave quantity left of it, and  $\mathbf{K} = \text{diag}(-1, 1)$ . Further, to obtain the right-hand side of the equation, the properties  $\mathbf{K}^T = \mathbf{K}$ ,  $\mathbf{K}\mathbf{D} = -\mathbf{D}\mathbf{K}$ , and  $\mathbf{D}^T = \mathbf{D}$  were used. The latter property, in the acoustic case, is easily verified by inspecting Table 2.1. To verify this property in the elastic case, the relation  $\Delta_{ijkl} = \Delta_{klji}$  should be used. In the electromagnetic case, the property  $\mathbf{D}^T = \mathbf{D}$  is verified by using the fact that  $-\epsilon_{kmi} = \epsilon_{imk}$ . A similar remark holds for  $\epsilon_{jmr}$ .

Substitution of the matrix-vector equation 2.1 into the right-hand side of

Parameter	Acoustic case	Elastic case	Electromagnetic case
$\hat{\mathbf{u}}(\mathbf{x}, \omega)$	$\begin{pmatrix} \hat{p}(\mathbf{x}, \omega) \\ \hat{v}_i(\mathbf{x}, \omega) \end{pmatrix}$	$\begin{pmatrix} \hat{v}_i(\mathbf{x}, \omega) \\ -\hat{\tau}_{kl}(\mathbf{x}, \omega) \end{pmatrix}$	$\begin{pmatrix} \hat{E}_r(\mathbf{x}, \omega) \\ \hat{H}_i(\mathbf{x}, \omega) \end{pmatrix}$
$\hat{\mathbf{s}}(\mathbf{x}, \omega)$	$\begin{pmatrix} \hat{q}(\mathbf{x}, \omega) \\ \hat{f}_i(\mathbf{x}, \omega) \end{pmatrix}$	$\begin{pmatrix} \hat{f}_i(\mathbf{x}, \omega) \\ \hat{h}_{pq}(\mathbf{x}, \omega) \end{pmatrix}$	$\begin{pmatrix} -\hat{J}_k^e(\mathbf{x}, \omega) \\ -\hat{J}_j^m(\mathbf{x}, \omega) \end{pmatrix}$
$\mathbf{A}(\mathbf{x})$	$\begin{pmatrix} \kappa(\mathbf{x}) & 0 \\ 0 & \rho(\mathbf{x}) \end{pmatrix}$	$\begin{pmatrix} \rho(\mathbf{x}) & 0 \\ 0 & s_{pqkl}(\mathbf{x}) \end{pmatrix}$	$\begin{pmatrix} \epsilon_{kr}(\mathbf{x}) & 0 \\ 0 & \mu_{ji}(\mathbf{x}) \end{pmatrix}$
$\mathbf{D}$	$\begin{pmatrix} 0 & \partial_i \\ \partial_i & 0 \end{pmatrix}$	$\begin{pmatrix} 0 & \Delta_{ijkl}\partial_j \\ \Delta_{pqji}\partial_j & 0 \end{pmatrix}$	$\begin{pmatrix} 0 & -\epsilon_{kmi}\partial_m \\ \epsilon_{jmr}\partial_m & 0 \end{pmatrix}$

**Table 2.1:** Expansion of the variables in equation 2.1 in the acoustic, elastic, or electromagnetic case. In the first row,  $\hat{p}$  stands for acoustic pressure,  $\hat{v}_i$  denotes the particle velocity vector,  $\hat{\tau}_{kl}$  stands for the stress tensor,  $\hat{E}_r$  describes the electric field vector, and  $\hat{H}_i$  describes the magnetic field vector. In the second row,  $\hat{q}$  represents the source distribution in terms of volume injection-rate density,  $\hat{f}_i$  represents the source distribution in terms of external volume force density,  $\hat{h}_{pq}$  stands for the external deformation-rate density, and  $\hat{J}_k^e$  and  $\hat{J}_j^m$  stand for the external source volume densities of electric and magnetic currents, respectively. In the third row,  $\kappa$  denotes the compressibility,  $\rho$  denotes the volume density of mass,  $s_{pqkl}$  describes the compliance,  $\epsilon_{kr}$  describes the electric permittivity, and  $\mu_{ji}$  denotes the magnetic permeability. In the fourth row,  $\Delta_{ijkl} = \frac{1}{2}(\delta_{ik}\delta_{jl} + \delta_{jk}\delta_{il})$ , where  $\delta_{ab}$  is the Kronecker delta function, while  $\epsilon_{kmi}$  is the antisymmetric (Levi-Civita) tensor of rank three, where  $\epsilon_{kmi} = 1$ , for  $kmi = \{123, 231, 312\}$ , and  $\epsilon_{kmi} = -1$ , for  $kmi = \{132, 213, 321\}$ .



equation 2.2 and using the property  $\mathbf{A}_{\mathcal{A}}^T(\mathbf{x}) \mathbf{K} = \mathbf{K} \mathbf{A}_{\mathcal{A}}(\mathbf{x})$ , results in

$$\begin{aligned} \hat{\mathbf{u}}_{\mathcal{A}}^T(\mathbf{x}, \omega) \mathbf{K} \mathbf{D} \hat{\mathbf{u}}_{\mathcal{B}}(\mathbf{x}, \omega) + \hat{\mathbf{u}}_{\mathcal{A}}^T(\mathbf{x}, \omega) \mathbf{K} \mathbf{D} \hat{\mathbf{u}}_{\mathcal{B}}(\mathbf{x}, \omega) = \\ \hat{\mathbf{u}}_{\mathcal{A}}^T(\mathbf{x}, \omega) \mathbf{K} \hat{\mathbf{S}}_{\mathcal{B}}(\mathbf{x}, \omega) - \hat{\mathbf{S}}_{\mathcal{A}}^T(\mathbf{x}, \omega) \mathbf{K} \hat{\mathbf{u}}_{\mathcal{B}}(\mathbf{x}, \omega) \\ + j\omega \hat{\mathbf{u}}_{\mathcal{A}}^T(\mathbf{x}, \omega) \mathbf{K} \left( \mathbf{A}_{\mathcal{A}}(\mathbf{x}) - \mathbf{A}_{\mathcal{B}}(\mathbf{x}) \right) \hat{\mathbf{u}}_{\mathcal{B}}(\mathbf{x}, \omega). \end{aligned} \quad (2.3)$$

Equation 2.3 represents the local form of the two-way wavefield convolution-type reciprocity theorem [Rayleigh, 1878; de Hoop, 1988; Fokkema and van den Berg, 1993] because multiplication of two quantities in the frequency domain corresponds to a convolution in the time domain.

Integration of equation 2.3 over the domain  $\mathbb{D}$  and application of Gauss' divergence theorem to the left-hand side of equation 2.3 yields (after swapping the places of the two sides)

$$\begin{aligned} \int_{\mathbb{D}} \left\{ \hat{\mathbf{u}}_{\mathcal{A}}^T(\mathbf{x}, \omega) \mathbf{K} \hat{\mathbf{S}}_{\mathcal{B}}(\mathbf{x}, \omega) - \hat{\mathbf{S}}_{\mathcal{A}}^T(\mathbf{x}, \omega) \mathbf{K} \hat{\mathbf{u}}_{\mathcal{B}}(\mathbf{x}, \omega) \right. \\ \left. + j\omega \hat{\mathbf{u}}_{\mathcal{A}}^T(\mathbf{x}, \omega) \mathbf{K} \left( \mathbf{A}_{\mathcal{A}}(\mathbf{x}) - \mathbf{A}_{\mathcal{B}}(\mathbf{x}) \right) \hat{\mathbf{u}}_{\mathcal{B}}(\mathbf{x}, \omega) \right\} d^3\mathbf{x} = \\ \oint_{\partial\mathbb{D}} \hat{\mathbf{u}}_{\mathcal{A}}^T(\mathbf{x}, \omega) \mathbf{K} \mathbf{N}_{\mathbf{x}} \hat{\mathbf{u}}_{\mathcal{B}}(\mathbf{x}, \omega) d^2\mathbf{x}, \end{aligned} \quad (2.4)$$

where in the acoustic case  $\mathbf{N}_{\mathbf{x}} = \text{antidiag}(n_i, n_i)$ , in the elastic case it is  $\mathbf{N}_{\mathbf{x}} = \text{antidiag}(\Delta_{ijkl}n_j, \Delta_{pqji}n_j)$ , and in the electromagnetic case it is  $\mathbf{N}_{\mathbf{x}} = \text{antidiag}(-\epsilon_{kmi}n_m, \epsilon_{jmr}n_m)$ . Equation 2.4 is known as the global form of the two-way wavefield convolution-type reciprocity theorem.

When the material quantities are assumed to be the same for both states, i.e.,  $\mathbf{A}_{\mathcal{A}}(\mathbf{x}) = \mathbf{A}_{\mathcal{B}}(\mathbf{x})$ , equation 2.4 can be rewritten as

$$\begin{aligned} \int_{\mathbb{D}} \left\{ \hat{\mathbf{u}}_{\mathcal{A}}^T(\mathbf{x}, \omega) \mathbf{K} \hat{\mathbf{S}}_{\mathcal{B}}(\mathbf{x}, \omega) - \hat{\mathbf{S}}_{\mathcal{A}}^T(\mathbf{x}, \omega) \mathbf{K} \hat{\mathbf{u}}_{\mathcal{B}}(\mathbf{x}, \omega) \right\} d^3\mathbf{x} = \\ \oint_{\partial\mathbb{D}} \hat{\mathbf{u}}_{\mathcal{A}}^T(\mathbf{x}, \omega) \mathbf{K} \mathbf{N}_{\mathbf{x}} \hat{\mathbf{u}}_{\mathcal{B}}(\mathbf{x}, \omega) d^2\mathbf{x}. \end{aligned} \quad (2.5)$$

Another wavefield interaction can be described by a local correlation between the wavefields in the two states [de Hoop, 1995] and can be written

as

$$\hat{\mathbf{u}}_{\mathcal{A}}^{\dagger}(\mathbf{x}, \omega) \left( \underline{\mathbf{D}} + \mathbf{D} \right) \hat{\mathbf{u}}_{\mathcal{B}}(\mathbf{x}, \omega) = \left( \mathbf{D} \hat{\mathbf{u}}_{\mathcal{A}}(\mathbf{x}, \omega) \right)^{\dagger} \hat{\mathbf{u}}_{\mathcal{B}}(\mathbf{x}, \omega) + \hat{\mathbf{u}}_{\mathcal{A}}^{\dagger}(\mathbf{x}, \omega) \left( \mathbf{D} \hat{\mathbf{u}}_{\mathcal{B}}(\mathbf{x}, \omega) \right), \quad (2.6)$$

where the superscript  $\dagger$  means complex conjugation and transposition, hence  $\hat{\mathbf{u}}_{\mathcal{A}}^{\dagger}(\mathbf{x}, \omega)$  is the time-reversed variant of  $\hat{\mathbf{u}}_{\mathcal{A}}^T(\mathbf{x}, \omega)$ . Then, after substitution of equation 2.1 into the right-hand side of equation 2.6 and making use of the property  $\mathbf{A}_{\mathcal{A}}^{\dagger}(\mathbf{x}) = \mathbf{A}_{\mathcal{A}}(\mathbf{x})$ , which follows from the invariance to time-reversal of the wave equation, one arrives at

$$\begin{aligned} \hat{\mathbf{u}}_{\mathcal{A}}^{\dagger}(\mathbf{x}, \omega) \underline{\mathbf{D}} \hat{\mathbf{u}}_{\mathcal{B}}(\mathbf{x}, \omega) + \hat{\mathbf{u}}_{\mathcal{A}}^{\dagger}(\mathbf{x}, \omega) \mathbf{D} \hat{\mathbf{u}}_{\mathcal{B}}(\mathbf{x}, \omega) = \\ \hat{\mathbf{u}}_{\mathcal{A}}^{\dagger}(\mathbf{x}, \omega) \hat{\mathbf{s}}_{\mathcal{B}}(\mathbf{x}, \omega) + \hat{\mathbf{s}}_{\mathcal{A}}^{\dagger}(\mathbf{x}, \omega) \hat{\mathbf{u}}_{\mathcal{B}}(\mathbf{x}, \omega) \\ + j\omega \hat{\mathbf{u}}_{\mathcal{A}}^{\dagger}(\mathbf{x}, \omega) \left( \mathbf{A}_{\mathcal{A}}(\mathbf{x}) - \mathbf{A}_{\mathcal{B}}(\mathbf{x}) \right) \hat{\mathbf{u}}_{\mathcal{B}}(\mathbf{x}, \omega). \end{aligned} \quad (2.7)$$

Equation 2.7 represents the local form of the two-way wavefield correlation-type reciprocity theorem [Bojarski, 1983; de Hoop, 1988; Wapenaar and Berkhout, 1989; Fokkema and van den Berg, 1993] since a multiplication of a quantity with a complex-conjugate of another quantity in the frequency domain corresponds to a correlation in the time domain.

Integration of equation 2.7 over the domain  $\mathbb{D}$  and application of Gauss' divergence theorem to the left-hand side of equation 2.7 gives

$$\begin{aligned} \int_{\mathbb{D}} \left\{ \hat{\mathbf{u}}_{\mathcal{A}}^{\dagger}(\mathbf{x}, \omega) \hat{\mathbf{s}}_{\mathcal{B}}(\mathbf{x}, \omega) + \hat{\mathbf{s}}_{\mathcal{A}}^{\dagger}(\mathbf{x}, \omega) \hat{\mathbf{u}}_{\mathcal{B}}(\mathbf{x}, \omega) \right. \\ \left. + j\omega \hat{\mathbf{u}}_{\mathcal{A}}^{\dagger}(\mathbf{x}, \omega) \left( \mathbf{A}_{\mathcal{A}}(\mathbf{x}) - \mathbf{A}_{\mathcal{B}}(\mathbf{x}) \right) \hat{\mathbf{u}}_{\mathcal{B}}(\mathbf{x}, \omega) \right\} d^3\mathbf{x} = \\ \oint_{\partial\mathbb{D}} \hat{\mathbf{u}}_{\mathcal{A}}^{\dagger}(\mathbf{x}, \omega) \mathbf{N}_{\mathbf{x}} \hat{\mathbf{u}}_{\mathcal{B}}(\mathbf{x}, \omega) d^2\mathbf{x}. \end{aligned} \quad (2.8)$$

Equation 2.8 is known as the global form of the two-way wavefield correlation-type reciprocity theorem.

For the case when the material properties in both states are the same, equation 2.8 can be rewritten as

$$\int_{\mathbb{D}} \left\{ \hat{\mathbf{u}}_{\mathcal{A}}^{\dagger}(\mathbf{x}, \omega) \hat{\mathbf{s}}_{\mathcal{B}}(\mathbf{x}, \omega) + \hat{\mathbf{s}}_{\mathcal{A}}^{\dagger}(\mathbf{x}, \omega) \hat{\mathbf{u}}_{\mathcal{B}}(\mathbf{x}, \omega) \right\} d^3\mathbf{x} = \oint_{\partial\mathbb{D}} \hat{\mathbf{u}}_{\mathcal{A}}^{\dagger}(\mathbf{x}, \omega) \mathbf{N}_{\mathbf{x}} \hat{\mathbf{u}}_{\mathcal{B}}(\mathbf{x}, \omega) d^2\mathbf{x}. \quad (2.9)$$

The the global forms of the reciprocity theorems 2.4 and 2.8 (or 2.5 and 2.9, respectively) can be used to obtain the wavefields inside domain  $\mathbb{D}$  only from measurements of the wavefields along its boundary  $\partial\mathbb{D}$ . In this sense, these theorems are used, for example, to derive integral equations for forward and inverse two-way wavefield extrapolation [Wapenaar and Berkhout, 1989]. In the following subsections, the reciprocity theorems 2.5 and 2.9 are used to derive source-receiver reciprocity relations followed by relations for seismic and electromagnetic interferometry.

### ■ 2.1.2 SI relations for impulsive sources in an acoustic medium

For an acoustic medium, as specified in the acoustic-case column of Table 2.1, the reciprocity relations 2.5 and 2.9 can be rewritten as

$$\int_{\mathbb{D}} \left\{ \hat{p}_{\mathcal{A}}(\mathbf{x}, \omega) \hat{q}_{\mathcal{B}}(\mathbf{x}, \omega) - \hat{v}_{i,\mathcal{A}}(\mathbf{x}, \omega) \hat{f}_{i,\mathcal{B}}(\mathbf{x}, \omega) - \hat{q}_{\mathcal{A}}(\mathbf{x}, \omega) \hat{p}_{\mathcal{B}}(\mathbf{x}, \omega) + \hat{f}_{i,\mathcal{A}}(\mathbf{x}, \omega) \hat{v}_{i,\mathcal{B}}(\mathbf{x}, \omega) \right\} d^3\mathbf{x} = \oint_{\partial\mathbb{D}} \left\{ \hat{p}_{\mathcal{A}}(\mathbf{x}, \omega) \hat{v}_{i,\mathcal{B}}(\mathbf{x}, \omega) - \hat{v}_{i,\mathcal{A}}(\mathbf{x}, \omega) \hat{p}_{\mathcal{B}}(\mathbf{x}, \omega) \right\} n_i d^2\mathbf{x} \quad (2.10)$$

and

$$\int_{\mathbb{D}} \left\{ \hat{p}_{\mathcal{A}}^*(\mathbf{x}, \omega) \hat{q}_{\mathcal{B}}(\mathbf{x}, \omega) + \hat{v}_{i,\mathcal{A}}^*(\mathbf{x}, \omega) \hat{f}_{i,\mathcal{B}}(\mathbf{x}, \omega) + \hat{q}_{\mathcal{A}}^*(\mathbf{x}, \omega) \hat{p}_{\mathcal{B}}(\mathbf{x}, \omega) + \hat{f}_{i,\mathcal{A}}^*(\mathbf{x}, \omega) \hat{v}_{i,\mathcal{B}}(\mathbf{x}, \omega) \right\} d^3\mathbf{x} = \oint_{\partial\mathbb{D}} \left\{ \hat{p}_{\mathcal{A}}^*(\mathbf{x}, \omega) \hat{v}_{i,\mathcal{B}}(\mathbf{x}, \omega) + \hat{v}_{i,\mathcal{A}}^*(\mathbf{x}, \omega) \hat{p}_{\mathcal{B}}(\mathbf{x}, \omega) \right\} n_i d^2\mathbf{x}, \quad (2.11)$$

respectively.

To make use of the reciprocity theorems, certain choices should be made for the wavefields and the source fields in the states  $\mathcal{A}$  and  $\mathcal{B}$ . Taking only impulsive sources of volume injection-rate density  $\hat{q}(\mathbf{x}, \omega)$  at points  $\mathbf{x}_\mathcal{A}$  and  $\mathbf{x}_\mathcal{B}$  in  $\mathbb{D}$  for states  $\mathcal{A}$  and  $\mathcal{B}$ , respectively, one can define the recorded pressure  $\hat{p}(\mathbf{x}, \omega)$  at  $\mathbf{x}$  in both states as the observed impulse response (Green's function  $\hat{G}(\mathbf{x}, \mathbf{x}_{\mathcal{A}(\mathcal{B})}, \omega)$ ) (see Table 2.2). The expressions for the particle velocities observed at  $\mathbf{x}$  for states  $\mathcal{A}$  and  $\mathcal{B}$  are obtained from the substitution of the respective quantities for  $\hat{q}(\mathbf{x}, \omega)$ ,  $\hat{f}_i(\mathbf{x}, \omega)$ , and  $\hat{p}(\mathbf{x}, \omega)$  from Table 2.2 into the wave equation 2.1 in case of an acoustic medium.

Parameter	State $\mathcal{A}$	State $\mathcal{B}$
$\hat{q}(\mathbf{x}, \omega)$	$\delta(\mathbf{x} - \mathbf{x}_\mathcal{A})$	$\delta(\mathbf{x} - \mathbf{x}_\mathcal{B})$
$\hat{f}_i(\mathbf{x}, \omega)$	0	0
$\hat{p}(\mathbf{x}, \omega)$	$\hat{G}(\mathbf{x}, \mathbf{x}_\mathcal{A}, \omega)$	$\hat{G}(\mathbf{x}, \mathbf{x}_\mathcal{B}, \omega)$
$\hat{v}_i(\mathbf{x}, \omega)$	$\frac{-1}{j\omega\rho(\mathbf{x})}\partial_i\hat{G}(\mathbf{x}, \mathbf{x}_\mathcal{A}, \omega)$	$\frac{-1}{j\omega\rho(\mathbf{x})}\partial_i\hat{G}(\mathbf{x}, \mathbf{x}_\mathcal{B}, \omega)$

**Table 2.2:** Choices for wavefield and source parameters for the acoustical states  $\mathcal{A}$  and  $\mathcal{B}$  to be used in the two-way wavefield acoustic reciprocity theorems.

Substitution of the expressions in the middle and right columns of Table 2.2 for their corresponding quantities in the convolution-type reciprocity theorem 2.10 and the use of the sifting property of the delta function, results in

$$\begin{aligned} \hat{G}(\mathbf{x}_\mathcal{B}, \mathbf{x}_\mathcal{A}, \omega) - \hat{G}(\mathbf{x}_\mathcal{A}, \mathbf{x}_\mathcal{B}, \omega) = \\ \oint_{\partial\mathbb{D}} \frac{-1}{j\omega\rho(\mathbf{x})} \left\{ \hat{G}(\mathbf{x}, \mathbf{x}_\mathcal{A}, \omega) \partial_i \hat{G}(\mathbf{x}, \mathbf{x}_\mathcal{B}, \omega) \right. \\ \left. - \left( \partial_i \hat{G}(\mathbf{x}, \mathbf{x}_\mathcal{A}, \omega) \right) \hat{G}(\mathbf{x}, \mathbf{x}_\mathcal{B}, \omega) \right\} n_i d^2\mathbf{x}. \quad (2.12) \end{aligned}$$

The right-hand side of equation 2.12 represents a surface integral over products of causal-in-time Green's functions. If the surface of integration  $\partial\mathbb{D}$  is chosen to be a sphere with infinite radius  $\Delta \rightarrow \infty$ , the right-hand side of

equation 2.12 will go to zero as it will be of order  $O(\Delta^{-1})$  [Fokkema and van den Berg, 1993]. If for this  $\partial\mathbb{D}$  the right-hand side vanishes, then, because it is independent of the choice of the boundary, it should vanish for any choice of  $\partial\mathbb{D}$  as long as the points  $\mathbf{x}_A$  and  $\mathbf{x}_B$  are inside it. This results in the acoustic source-receiver reciprocity relation

$$\hat{G}(\mathbf{x}_B, \mathbf{x}_A, \omega) = \hat{G}(\mathbf{x}_A, \mathbf{x}_B, \omega) . \quad (2.13)$$

This relation shows the well-known property that interchanging the place of source and receiver will not change the measurement result.

Let one now substitute the quantities from the middle and the right columns of Table 2.2 into their corresponding places in the correlation-type acoustic reciprocity theorem 2.11. Making again use of the sifting property of the delta function gives

$$\begin{aligned} \hat{G}^*(\mathbf{x}_B, \mathbf{x}_A, \omega) + \hat{G}(\mathbf{x}_A, \mathbf{x}_B, \omega) = \\ \oint_{\partial\mathbb{D}} \frac{-1}{j\omega\rho(\mathbf{x})} \left\{ \hat{G}^*(\mathbf{x}, \mathbf{x}_A, \omega) \partial_i \hat{G}(\mathbf{x}, \mathbf{x}_B, \omega) \right. \\ \left. - \left( \partial_i \hat{G}(\mathbf{x}, \mathbf{x}_A, \omega) \right)^* \hat{G}(\mathbf{x}, \mathbf{x}_B, \omega) \right\} n_i d^2\mathbf{x} . \end{aligned} \quad (2.14)$$

Further application of the source-receiver reciprocity 2.13 to both sides of equation 2.14 results in

$$\begin{aligned} 2\Re \left\{ \hat{G}(\mathbf{x}_A, \mathbf{x}_B, \omega) \right\} = \\ \oint_{\partial\mathbb{D}} \frac{-1}{j\omega\rho(\mathbf{x})} \left\{ \hat{G}^*(\mathbf{x}_A, \mathbf{x}, \omega) \partial_i \hat{G}(\mathbf{x}_B, \mathbf{x}, \omega) \right. \\ \left. - \left( \partial_i \hat{G}(\mathbf{x}_A, \mathbf{x}, \omega) \right)^* \hat{G}(\mathbf{x}_B, \mathbf{x}, \omega) \right\} n_i d^2\mathbf{x} , \end{aligned} \quad (2.15)$$

where  $\Re$  stands for "real part". The products in the right-hand side correspond to crosscorrelations in the time domain, while the left-hand side corresponds in the time domain to a Green's function and its time-reversed version. In this way, relation 2.15 gives the possibility to retrieve the complete Green's function and its time-reversed version between the points  $\mathbf{x}_A$  and  $\mathbf{x}_B$  from the constructive and destructive interference (the summation) of crosscorrelations of observed Green's functions  $\hat{G}(\mathbf{x}_{A(B)}, \mathbf{x}, \omega)$  due to monopole

sources on  $\partial\mathbb{D}$  and observed Green's functions  $\partial_i \hat{G}(\mathbf{x}_{\mathcal{A}(\mathcal{B})}, \mathbf{x}, \omega) n_i$  due to dipole sources on  $\partial\mathbb{D}$ .

Equation 2.15 is exact and valid for any lossless inhomogeneous (inside, as well as outside  $\partial\mathbb{D}$ ) acoustic medium. It represents the basis for acoustic SI. Van Manen et al. [2005] developed an effective modelling scheme based on a relation very similar to equation 2.15, where the difference comes from using another source definition for the Green's function.

Even though equation 2.15 is very useful for modelling or laboratory investigations, there are several difficulties in its application to field data, like for example in petroleum exploration. One difficulty is the need to evaluate two correlation products. To overcome this, let one assume that in a small region (relative to the dominant wavelength) around  $\partial\mathbb{D}$  the medium parameters change smoothly. The Green's functions observed in domain  $\mathbb{D}$  can be written as a sum of waves that propagate initially inward from the sources on  $\partial\mathbb{D}$  (superscript *in*) and of waves that propagate initially outward from the sources (superscript *out*):

$$\hat{G}(\mathbf{x}_{\mathcal{A}(\mathcal{B})}, \mathbf{x}, \omega) = \hat{G}^{in}(\mathbf{x}_{\mathcal{A}(\mathcal{B})}, \mathbf{x}, \omega) + \hat{G}^{out}(\mathbf{x}_{\mathcal{A}(\mathcal{B})}, \mathbf{x}, \omega). \quad (2.16)$$

Substitution of equation 2.16 for states  $\mathcal{A}$  and  $\mathcal{B}$  into the SI relation 2.15 gives

$$\begin{aligned} 2\Re \left\{ \hat{G}(\mathbf{x}_{\mathcal{A}}, \mathbf{x}_{\mathcal{B}}, \omega) \right\} = & \oint_{\partial\mathbb{D}} \frac{-1}{j\omega\rho(\mathbf{x})} \left\{ \left[ \hat{G}^{in*}(\mathbf{x}_{\mathcal{A}}, \mathbf{x}, \omega) + \hat{G}^{out*}(\mathbf{x}_{\mathcal{A}}, \mathbf{x}, \omega) \right] \times \right. \\ & \left[ \partial_i \hat{G}^{in}(\mathbf{x}_{\mathcal{B}}, \mathbf{x}, \omega) + \partial_i \hat{G}^{out}(\mathbf{x}_{\mathcal{B}}, \mathbf{x}, \omega) \right] \\ & - \left[ \left( \partial_i \hat{G}^{in}(\mathbf{x}_{\mathcal{A}}, \mathbf{x}, \omega) \right)^* + \left( \partial_i \hat{G}^{out}(\mathbf{x}_{\mathcal{A}}, \mathbf{x}, \omega) \right)^* \right] \times \\ & \left. \left[ \hat{G}^{in}(\mathbf{x}_{\mathcal{B}}, \mathbf{x}, \omega) + \hat{G}^{out}(\mathbf{x}_{\mathcal{B}}, \mathbf{x}, \omega) \right] \right\} n_i d^2\mathbf{x} \quad (2.17) \end{aligned}$$

or

$$\begin{aligned}
2\Re \left\{ \hat{G}(\mathbf{x}_A, \mathbf{x}_B, \omega) \right\} &= \oint_{\partial\mathbb{D}} \frac{-1}{j\omega\rho(\mathbf{x})} \left\{ \hat{G}^{in*}(\mathbf{x}_A, \mathbf{x}, \omega) \partial_i \hat{G}^{in}(\mathbf{x}_B, \mathbf{x}, \omega) \right. \\
&- \left( \partial_i \hat{G}^{in}(\mathbf{x}_A, \mathbf{x}, \omega) \right)^* \hat{G}^{in}(\mathbf{x}_B, \mathbf{x}, \omega) + \hat{G}^{out*}(\mathbf{x}_A, \mathbf{x}, \omega) \partial_i \hat{G}^{out}(\mathbf{x}_B, \mathbf{x}, \omega) \\
&\quad \left. - \left( \partial_i \hat{G}^{out}(\mathbf{x}_A, \mathbf{x}, \omega) \right)^* \hat{G}^{out}(\mathbf{x}_B, \mathbf{x}, \omega) \right\} n_i d\mathbf{x}^2 \\
&+ \oint_{\partial\mathbb{D}} \frac{-1}{j\omega\rho(\mathbf{x})} \left\{ \hat{G}^{in*}(\mathbf{x}_A, \mathbf{x}, \omega) \partial_i \hat{G}^{out}(\mathbf{x}_B, \mathbf{x}, \omega) \right. \\
&- \left( \partial_i \hat{G}^{in}(\mathbf{x}_A, \mathbf{x}, \omega) \right)^* \hat{G}^{out}(\mathbf{x}_B, \mathbf{x}, \omega) + \hat{G}^{out*}(\mathbf{x}_A, \mathbf{x}, \omega) \partial_i \hat{G}^{in}(\mathbf{x}_B, \mathbf{x}, \omega) \\
&\quad \left. - \left( \partial_i \hat{G}^{out}(\mathbf{x}_A, \mathbf{x}, \omega) \right)^* \hat{G}^{in}(\mathbf{x}_B, \mathbf{x}, \omega) \right\} n_i d^2\mathbf{x}. \quad (2.18)
\end{aligned}$$

When the dominant wavelengths of the fields are small compared to the sizes of the inhomogeneities (high-frequency regime), then for each constituent  $\hat{G}_w^{in}(\mathbf{x}_{A(B)}, \mathbf{x}, \omega)$  and  $\hat{G}_w^{out}(\mathbf{x}_{A(B)}, \mathbf{x}, \omega)$  - direct wave, scattered wave, etc. - of the Green's function, one has

$$\partial_i \hat{G}_w^{in}(\mathbf{x}_{A(B)}, \mathbf{x}, \omega) n_i = -j \frac{\omega}{c(\mathbf{x})} |\cos \alpha_w(\mathbf{x})| \hat{G}_w^{in}(\mathbf{x}_{A(B)}, \mathbf{x}, \omega) \quad (2.19a)$$

$$\partial_i \hat{G}_w^{out}(\mathbf{x}_{A(B)}, \mathbf{x}, \omega) n_i = +j \frac{\omega}{c(\mathbf{x})} |\cos \alpha_w(\mathbf{x})| \hat{G}_w^{out}(\mathbf{x}_{A(B)}, \mathbf{x}, \omega), \quad (2.19b)$$

where  $c(\mathbf{x})$  is the local propagation velocity and  $\alpha_w(\mathbf{x})$  is the local angle between the pertinent ray and the normal on  $\partial\mathbb{D}$ . Note that in the above equation, no summation takes place over  $w$ . The main contribution to the integrals in equation 2.18 comes from regions on  $\partial\mathbb{D}$  around the stationary points [Schuster et al., 2004; Snieder, 2004; Wapenaar et al., 2004a]. For such regions,  $|\cos \alpha_w(\mathbf{x})|$  for  $\hat{G}_w(\mathbf{x}_A, \mathbf{x}, \omega)$  and  $\hat{G}_w(\mathbf{x}_B, \mathbf{x}, \omega)$  will be identical. This means that in equation 2.18 the second integral will disappear, while the terms under the first integral will add together. Hence,

$$\begin{aligned}
2\Re \left\{ \hat{G}(\mathbf{x}_A, \mathbf{x}_B, \omega) \right\} &= \\
&\oint_{\partial\mathbb{D}} \frac{2}{j\omega\rho(\mathbf{x})} \left\{ \left( \partial_i \hat{G}^{in}(\mathbf{x}_A, \mathbf{x}, \omega) \right)^* \hat{G}^{in}(\mathbf{x}_B, \mathbf{x}, \omega) \right. \\
&\quad \left. + \left( \partial_i \hat{G}^{out}(\mathbf{x}_A, \mathbf{x}, \omega) \right)^* \hat{G}^{out}(\mathbf{x}_B, \mathbf{x}, \omega) \right\} n_i d^2\mathbf{x}. \quad (2.20)
\end{aligned}$$

Because the inward- and outward-propagating waves at the points  $\mathbf{x}$  on  $\partial\mathbb{D}$  cannot be measured separately, equation 2.16 for states  $\mathcal{A}$  and  $\mathcal{B}$  is used to rewrite equation 2.20 as

$$2\Re \left\{ \hat{G}(\mathbf{x}_A, \mathbf{x}_B, \omega) \right\} + \text{ghosts} = \oint_{\partial\mathbb{D}} \frac{2}{j\omega\rho(\mathbf{x})} \left( \partial_i \hat{G}(\mathbf{x}_A, \mathbf{x}, \omega) \right)^* \hat{G}(\mathbf{x}_B, \mathbf{x}, \omega) n_i d^2\mathbf{x}, \quad (2.21)$$

where

$$\text{ghosts} = \oint_{\partial\mathbb{D}} \frac{2}{j\omega\rho(\mathbf{x})} \left\{ \left( \partial_i \hat{G}^{in}(\mathbf{x}_A, \mathbf{x}, \omega) \right)^* \hat{G}^{out}(\mathbf{x}_B, \mathbf{x}, \omega) + \left( \partial_i \hat{G}^{out}(\mathbf{x}_A, \mathbf{x}, \omega) \right)^* \hat{G}^{in}(\mathbf{x}_B, \mathbf{x}, \omega) \right\} n_i d^2\mathbf{x}. \quad (2.22)$$

The left-hand side of equation 2.21 contains not only the retrieved Green's function, but also spurious events (ghosts) that will appear as a result from the crosscorrelations in the right-hand side (see Figure 3.12). These ghosts result from the integration over correlation products of inward-propagating waves in one of the states with outward-propagating waves in the other state. When the sources are randomly distributed in space, i.e., the surface  $\partial\mathbb{D}$  is sufficiently irregular, the correlation products will not interfere coherently and the ghost terms will be strongly weakened and can be ignored, while the retrieved Green's function will correctly contain all scattered fields from inside and outside  $\partial\mathbb{D}$  (see Figure 3.15 and Draganov et al. [2003]).

If, on the other hand, the medium at and outside  $\partial\mathbb{D}$  is assumed to be homogeneous with propagation velocity  $c$  and mass density  $\rho$ , then  $\text{ghosts} = 0$ . Furthermore, if  $\partial\mathbb{D}$  is taken to be a sphere with a sufficiently large radius, then all rays are normal to  $\partial\mathbb{D}$  and consequently  $\alpha = 0$ . Then, from equation 2.21 one finally obtains

$$2\Re \left\{ \hat{G}(\mathbf{x}_A, \mathbf{x}_B, \omega) \right\} \approx \frac{2}{\rho c} \oint_{\partial\mathbb{D}} \hat{G}^*(\mathbf{x}_A, \mathbf{x}, \omega) \hat{G}(\mathbf{x}_B, \mathbf{x}, \omega) d^2\mathbf{x}. \quad (2.23)$$

The approximation in equation 2.23 involves only amplitude errors; when  $\partial\mathbb{D}$  differs significantly from a sphere, these errors may be significant. Furthermore, due to incomplete destructive interference, events that would be



canceled completely when equation 2.15 is used, may here give rise to artefacts. Nevertheless, the application of relation 2.23 will correctly retrieve the phases of all arrivals. That is why relation 2.23 is considered acceptable for SI in practical applications.

### ■ 2.1.3 SI relation for impulsive sources in an acoustic medium with a free surface

Let the medium  $\mathbb{D}$  represent part of the Earth and be bounded by a free surface. In that case, the boundary  $\partial\mathbb{D}$  can be written as consisting of two parts:  $\partial\mathbb{D}_0$ , coinciding with the free surface, and  $\partial\mathbb{D}_m$ , representing the part of the boundary in the subsurface. The integral on the right-hand side of equation 2.14 can be split into an integral over  $\partial\mathbb{D}_m$  and an integral over  $\partial\mathbb{D}_0$ . At the free surface, the Green's function  $\hat{G}(\mathbf{x}, \mathbf{x}_{\mathcal{A}(\mathcal{B})}, \omega)$ , which represents observed pressure, will be zero and as a result the integral over  $\partial\mathbb{D}_0$  will be zero too. This means that the right-hand side of equation 2.14 needs to be evaluated only over  $\partial\mathbb{D}_m$ . Following the same steps as above, one can conclude that in the case when a free surface is present, to retrieve the Green's function in the left-hand side of equation 2.23, one needs to evaluate the right-hand side only over  $\partial\mathbb{D}_m$ , i.e., one needs to have sources only in the subsurface. Intuitively, one can look at the free surface as a mirror that reflects the subsurface sources and creates an illusion of sources distributed over a closed boundary.

### ■ 2.1.4 SI relation for transient sources in acoustic medium

In the previous subsection, the sources along the boundary  $\partial\mathbb{D}$  were taken to be impulsive. In practice, one will have to deal with band-limited sources characterized by a wavelet  $\hat{s}(\mathbf{x}, \omega)$ . Then, the observed wavefields at the points  $\mathbf{x}_{\mathcal{A}}$  and  $\mathbf{x}_{\mathcal{B}}$  in the two states are

$$\hat{p}^{obs}(\mathbf{x}_{\mathcal{A}(\mathcal{B})}, \mathbf{x}, \omega) = \hat{G}(\mathbf{x}_{\mathcal{A}(\mathcal{B})}, \mathbf{x}, \omega) \hat{s}(\mathbf{x}, \omega). \quad (2.24)$$

Substitution of equation 2.24 for states  $\mathcal{A}$  and  $\mathcal{B}$  into the SI relation 2.23 gives

$$2\Re \left\{ \hat{G}(\mathbf{x}_{\mathcal{A}}, \mathbf{x}_{\mathcal{B}}, \omega) \right\} \hat{S}_0(\omega) \approx \frac{2}{\rho c} \oint_{\partial\mathbb{D}} \hat{F}(\mathbf{x}, \omega) \hat{p}^{obs*}(\mathbf{x}_{\mathcal{A}}, \mathbf{x}, \omega) \hat{p}^{obs}(\mathbf{x}_{\mathcal{B}}, \mathbf{x}, \omega) d^2\mathbf{x}, \quad (2.25)$$

where

$$\hat{F}(\mathbf{x}, \omega) = \frac{\hat{S}_0(\omega)}{\hat{S}(\mathbf{x}, \omega)} \quad (2.26)$$

is a shaping filter with  $\hat{S}(\mathbf{x}, \omega) = \hat{s}^*(\mathbf{x}, \omega) \hat{s}(\mathbf{x}, \omega)$  the power spectrum of the sources along  $\partial\mathbb{D}$  and  $\hat{S}_0(\omega)$  an average, arbitrarily chosen power spectrum. The SI relation 2.25 can be used when separate recordings can be taken at  $\mathbf{x}_{\mathcal{A}}$  and  $\mathbf{x}_{\mathcal{B}}$  from each of the transient sources on  $\partial\mathbb{D}$ . The shaping filter  $\hat{F}(\mathbf{x}, \omega)$  compensates for the different power spectra of the sources. This requires that these power spectra are known.

### ■ 2.1.5 SI relation for noise sources in acoustic medium

It is not always possible to record separate responses from the sources on  $\partial\mathbb{D}$ , as required for the application of SI relation 2.25. Often, the sources will be overlapping in time or one may not even know exactly when the sources were active. In such cases, there is an alternative solution if one may assume the sources to be mutually temporally uncorrelated with equal power spectrum  $\hat{S}(\omega)$  and to be acting simultaneously. This means that at the observation points  $\mathbf{x}_{\mathcal{A}}$  and  $\mathbf{x}_{\mathcal{B}}$ , the recorded wavefields will be

$$\hat{p}^{obs}(\mathbf{x}_{\mathcal{A}}, \omega) = \oint_{\partial\mathbb{D}} \hat{G}(\mathbf{x}_{\mathcal{A}}, \mathbf{x}, \omega) \hat{N}(\mathbf{x}, \omega) d^2\mathbf{x}, \quad (2.27a)$$

$$\hat{p}^{obs}(\mathbf{x}_{\mathcal{B}}, \omega) = \oint_{\partial\mathbb{D}} \hat{G}(\mathbf{x}_{\mathcal{B}}, \mathbf{x}', \omega) \hat{N}(\mathbf{x}', \omega) d^2\mathbf{x}', \quad (2.27b)$$

where  $\hat{N}(\mathbf{x}, \omega)$  and  $\hat{N}(\mathbf{x}', \omega)$  are the spectra of the sources at  $\mathbf{x}$  and  $\mathbf{x}'$ , respectively. Because the sources are assumed uncorrelated,

$$\langle \hat{N}^*(\mathbf{x}, \omega) \hat{N}(\mathbf{x}', \omega) \rangle = \delta(\mathbf{x} - \mathbf{x}') \hat{S}(\omega), \quad (2.28)$$

where  $\langle \bullet \rangle$  stands for spatial ensemble average. In such a case, the correlation of the observed wavefields at  $\mathbf{x}_A$  and  $\mathbf{x}_B$  can be written as

$$\langle \hat{p}^{obs*}(\mathbf{x}_A, \omega) \hat{p}^{obs}(\mathbf{x}_B, \omega) \rangle = \oint_{\partial\mathbb{D}} \hat{G}^*(\mathbf{x}_A, \mathbf{x}, \omega) \hat{G}(\mathbf{x}_B, \mathbf{x}, \omega) \hat{S}(\omega) d^2\mathbf{x}. \quad (2.29)$$

Comparing equation 2.29 to equation 2.23, it can be concluded that

$$2\Re \left\{ \hat{G}(\mathbf{x}_A, \mathbf{x}_B, \omega) \right\} \hat{S}(\omega) \approx \frac{2}{\rho c} \langle \hat{p}^{obs*}(\mathbf{x}_A, \omega) \hat{p}^{obs}(\mathbf{x}_B, \omega) \rangle. \quad (2.30)$$

The above relation is very easy to apply in practice – one only needs to install seismic receivers, record the noise responses, and then crosscorrelate the recorded responses following equation 2.30. A disadvantage is that no compensation can be applied for the different spectra of the different sources. As the sources are assumed uncorrelated, they can be called "noise sources" and the recorded wavefields can be called "noise" in the sense that one may not be able to see any clear arrivals. Nevertheless, what is recorded from such sources are propagating fields. The advantage of using relation 2.30 is that one does not need to have any a priori information about the sources. In practice, though, it will be difficult to find simultaneously acting noise sources. It will be most likely that the noise sources will be acting separately in time or will be partly overlapping in time. For this reason, to ensure the fulfillment of the assumption that the sources are uncorrelated in time, the noise recordings should be very long. In such a case, the ensemble average is then approximated by averaging over different time windows.

### ■ 2.1.6 SI relations for impulsive sources in an elastic medium

For an elastic medium, making use of the elastic-case column in Table 2.1, the reciprocity relations 2.5 and 2.9 can be rewritten as

$$\begin{aligned} \int_{\mathbb{D}} \left\{ -\hat{\tau}_{ij,A}(\mathbf{x}, \omega) \hat{h}_{ij,B}(\mathbf{x}, \omega) - \hat{v}_{i,A}(\mathbf{x}, \omega) \hat{f}_{i,B}(\mathbf{x}, \omega) \right. \\ \left. + \hat{h}_{ij,A}(\mathbf{x}, \omega) \hat{\tau}_{ij,B}(\mathbf{x}, \omega) + \hat{f}_{i,A}(\mathbf{x}, \omega) \hat{v}_{i,B}(\mathbf{x}, \omega) \right\} d^3\mathbf{x} = \\ \oint_{\partial\mathbb{D}} \left\{ \hat{v}_{i,A}(\mathbf{x}, \omega) \hat{\tau}_{ij,B}(\mathbf{x}, \omega) - \hat{\tau}_{ij,A}(\mathbf{x}, \omega) \hat{v}_{i,B}(\mathbf{x}, \omega) \right\} n_j d^2\mathbf{x} \quad (2.31) \end{aligned}$$

and

$$\begin{aligned} & \int_{\mathbb{D}} \left\{ -\hat{\tau}_{ij,\mathcal{A}}^*(\mathbf{x}, \omega) \hat{h}_{ij,\mathcal{B}}(\mathbf{x}, \omega) + \hat{v}_{i,\mathcal{A}}^*(\mathbf{x}, \omega) \hat{f}_{i,\mathcal{B}}(\mathbf{x}, \omega) \right. \\ & \quad \left. - \hat{h}_{ij,\mathcal{A}}^*(\mathbf{x}, \omega) \hat{\tau}_{ij,\mathcal{B}}(\mathbf{x}, \omega) + \hat{f}_{i,\mathcal{A}}^*(\mathbf{x}, \omega) \hat{v}_{i,\mathcal{B}}(\mathbf{x}, \omega) \right\} d^3\mathbf{x} = \\ & \oint_{\partial\mathbb{D}} \left\{ -\hat{v}_{i,\mathcal{A}}^*(\mathbf{x}, \omega) \hat{\tau}_{ij,\mathcal{B}}(\mathbf{x}, \omega) - \hat{\tau}_{ij,\mathcal{A}}^*(\mathbf{x}, \omega) \hat{v}_{i,\mathcal{B}}(\mathbf{x}, \omega) \right\} n_j d^2\mathbf{x}, \quad (2.32) \end{aligned}$$

respectively.

Just like in the acoustic case, certain choices are made about the wavefields and the source fields in the states  $\mathcal{A}$  and  $\mathcal{B}$ . Here, the choice is for impulsive point sources of external volume force density  $\hat{f}_i(\mathbf{x}, \omega)$  at points  $\mathbf{x}_{\mathcal{A}}$  and  $\mathbf{x}_{\mathcal{B}}$  in  $\mathbb{D}$  for states  $\mathcal{A}$  and  $\mathcal{B}$ , respectively, while the external deformation rate density  $\hat{h}_{ij}(\mathbf{x}, \omega)$  is taken to be zero. Then, the particle velocity  $\hat{v}_i(\mathbf{x}, \omega)$  at  $\mathbf{x}$  in both states can be defined as the observed impulse responses (Green's functions  $\hat{G}_{r,p(q)}^{v,f}(\mathbf{x}, \mathbf{x}_{\mathcal{A}(\mathcal{B})}, \omega)$ , see Table 2.3). The expressions for the stresses observed at  $\mathbf{x}$  for states  $\mathcal{A}$  and  $\mathcal{B}$  are obtained from the substitution of the corresponding quantities for  $\hat{f}_i(\mathbf{x}, \omega)$ ,  $\hat{h}_{ij}(\mathbf{x}, \omega)$ , and  $\hat{v}_i(\mathbf{x}, \omega)$  from Table 2.3 into the matrix-vector equation 2.1 for an elastic medium and the usage of the inverse of the compliance, which is the stiffness tensor  $c_{ijkl}$  obeying  $c_{ijkl} s_{klmn} = s_{ijkl} c_{klmn} = \frac{1}{2} (\delta_{im} \delta_{jn} + \delta_{in} \delta_{jm})$ .

Substitution of the expressions in the middle and right columns of Table 2.3 for their corresponding quantities in the convolution-type reciprocity theorem 2.31 and the use of the sifting property of the delta function, results in

$$\begin{aligned} & -\hat{G}_{q,p}^{v,f}(\mathbf{x}_{\mathcal{B}}, \mathbf{x}_{\mathcal{A}}, \omega) + \hat{G}_{p,q}^{v,f}(\mathbf{x}_{\mathcal{A}}, \mathbf{x}_{\mathcal{B}}, \omega) = \\ & \quad \oint_{\partial\mathbb{D}} \left\{ \hat{G}_{i,p}^{v,f}(\mathbf{x}, \mathbf{x}_{\mathcal{A}}, \omega) \hat{G}_{ij,q}^{\tau,f}(\mathbf{x}, \mathbf{x}_{\mathcal{B}}, \omega) \right. \\ & \quad \left. - \left( \hat{G}_{ij,p}^{\tau,f}(\mathbf{x}, \mathbf{x}_{\mathcal{A}}, \omega) \right) \hat{G}_{i,q}^{v,f}(\mathbf{x}, \mathbf{x}_{\mathcal{B}}, \omega) \right\} n_j d^2\mathbf{x}. \quad (2.33) \end{aligned}$$

The right-hand side of equation 2.33 represents a surface integral over products of causal-in-time Green's functions. If the surface of integration  $\partial\mathbb{D}$  is chosen to be a sphere with infinite radius  $\Delta \rightarrow \infty$ , the right-hand side of equation 2.33 will go to zero as it will be of order  $O(\Delta^{-1})$ . If the right-hand side vanishes on this  $\partial\mathbb{D}$ , then, because it is independent of the choice of the

boundary, it should vanish for any choice of  $\partial\mathbb{D}$  as long as the points  $\mathbf{x}_A$  and  $\mathbf{x}_B$  are inside it. This results in the elastodynamic source-receiver reciprocity relation

$$\hat{G}_{q,p}^{v,f}(\mathbf{x}_B, \mathbf{x}_A, \omega) = \hat{G}_{p,q}^{v,f}(\mathbf{x}_A, \mathbf{x}_B, \omega). \quad (2.34)$$

If, though, the choice is for impulsive point sources of external deformation rate density at the point  $\mathbf{x}_B$  in  $\mathbb{D}$  for state  $\mathcal{B}$ , while for state  $\mathcal{A}$  the choice is for a source of external volume force density at  $\mathbf{x}_A$ , see Table 2.4, then the substitution of the parameters from Table 2.4 into the reciprocity relation 2.31 followed by the same reasoning as above, will produce

$$\hat{G}_{qr,p}^{\tau,f}(\mathbf{x}_B, \mathbf{x}_A, \omega) = \hat{G}_{p,qr}^{v,h}(\mathbf{x}_A, \mathbf{x}_B, \omega). \quad (2.35)$$

Let one now substitute the quantities from the middle and the right columns of Table 2.3 into their corresponding places in the correlation-type elastodynamic reciprocity relation 2.32. Making use of the sifting property of the

Parameter	State $\mathcal{A}$	State $\mathcal{B}$
$\hat{f}_i(\mathbf{x}, \omega)$	$\delta(\mathbf{x} - \mathbf{x}_A) \delta_{ip}$	$\delta(\mathbf{x} - \mathbf{x}_B) \delta_{iq}$
$\hat{h}_{ij}(\mathbf{x}, \omega)$	0	0
$\hat{v}_i(\mathbf{x}, \omega)$	$\hat{G}_{i,p}^{v,f}(\mathbf{x}, \mathbf{x}_A, \omega)$	$\hat{G}_{i,q}^{v,f}(\mathbf{x}, \mathbf{x}_B, \omega)$
$\hat{\tau}_{ij}(\mathbf{x}, \omega)$	$\frac{1}{j\omega} c_{ijkl}(\mathbf{x}) \partial_l \hat{G}_{k,p}^{v,f}(\mathbf{x}, \mathbf{x}_A, \omega)$ $\triangleq \hat{G}_{ij,p}^{\tau,f}(\mathbf{x}, \mathbf{x}_A, \omega)$	$\frac{1}{j\omega} c_{ijkl}(\mathbf{x}) \partial_l \hat{G}_{k,q}^{v,f}(\mathbf{x}, \mathbf{x}_B, \omega)$ $\triangleq \hat{G}_{ij,q}^{\tau,f}(\mathbf{x}, \mathbf{x}_B, \omega)$

**Table 2.3:** Choice of wavefield and source parameters for the elastodynamic states  $\mathcal{A}$  and  $\mathcal{B}$ , to be used in two-way wavefield elastodynamic reciprocity theorems. The superscripts in the Green's function notation represent the receiver quantity (particle velocity  $v$  or stress  $\tau$ ) and source quantity (force  $f$  or deformation rate  $h$ ), respectively, while the subscripts represent the components of the observed quantity ( $i, j$ ) and the source components ( $p, q$ ), respectively.

delta function gives

$$\begin{aligned} \left\{ \hat{G}_{q,p}^{v,f}(\mathbf{x}_B, \mathbf{x}_A, \omega) \right\}^* + \hat{G}_{p,q}^{v,f}(\mathbf{x}_A, \mathbf{x}_B, \omega) = \\ - \oint_{\partial\mathbb{D}} \left\{ \left( \hat{G}_{i,p}^{v,f}(\mathbf{x}, \mathbf{x}_A, \omega) \right)^* \hat{G}_{ij,q}^{\tau,f}(\mathbf{x}, \mathbf{x}_B, \omega) \right. \\ \left. + \left( \hat{G}_{ij,p}^{\tau,f}(\mathbf{x}, \mathbf{x}_A, \omega) \right)^* \hat{G}_{i,q}^{v,f}(\mathbf{x}, \mathbf{x}_B, \omega) \right\} n_j d^2\mathbf{x}. \end{aligned} \quad (2.36)$$

Further application of the source-receiver reciprocities 2.34 and 2.35 to both sides of equation 2.36 results in

$$\begin{aligned} 2\Re \left\{ \hat{G}_{p,q}^{v,f}(\mathbf{x}_A, \mathbf{x}_B, \omega) \right\} = \\ - \oint_{\partial\mathbb{D}} \left\{ \left( \hat{G}_{p,i}^{v,f}(\mathbf{x}_A, \mathbf{x}, \omega) \right)^* \hat{G}_{q,ij}^{v,h}(\mathbf{x}_B, \mathbf{x}, \omega) \right. \\ \left. + \left( \hat{G}_{p,ij}^{v,h}(\mathbf{x}_A, \mathbf{x}, \omega) \right)^* \hat{G}_{q,i}^{v,f}(\mathbf{x}_B, \mathbf{x}, \omega) \right\} n_j d^2\mathbf{x}. \end{aligned} \quad (2.37)$$

In the time domain, the products on the right-hand side of the above equation correspond to crosscorrelations, while the left-hand side corresponds to a Green's function and its time-reversed version. In this way, relation

Parameter	State $\mathcal{A}$	State $\mathcal{B}$
$\hat{f}_i(\mathbf{x}, \omega)$	$\delta(\mathbf{x} - \mathbf{x}_A) \delta_{ip}$	0
$\hat{h}_{ij}(\mathbf{x}, \omega)$	0	$\delta(\mathbf{x} - \mathbf{x}_B) \delta_{iq} \delta_{jr}$
$\hat{v}_i(\mathbf{x}, \omega)$	$\hat{G}_{i,p}^{v,f}(\mathbf{x}, \mathbf{x}_A, \omega)$	$\frac{1}{j\omega\rho} \Delta_{ijkl} \partial_j \hat{G}_{kl,qr}^{\tau,h}(\mathbf{x}, \mathbf{x}_B, \omega)$ $\triangleq \hat{G}_{i,qr}^{v,h}(\mathbf{x}, \mathbf{x}_B, \omega)$
$\hat{\tau}_{ij}(\mathbf{x}, \omega)$	$\frac{1}{j\omega} c_{ijkl}(\mathbf{x}) \partial_l \hat{G}_{k,p}^{v,f}(\mathbf{x}, \mathbf{x}_A, \omega)$ $\triangleq \hat{G}_{ij,p}^{\tau,f}(\mathbf{x}, \mathbf{x}_A, \omega)$	$\hat{G}_{ij,qr}^{\tau,h}(\mathbf{x}, \mathbf{x}_B, \omega)$

**Table 2.4:** Alternative choice for wavefield and source parameters for the elastodynamic states  $\mathcal{A}$  and  $\mathcal{B}$  to be used in two-way wavefield elastodynamic convolution-type reciprocity theorem.

2.37 provides the possibility to retrieve the complete Green's function and its time-reversed version between the points  $\mathbf{x}_A$  and  $\mathbf{x}_B$  by constructive and destructive interference (summation) of crosscorrelations of observed Green's functions  $\hat{G}_{p,i}^{v,f}(\mathbf{x}_{A(B)}, \mathbf{x}, \omega)$ , due to impulsive force sources on  $\partial\mathbb{D}$ , and observed Green's functions  $\hat{G}_{q,ij}^{v,h}(\mathbf{x}_{A(B)}, \mathbf{x}, \omega) n_j$  due to impulsive deformation sources on  $\partial\mathbb{D}$ . Equation 2.37 is exact and valid for any lossless inhomogeneous (inside, as well as outside  $\partial\mathbb{D}$ ) elastic medium. Van Manen et al. [2006] developed an effective modelling scheme based on a relation very similar to equation 2.37.

But just as in the acoustic case, in the application of this relation one faces the two difficulties of having to perform two correlations separately and needing the responses of two different types of sources. To overcome these problems, it is assumed that in a small region around  $\partial\mathbb{D}$  the medium is homogeneous and isotropic. Because of this, the observed wavefields can be written as simple sum of observed P- and S-waves. Thus, the Green's functions observed at  $\mathbf{x}$  due to sources at  $\mathbf{x}_A$  and  $\mathbf{x}_B$  can be represented in terms of Green's function potentials for observed P- and S-waves [Wapenaar and Berkhout, 1989; Aki and Richards, 2002]:

$$\begin{aligned} \hat{G}_{i,p(q)}^{v,f}(\mathbf{x}, \mathbf{x}_{A(B)}, \omega) = \\ \frac{-1}{j\omega\rho} \left\{ \partial_i \hat{G}_{0,p(q)}^{\phi,f}(\mathbf{x}, \mathbf{x}_{A(B)}, \omega) + \epsilon_{ijk} \partial_j \hat{G}_{k,p(q)}^{\phi,f}(\mathbf{x}, \mathbf{x}_{A(B)}, \omega) \right\} \\ \text{with } \partial_k \hat{G}_{k,p(q)}^{\phi,f}(\mathbf{x}, \mathbf{x}_{A(B)}, \omega) = 0 \quad (2.38) \end{aligned}$$

where the superscript  $\phi$  means that the observed quantity is a P-wave when the left subscript is 0, or an S-wave when the left subscript is  $k$ . The Green's function potentials obey the Helmholtz equations

$$\partial_i \partial_i \hat{G}_{0,p(q)}^{\phi,f}(\mathbf{x}, \mathbf{x}_{A(B)}, \omega) + \frac{\omega^2}{c_P^2} \hat{G}_{0,p(q)}^{\phi,f}(\mathbf{x}, \mathbf{x}_{A(B)}, \omega) = 0 \quad (2.39a)$$

$$\partial_i \partial_i \hat{G}_{k,p(q)}^{\phi,f}(\mathbf{x}, \mathbf{x}_{A(B)}, \omega) + \frac{\omega^2}{c_S^2} \hat{G}_{k,p(q)}^{\phi,f}(\mathbf{x}, \mathbf{x}_{A(B)}, \omega) = 0, \quad (2.39b)$$

where  $c_P$  and  $c_S$  are the P- and S-wave propagation velocities in the medium, respectively. The Green's function potentials can be explicitly written in

terms of the observed Green's functions as

$$\hat{G}_{0,p(q)}^{\phi,f}(\mathbf{x}, \mathbf{x}_{\mathcal{A}(\mathcal{B})}, \omega) = -\frac{\rho c_P^2}{j\omega} \partial_i \hat{G}_{i,p(q)}^{v,f}(\mathbf{x}, \mathbf{x}_{\mathcal{A}(\mathcal{B})}, \omega) \quad (2.40a)$$

$$\hat{G}_{k,p(q)}^{\phi,f}(\mathbf{x}, \mathbf{x}_{\mathcal{A}(\mathcal{B})}, \omega) = \frac{\rho c_S^2}{j\omega} \epsilon_{kji} \partial_j \hat{G}_{i,p(q)}^{v,f}(\mathbf{x}, \mathbf{x}_{\mathcal{A}(\mathcal{B})}, \omega). \quad (2.40b)$$

Furthermore, at the boundary  $\partial\mathbb{D}$  the Green's function potentials can be divided into inward- and outward-propagating parts:

$$\hat{G}_{K,p(q)}^{\phi,f}(\mathbf{x}, \mathbf{x}_{\mathcal{A}(\mathcal{B})}, \omega) = \hat{G}_{K,p(q)}^{\phi,f,in}(\mathbf{x}, \mathbf{x}_{\mathcal{A}(\mathcal{B})}, \omega) + \hat{G}_{K,p(q)}^{\phi,f,out}(\mathbf{x}, \mathbf{x}_{\mathcal{A}(\mathcal{B})}, \omega), \quad (2.41)$$

where  $K = 0, 1, 2, 3$ . Expressions for the Green's functions  $\hat{G}_{ij,p}^{\tau,f}(\mathbf{x}, \mathbf{x}_{\mathcal{A}}, \omega)$  and  $\hat{G}_{ij,q}^{\tau,f}(\mathbf{x}, \mathbf{x}_{\mathcal{B}}, \omega)$  in terms of the Green's function potentials can be written as

$$\begin{aligned} \hat{G}_{ij,p(q)}^{\tau,f}(\mathbf{x}, \mathbf{x}_{\mathcal{A}(\mathcal{B})}, \omega) = & \frac{-1}{(j\omega)^2 \rho} \left\{ c_{ijkl} \partial_l \partial_k \hat{G}_{0,p(q)}^{\phi,f}(\mathbf{x}, \mathbf{x}_{\mathcal{A}(\mathcal{B})}, \omega) \right. \\ & \left. + c_{ijkl} \partial_l \epsilon_{kmn} \partial_m \hat{G}_{n,p(q)}^{\phi,f}(\mathbf{x}, \mathbf{x}_{\mathcal{A}(\mathcal{B})}, \omega) \right\}. \quad (2.42) \end{aligned}$$

Substitution of equation 2.38 and equation 2.42 in conjunction with equation 2.41 for states  $\mathcal{A}$  and  $\mathcal{B}$  into the right-hand side of equation 2.36 results in products between inward- and outward-propagating P-waves and S-waves. [Wapenaar and Berkhout \[1989\]](#) show that for a horizontal boundary, products between only P-waves and products between only S-waves remain, while the cross-products between P- and S-waves cancel each other. They show further that only products between waves traveling in opposite directions will remain. I.e., for a horizontal boundary  $\partial\mathbb{D}$ , the right-hand side of equation 2.36 can be written as

$$\begin{aligned} \frac{2}{j\omega\rho} \int_{\partial\mathbb{D}} \left\{ \left( \partial_3 \hat{G}_{0,p}^{\phi,f,in}(\mathbf{x}, \mathbf{x}_{\mathcal{A}}, \omega) \right)^* \hat{G}_{0,q}^{\phi,f,in}(\mathbf{x}, \mathbf{x}_{\mathcal{B}}, \omega) \right. \\ + \left( \partial_3 \hat{G}_{0,p}^{\phi,f,out}(\mathbf{x}, \mathbf{x}_{\mathcal{A}}, \omega) \right)^* \hat{G}_{0,q}^{\phi,f,out}(\mathbf{x}, \mathbf{x}_{\mathcal{B}}, \omega) \\ + \left( \partial_3 \hat{G}_{k,p}^{\phi,f,in}(\mathbf{x}, \mathbf{x}_{\mathcal{A}}, \omega) \right)^* \hat{G}_{k,q}^{\phi,f,in}(\mathbf{x}, \mathbf{x}_{\mathcal{B}}, \omega) \\ \left. + \left( \partial_3 \hat{G}_{k,p}^{\phi,f,out}(\mathbf{x}, \mathbf{x}_{\mathcal{A}}, \omega) \right)^* \hat{G}_{k,q}^{\phi,f,out}(\mathbf{x}, \mathbf{x}_{\mathcal{B}}, \omega) \right\} n_3 d^2\mathbf{x} \quad (2.43) \end{aligned}$$



(note that the complex conjugation reverses the propagation direction, hence, all terms are indeed products of waves traveling in the opposite directions). The above result is not exact because the evanescent waves that propagate parallel to the horizontal boundary were neglected.

The integral will now be analyzed for an arbitrary closed surface  $\partial\mathbb{D}$ . In the high-frequency regime, the integral on the right-hand side of equation 2.36 receives its main contributions from stationary points along the boundary  $\partial\mathbb{D}$ . At such stationary points a local coordinate system is chosen, in which the local  $x_3$  axis is in the direction of the outward-pointing normal on  $\partial\mathbb{D}$ . For each of these local coordinate systems, one obtains a result similar to the result in 2.43. When all the stationary points are accounted for, the total result would include also waves that propagate in the horizontal direction in the global coordinate system, including evanescent waves. As a result of this reasoning, going back to the global coordinate system, equation 2.36 can be written as

$$\begin{aligned}
2\Re \left\{ \hat{G}_{p,q}^{v,f}(\mathbf{x}_A, \mathbf{x}_B, \omega) \right\} = & \\
& \frac{2}{j\omega\rho} \oint_{\partial\mathbb{D}} \left\{ \left( \partial_j \hat{G}_{0,p}^{\phi,f,in}(\mathbf{x}, \mathbf{x}_A, \omega) \right)^* \hat{G}_{0,q}^{\phi,f,in}(\mathbf{x}, \mathbf{x}_B, \omega) \right. \\
& + \left( \partial_j \hat{G}_{0,p}^{\phi,f,out}(\mathbf{x}, \mathbf{x}_A, \omega) \right)^* \hat{G}_{0,q}^{\phi,f,out}(\mathbf{x}, \mathbf{x}_B, \omega) \\
& + \left( \partial_j \hat{G}_{k,p}^{\phi,f,in}(\mathbf{x}, \mathbf{x}_A, \omega) \right)^* \hat{G}_{k,q}^{\phi,f,in}(\mathbf{x}, \mathbf{x}_B, \omega) \\
& \left. + \left( \partial_j \hat{G}_{k,p}^{\phi,f,out}(\mathbf{x}, \mathbf{x}_A, \omega) \right)^* \hat{G}_{k,q}^{\phi,f,out}(\mathbf{x}, \mathbf{x}_B, \omega) \right\} n_j d^2\mathbf{x}. \quad (2.44)
\end{aligned}$$

As the medium in a small region around  $\partial\mathbb{D}$  is assumed homogeneous and isotropic, the Green's functions observed at  $\mathbf{x}_A$  and  $\mathbf{x}_B$  due to sources at  $\mathbf{x}$  can be represented in terms of Green's function potentials from P- and S-wave sources [Wapenaar and Berkhout, 1989]:

$$\begin{aligned}
\hat{G}_{p(q),i}^{v,f}(\mathbf{x}_{A(B)}, \mathbf{x}, \omega) = & \\
& \frac{-1}{j\omega\rho} \left\{ \partial_i \hat{G}_{p(q),0}^{v,\phi}(\mathbf{x}_{A(B)}, \mathbf{x}, \omega) + \epsilon_{ijk} \partial_j \hat{G}_{p(q),k}^{v,\phi}(\mathbf{x}_{A(B)}, \mathbf{x}, \omega) \right\} \\
& \text{with } \partial_k \hat{G}_{p(q),k}^{v,\phi}(\mathbf{x}_{A(B)}, \mathbf{x}, \omega) = 0. \quad (2.45)
\end{aligned}$$

Then,

$$\hat{G}_{p(q),0}^{v,\phi}(\mathbf{x}_{\mathcal{A}(\mathcal{B})}, \mathbf{x}, \omega) = -\frac{\rho c_P^2}{j\omega} \partial_i \hat{G}_{p(q),i}^{v,f}(\mathbf{x}_{\mathcal{A}(\mathcal{B})}, \mathbf{x}, \omega), \quad (2.46a)$$

$$\hat{G}_{p(q),k}^{v,\phi}(\mathbf{x}_{\mathcal{A}(\mathcal{B})}, \mathbf{x}, \omega) = \frac{\rho c_S^2}{j\omega} \epsilon_{kji} \partial_j \hat{G}_{p(q),i}^{v,f}(\mathbf{x}_{\mathcal{A}(\mathcal{B})}, \mathbf{x}, \omega). \quad (2.46b)$$

The use of reciprocity relations 2.34 together with equations 2.40 and 2.46, results in the reciprocity relation for the Green's function potentials

$$\hat{G}_{K,p(q)}^{\phi,f,in}(\mathbf{x}, \mathbf{x}_{\mathcal{A}(\mathcal{B})}, \omega) = \hat{G}_{p(q),K}^{v,\phi,out}(\mathbf{x}_{\mathcal{A}(\mathcal{B})}, \mathbf{x}, \omega), \quad (2.47a)$$

$$\hat{G}_{K,p(q)}^{\phi,f,out}(\mathbf{x}, \mathbf{x}_{\mathcal{A}(\mathcal{B})}, \omega) = \hat{G}_{p(q),K}^{v,\phi,in}(\mathbf{x}_{\mathcal{A}(\mathcal{B})}, \mathbf{x}, \omega), \quad (2.47b)$$

where  $K = 0, 1, 2, 3$ . Thus, relation 2.44 can be rewritten as

$$\begin{aligned} 2\Re \left\{ \hat{G}_{p,q}^{v,f}(\mathbf{x}_{\mathcal{A}}, \mathbf{x}_{\mathcal{B}}, \omega) \right\} = \\ \frac{2}{j\omega\rho} \oint_{\partial\mathbb{D}} \left\{ \left( \partial_j \hat{G}_{p,K}^{v,\phi,in}(\mathbf{x}_{\mathcal{A}}, \mathbf{x}, \omega) \right)^* \hat{G}_{q,K}^{v,\phi,in}(\mathbf{x}_{\mathcal{B}}, \mathbf{x}, \omega) \right. \\ \left. + \left( \partial_j \hat{G}_{p,K}^{v,\phi,out}(\mathbf{x}_{\mathcal{A}}, \mathbf{x}, \omega) \right)^* \hat{G}_{q,K}^{v,\phi,out}(\mathbf{x}_{\mathcal{B}}, \mathbf{x}, \omega) \right\} n_j d^2\mathbf{x}. \quad (2.48) \end{aligned}$$

Making use of the equations 2.47 in conjunction with equation 2.41, one can rewrite equation 2.48 as

$$\begin{aligned} 2\Re \left\{ \hat{G}_{p,q}^{v,f}(\mathbf{x}_{\mathcal{A}}, \mathbf{x}_{\mathcal{B}}, \omega) \right\} + \text{ghosts} = \\ \frac{2}{j\omega\rho} \oint_{\partial\mathbb{D}} \left\{ \left( \partial_j \hat{G}_{p,K}^{v,\phi}(\mathbf{x}_{\mathcal{A}}, \mathbf{x}, \omega) \right)^* \hat{G}_{q,K}^{v,\phi}(\mathbf{x}_{\mathcal{B}}, \mathbf{x}, \omega) \right\} n_j d^2\mathbf{x}, \quad (2.49) \end{aligned}$$

where

$$\begin{aligned} \text{ghosts} = \\ \frac{2}{j\omega\rho} \oint_{\partial\mathbb{D}} \left\{ \left( \partial_j \hat{G}_{p,K}^{v,\phi,in}(\mathbf{x}_{\mathcal{A}}, \mathbf{x}, \omega) \right)^* \hat{G}_{q,K}^{v,\phi,out}(\mathbf{x}_{\mathcal{B}}, \mathbf{x}, \omega) \right. \\ \left. + \left( \partial_j \hat{G}_{p,K}^{v,\phi,out}(\mathbf{x}_{\mathcal{A}}, \mathbf{x}, \omega) \right)^* \hat{G}_{q,K}^{v,\phi,in}(\mathbf{x}_{\mathcal{B}}, \mathbf{x}, \omega) \right\} n_j d^2\mathbf{x}. \quad (2.50) \end{aligned}$$

The left-hand side of equation 2.49 contains not only the retrieved Green's function and its time-reversed version, but also ghosts that result from the

crosscorrelations on the right-hand side (see Figure 3.30 for examples). When the sources are randomly distributed in space, i.e., when the surface  $\partial\mathbb{D}$  is sufficiently irregular, the ghost correlation products will not interfere coherently and the ghost terms will be strongly weakened and can be ignored. At the same time, the retrieved Green's function will contain all scattered fields from inside and outside  $\partial\mathbb{D}$  (see Figure 3.32). If the medium outside  $\partial\mathbb{D}$  is taken to be homogeneous with propagation velocity  $c_P$  and  $c_S$  for P- and S-waves, respectively, and mass density  $\rho$ , the outward-propagating part of the Green's function potentials will not come back and then  $ghosts = 0$ .

In the high-frequency regime, the normal derivatives of each constituent of the Green's function potentials can be written as

$$\partial_j \hat{G}_{p(q),K,w}^{v,\phi,in}(\mathbf{x}_{\mathcal{A}(\mathcal{B})}, \mathbf{x}, \omega) n_j = -j \frac{\omega}{c^K} |\cos \alpha_{K,w}(\mathbf{x})| \hat{G}_{p(q),K,w}^{v,\phi,in}(\mathbf{x}_{\mathcal{A}(\mathcal{B})}, \mathbf{x}, \omega) \quad (2.51a)$$

$$\partial_j \hat{G}_{p(q),K,w}^{v,\phi,out}(\mathbf{x}_{\mathcal{A}(\mathcal{B})}, \mathbf{x}, \omega) n_j = +j \frac{\omega}{c^K} |\cos \alpha_{K,w}(\mathbf{x})| \hat{G}_{p(q),K,w}^{v,\phi,out}(\mathbf{x}_{\mathcal{A}(\mathcal{B})}, \mathbf{x}, \omega), \quad (2.51b)$$

where  $c^K = c_P$  for  $K = 0$  and  $c^K = c_S$  for  $K = 1, 2, 3$ . Further, if  $\partial\mathbb{D}$  is taken to be a sphere with a sufficiently large radius, then all rays are normal to  $\partial\mathbb{D}$  and consequently  $\alpha = 0$ . Consequently, equation 2.49 can finally be expressed as

$$2\Re \left\{ \hat{G}_{p,q}^{v,f}(\mathbf{x}_{\mathcal{A}}, \mathbf{x}_{\mathcal{B}}, \omega) \right\} \approx \frac{2}{\rho c^K} \oint_{\partial\mathbb{D}} \left( \hat{G}_{p,K}^{v,\phi}(\mathbf{x}_{\mathcal{A}}, \mathbf{x}, \omega) \right)^* \hat{G}_{q,K}^{v,\phi}(\mathbf{x}_{\mathcal{B}}, \mathbf{x}, \omega) d^2\mathbf{x}. \quad (2.52)$$

The approximation in equation 2.52 involves only amplitude errors; when  $\partial\mathbb{D}$  differs significantly from a sphere these errors may be significant. Furthermore, due to incomplete destructive interference, events that would be canceled completely when equation 2.36 is used may here give rise to artefacts. Nevertheless, the application of relation 2.52 will correctly retrieve the phases of all arrivals. That is why relation 2.52 is considered acceptable for SI for practical applications.

### ■ 2.1.7 SI relation for impulsive sources in an elastic medium with a free surface

Just as in the acoustic case, the medium  $\mathbb{D}$  can be taken to be bounded (at the top) by a free surface. Then,  $\partial\mathbb{D} = \partial\mathbb{D}_m \cup \partial\mathbb{D}_0$ , where  $\partial\mathbb{D}_0$  is the part coinciding with the free surface. The integral on the right-hand side of equation 2.36 needs then to be evaluated only over  $\partial\mathbb{D}_m$  because the traction  $\hat{G}_{ij,p(q)}^{\tau,f}(\mathbf{x}, \mathbf{x}_{\mathcal{A}(\mathcal{B})}, \omega)$  is zero on  $\partial\mathbb{D}_0$ . Following the same steps as above, one can conclude that in the case when a free surface is present, to retrieve the Green's function in the left-hand side of equation 2.52, one needs to evaluate the right-hand side only over sources in the subsurface.

### ■ 2.1.8 SI relation for transient sources in an elastic medium

In practice, the sources along the boundary  $\partial\mathbb{D}$  will not be impulsive, as in the previous subsection, but will be band-limited. Let the P- and S-wave sources be characterized by a wavelet with a spectrum  $\hat{s}^K(\mathbf{x}, \omega)$  for  $K = 0, 1, 2, 3$ . Then the observed wavefields at the points  $\mathbf{x}_A$  and  $\mathbf{x}_B$  for the two states are

$$\hat{v}_{p(q),K}^{obs}(\mathbf{x}_{\mathcal{A}(\mathcal{B})}, \mathbf{x}, \omega) = \hat{G}_{p(q),k}^{v,\phi}(\mathbf{x}_{\mathcal{A}(\mathcal{B})}, \mathbf{x}, \omega) \hat{s}^K(\mathbf{x}, \omega). \quad (2.53)$$

Substitution of equation 2.53 for the two points into the SI relation 2.52 gives

$$2\Re \left\{ \hat{G}_{p,q}^{v,f}(\mathbf{x}_A, \mathbf{x}_B, \omega) \right\} \hat{S}_0(\omega) \approx \frac{2}{\rho c^K} \oint_{\partial\mathbb{D}} \hat{F}^K(\mathbf{x}, \omega) \hat{v}_{p,K}^{obs*}(\mathbf{x}_A, \mathbf{x}, \omega) \hat{v}_{q,K}^{obs}(\mathbf{x}_B, \mathbf{x}, \omega) d^2\mathbf{x}, \quad (2.54)$$

where

$$\hat{F}^K(\mathbf{x}, \omega) = \frac{\hat{S}_0(\omega)}{\hat{S}^K(\mathbf{x}, \omega)} \quad (2.55)$$

is a shaping filter with  $\hat{S}^K(\mathbf{x}, \omega) = \hat{s}^{K*}(\mathbf{x}, \omega) \hat{s}^K(\mathbf{x}, \omega)$  the power spectrum of the P- and S-wave sources along  $\partial\mathbb{D}$  and  $\hat{S}_0(\omega)$  an average, arbitrarily chosen power spectrum. The SI relation 2.53 can be used when separate recordings can be taken at  $\mathbf{x}_A$  and  $\mathbf{x}_B$  from each of the transient sources on  $\partial\mathbb{D}$ . The shaping filter  $\hat{F}^K(\mathbf{x}, \omega)$  compensates for the different power spectra of the sources. This requires that these power spectra are known.

### ■ 2.1.9 SI relation for noise sources in an elastic medium

To make use of the SI relation 2.54, one needs separate recordings from each source-type at each source position on  $\partial\mathbb{D}$ . Such information will be available only in special cases or after some preprocessing. When such recordings are not available, an alternative solution is to assume the sources to be acting simultaneously and to be mutually temporally uncorrelated with equal power spectrum  $\frac{c_P}{c_K} \hat{S}(\omega)$ . This means that at the observation points  $\mathbf{x}_A$  and  $\mathbf{x}_B$  the recorded wavefields will be

$$\hat{v}_p^{obs}(\mathbf{x}_A, \omega) = \oint_{\partial\mathbb{D}} \hat{G}_{p,K}^{v,\phi}(\mathbf{x}_A, \mathbf{x}, \omega) \hat{N}_K(\mathbf{x}, \omega) d^2\mathbf{x}, \quad (2.56a)$$

$$\hat{v}_q^{obs}(\mathbf{x}_B, \omega) = \oint_{\partial\mathbb{D}} \hat{G}_{q,L}^{v,\phi}(\mathbf{x}_B, \mathbf{x}', \omega) \hat{N}_L(\mathbf{x}', \omega) d^2\mathbf{x}', \quad (2.56b)$$

where  $\hat{N}_K(\mathbf{x}, \omega)$  and  $\hat{N}_L(\mathbf{x}', \omega)$  are the spectra of the different source types at  $\mathbf{x}$  and  $\mathbf{x}'$ , respectively. Because the sources are assumed uncorrelated for any  $K \neq L$  and  $\mathbf{x} \neq \mathbf{x}'$ ,

$$\langle \hat{N}_K^*(\mathbf{x}, \omega) \hat{N}_L(\mathbf{x}', \omega) \rangle = \frac{c_P}{c_K} \delta_{KL} \delta(\mathbf{x} - \mathbf{x}') \hat{S}(\omega). \quad (2.57)$$

Then, the correlation of the observed wavefields at  $\mathbf{x}_A$  and  $\mathbf{x}_B$  can be written as

$$\begin{aligned} \langle \hat{v}_p^{obs*}(\mathbf{x}_A, \omega) \hat{v}_q^{obs}(\mathbf{x}_B, \omega) \rangle = \\ \frac{c_P}{c_K} \oint_{\partial\mathbb{D}} \left( \hat{G}_{p,K}^{v,\phi}(\mathbf{x}_A, \mathbf{x}, \omega) \right)^* \hat{G}_{q,K}^{v,\phi}(\mathbf{x}_B, \mathbf{x}, \omega) \hat{S}(\omega) d^2\mathbf{x}. \end{aligned} \quad (2.58)$$

Comparing equation 2.58 to equation 2.52, it can be concluded that

$$2\Re \left\{ \hat{G}_{p,q}^{v,f}(\mathbf{x}_A, \mathbf{x}_B, \omega) \right\} \hat{S}(\omega) \approx \frac{2}{\rho c_P} \langle \hat{v}_p^{obs*}(\mathbf{x}_A, \omega) \hat{v}_q^{obs}(\mathbf{x}_B, \omega) \rangle. \quad (2.59)$$

The above relation is very easy to use in practice. A disadvantage is that no compensation can be applied for the different spectra of the different sources. The advantage of using relation 2.59 is that one does not need to have any a priori information about the sources. The sources can act simultaneously, be separate in time, or overlap. The sources can be active for a long time or represent short bursts of energy.

### ■ 2.1.10 EMI relations for impulsive sources

In the electromagnetic case, making use of the right-most column in Table 2.1, the reciprocity relations 2.5 and 2.9 can be rewritten as [Slob et al., 2007]

$$\begin{aligned} & \int_{\mathbb{D}} \left\{ \hat{E}_{r,\mathcal{A}}(\mathbf{x}, \omega) \hat{J}_{r,\mathcal{B}}^e(\mathbf{x}, \omega) - \hat{H}_{j,\mathcal{A}}(\mathbf{x}, \omega) \hat{J}_{j,\mathcal{B}}^m(\mathbf{x}, \omega) \right. \\ & \quad \left. - \hat{J}_{r,\mathcal{A}}^e(\mathbf{x}, \omega) \hat{E}_{r,\mathcal{B}}(\mathbf{x}, \omega) + \hat{J}_{j,\mathcal{A}}^m(\mathbf{x}, \omega) \hat{H}_{j,\mathcal{B}}(\mathbf{x}, \omega) \right\} d^3\mathbf{x} = \\ & \oint_{\partial\mathbb{D}} n_m \epsilon_{mrj} \left( \hat{H}_{j,\mathcal{A}}(\mathbf{x}, \omega) \hat{E}_{r,\mathcal{B}}(\mathbf{x}, \omega) - \hat{E}_{r,\mathcal{A}}(\mathbf{x}, \omega) \hat{H}_{j,\mathcal{B}}(\mathbf{x}, \omega) \right) d^2\mathbf{x} \end{aligned} \quad (2.60)$$

and

$$\begin{aligned} & - \int_{\mathbb{D}} \left\{ \hat{E}_{r,\mathcal{A}}^*(\mathbf{x}, \omega) \hat{J}_{r,\mathcal{B}}^e(\mathbf{x}, \omega) + \hat{H}_{j,\mathcal{A}}^*(\mathbf{x}, \omega) \hat{J}_{j,\mathcal{B}}^m(\mathbf{x}, \omega) \right. \\ & \quad \left. + \hat{J}_{r,\mathcal{A}}^{e*}(\mathbf{x}, \omega) \hat{E}_{r,\mathcal{B}}(\mathbf{x}, \omega) + \hat{J}_{j,\mathcal{A}}^{m*}(\mathbf{x}, \omega) \hat{H}_{j,\mathcal{B}}(\mathbf{x}, \omega) \right\} d^3\mathbf{x} = \\ & \oint_{\partial\mathbb{D}} n_m \epsilon_{mrj} \left( \hat{H}_{j,\mathcal{A}}^*(\mathbf{x}, \omega) \hat{E}_{r,\mathcal{B}}(\mathbf{x}, \omega) + \hat{E}_{r,\mathcal{A}}^*(\mathbf{x}, \omega) \hat{H}_{j,\mathcal{B}}(\mathbf{x}, \omega) \right) d^2\mathbf{x}, \end{aligned} \quad (2.61)$$

respectively.

A choice is made for impulsive point source of external volume density of the electric current  $\hat{J}_r^e(\mathbf{x}, \omega)$  at points  $\mathbf{x}_{\mathcal{A}}$  and  $\mathbf{x}_{\mathcal{B}}$  in  $\mathbb{D}$  for states  $\mathcal{A}$  and  $\mathcal{B}$ , respectively, while the external volume density of the magnetic current  $\hat{J}_j^m(\mathbf{x}, \omega)$  is taken to be zero. In such a way, the electric and the magnetic field vectors can be expressed in terms of Green's functions, see Table 2.5.

Substituting the expressions in the middle and right columns of Table 2.5 for their corresponding quantities in the convolution-type reciprocity theorem 2.60, making use of the sifting property of the delta function, and applying the same arguments as the ones directly after equation 2.33, yields

$$\hat{G}_{q,p}^{E,J^e}(\mathbf{x}_{\mathcal{B}}, \mathbf{x}_{\mathcal{A}}, \omega) = \hat{G}_{p,q}^{E,J^e}(\mathbf{x}_{\mathcal{A}}, \mathbf{x}_{\mathcal{B}}, \omega). \quad (2.62)$$

If, instead, a choice is made in state  $\mathcal{B}$  for a source of external volume density of the magnetic current  $\hat{J}_j^m(\mathbf{x}, \omega)$ , see Table 2.6, then following similar steps

as above would produce

$$\hat{G}_{q,p}^{H,J^e}(\mathbf{x}_B, \mathbf{x}_A, \omega) = -\hat{G}_{p,q}^{E,J^m}(\mathbf{x}_A, \mathbf{x}_B, \omega). \quad (2.63)$$

When the quantities from the middle and the right columns of Table 2.5 are substituted into their corresponding places in the correlation-type electromagnetic reciprocity relation 2.61, followed by the application of the sifting property of the delta function, results in

$$\begin{aligned} & \left\{ \hat{G}_{q,p}^{E,J^e}(\mathbf{x}_B, \mathbf{x}_A, \omega) \right\}^* + \hat{G}_{p,q}^{E,J^e}(\mathbf{x}_A, \mathbf{x}_B, \omega) = \\ & - \oint_{\partial\mathbb{D}} n_m \epsilon_{mrj} \left\{ \left( \hat{G}_{j,p}^{H,J^e}(\mathbf{x}, \mathbf{x}_A, \omega) \right)^* \hat{G}_{r,q}^{E,J^e}(\mathbf{x}, \mathbf{x}_B, \omega) \right. \\ & \quad \left. + \left( \hat{G}_{r,p}^{E,J^e}(\mathbf{x}, \mathbf{x}_A, \omega) \right)^* \hat{G}_{j,q}^{H,J^e}(\mathbf{x}, \mathbf{x}_B, \omega) \right\} d^2\mathbf{x}. \quad (2.64) \end{aligned}$$

If this is followed by the application of the reciprocity relations 2.62 and

Parameter	State $\mathcal{A}$	State $\mathcal{B}$
$\hat{J}_k^e(\mathbf{x}, \omega)$	$\delta(\mathbf{x} - \mathbf{x}_A) \delta_{kp}$	$\delta(\mathbf{x} - \mathbf{x}_B) \delta_{kq}$
$\hat{J}_j^m(\mathbf{x}, \omega)$	0	0
$\hat{E}_r(\mathbf{x}, \omega)$	$\hat{G}_{r,p}^{E,J^e}(\mathbf{x}, \mathbf{x}_A, \omega)$	$\hat{G}_{r,q}^{E,J^e}(\mathbf{x}, \mathbf{x}_B, \omega)$
$\hat{H}_i(\mathbf{x}, \omega)$	$-\frac{\zeta_{ij}}{j\omega} \epsilon_{jmr} \partial_m \hat{G}_{r,p}^{E,J^e}(\mathbf{x}, \mathbf{x}_A, \omega)$ $\triangleq \hat{G}_{i,p}^{H,J^e}(\mathbf{x}, \mathbf{x}_A, \omega)$	$-\frac{\zeta_{ij}}{j\omega} \epsilon_{jmr} \partial_m \hat{G}_{r,q}^{E,J^e}(\mathbf{x}, \mathbf{x}_B, \omega)$ $\triangleq \hat{G}_{i,q}^{H,J^e}(\mathbf{x}, \mathbf{x}_B, \omega)$

**Table 2.5:** Choice of wavefield and source parameters for the electromagnetic states  $\mathcal{A}$  and  $\mathcal{B}$  to be used in the two-way wavefield electromagnetic reciprocity theorems. The superscripts in the Green's function notation represent the receiver quantity (electric  $E$  or magnetic  $H$  field vector) and source quantity (electric  $J^e$  or magnetic  $J^m$  current), respectively, while the subscripts represent the components of the observed quantity ( $k$ ,  $i$ ) and the source components ( $p$ ,  $q$ ), respectively.  $\zeta_{ij}$  is the inverse of the magnetic permeability  $\zeta_{ip}\mu_{pj} = \delta_{ij}$ .

2.63, then the result is

$$2\Re \left\{ \hat{G}_{p,q}^{E,J^e}(\mathbf{x}_A, \mathbf{x}_B, \omega) \right\} = \int_{\partial\mathbb{D}} n_m \epsilon_{mrj} \left\{ \left( \hat{G}_{p,j}^{E,J^m}(\mathbf{x}_A, \mathbf{x}, \omega) \right)^* \hat{G}_{q,r}^{E,J^e}(\mathbf{x}_B, \mathbf{x}, \omega) + \left( \hat{G}_{p,r}^{E,J^e}(\mathbf{x}_A, \mathbf{x}, \omega) \right)^* \hat{G}_{q,j}^{E,J^m}(\mathbf{x}_B, \mathbf{x}, \omega) \right\} d^2\mathbf{x}. \quad (2.65)$$

The above equation shows, that to retrieve the electric field at point  $\mathbf{x}_A$  due to an electric current source at point  $\mathbf{x}_B$ , one needs to sum the crosscorrelations of observed electric field at  $\mathbf{x}_A$  and  $\mathbf{x}_B$  due to impulsive sources of electric and magnetic currents at points  $\mathbf{x}$  along  $\partial\mathbb{D}$ . Equation 2.65 is exact and valid for any inhomogeneous (inside, as well as outside  $\partial\mathbb{D}$ ) lossless medium. Just like in the acoustic and the elastic case, some simplifications of equation 2.65 are needed to make it easy for practical applications. The first simplification stems from the desire to measure at  $\mathbf{x}_A$  and  $\mathbf{x}_B$  only the response from one source type. To achieve this, using Table 2.5, the right-hand side of equation 2.64 is rewritten only in terms of observed electrical fields, while

Parameter	State $\mathcal{A}$	State $\mathcal{B}$
$\hat{J}_k^e(\mathbf{x}, \omega)$	$\delta(\mathbf{x} - \mathbf{x}_A) \delta_{kp}$	0
$\hat{J}_j^m(\mathbf{x}, \omega)$	0	$\delta(\mathbf{x} - \mathbf{x}_B) \delta_{jq}$
$\hat{E}_r(\mathbf{x}, \omega)$	$\hat{G}_{r,p}^{E,J^e}(\mathbf{x}, \mathbf{x}_A, \omega)$	$\frac{\xi_{rk}}{j\omega} \epsilon_{kmi} \partial_m \hat{G}_{i,q}^{H,J^m}(\mathbf{x}, \mathbf{x}_B, \omega)$ $\triangleq \hat{G}_{r,q}^{E,J^m}(\mathbf{x}, \mathbf{x}_B, \omega)$
$\hat{H}_i(\mathbf{x}, \omega)$	$-\frac{\xi_{ij}}{j\omega} \epsilon_{jmr} \partial_m \hat{G}_{r,p}^{E,J^e}(\mathbf{x}, \mathbf{x}_A, \omega)$ $\triangleq \hat{G}_{i,p}^{H,J^e}(\mathbf{x}, \mathbf{x}_A, \omega)$	$\hat{G}_{i,q}^{H,J^m}(\mathbf{x}, \mathbf{x}_B, \omega)$

**Table 2.6:** Alternative choice of wavefield and source parameters for the electromagnetic states  $\mathcal{A}$  and  $\mathcal{B}$  to be used in the two-way wavefield electromagnetic convolution-type reciprocity theorem.  $\xi_{rk}$  is the inverse of the electric permittivity  $\xi_{rs}\epsilon_{sk} = \delta_{rk}$ .



the source-receiver reciprocity has been used on the left-hand side:

$$\begin{aligned}
2\Re \left\{ \hat{G}_{p,q}^{E,J^e}(\mathbf{x}_A, \mathbf{x}_B, \omega) \right\} = & \\
& - \oint_{\partial\mathbb{D}} n_m \epsilon_{mrj} \left\{ \left( -\frac{\zeta_{ji}}{j\omega} \epsilon_{inl} \partial_n \hat{G}_{l,p}^{E,J^e}(\mathbf{x}, \mathbf{x}_A, \omega) \right)^* \hat{G}_{r,q}^{E,J^e}(\mathbf{x}, \mathbf{x}_B, \omega) \right. \\
& \left. + \left( \hat{G}_{r,p}^{E,J^e}(\mathbf{x}, \mathbf{x}_A, \omega) \right)^* \frac{-\zeta_{ji}}{j\omega} \epsilon_{inl} \partial_n \hat{G}_{l,q}^{E,J^e}(\mathbf{x}, \mathbf{x}_B, \omega) \right\} d^2\mathbf{x}. \quad (2.66)
\end{aligned}$$

Assuming that the medium in a small region around  $\partial\mathbb{D}$  is homogeneous and isotropic, the inverse of the magnetic permeability can be taken outside the integral (and switching back to magnetic permeability):

$$\begin{aligned}
2\Re \left\{ \hat{G}_{p,q}^{E,J^e}(\mathbf{x}_A, \mathbf{x}_B, \omega) \right\} = & \\
& - \frac{1}{j\omega\mu} \oint_{\partial\mathbb{D}} n_m \epsilon_{mrj} \left\{ \left( \epsilon_{jnl} \partial_n \hat{G}_{l,p}^{E,J^e}(\mathbf{x}, \mathbf{x}_A, \omega) \right)^* \hat{G}_{r,q}^{E,J^e}(\mathbf{x}, \mathbf{x}_B, \omega) \right. \\
& \left. - \left( \hat{G}_{r,p}^{E,J^e}(\mathbf{x}, \mathbf{x}_A, \omega) \right)^* \epsilon_{jnl} \partial_n \hat{G}_{l,q}^{E,J^e}(\mathbf{x}, \mathbf{x}_B, \omega) \right\} d^2\mathbf{x}. \quad (2.67)
\end{aligned}$$

Using the fact that  $\epsilon_{mrj}\epsilon_{jnl} = \delta_{mn}\delta_{rl} - \delta_{ml}\delta_{rn}$ , equation 2.67 becomes

$$\begin{aligned}
2\Re \left\{ \hat{G}_{p,q}^{E,J^e}(\mathbf{x}_A, \mathbf{x}_B, \omega) \right\} = & \\
& - \frac{1}{j\omega\mu} \oint_{\partial\mathbb{D}} \left\{ \left( n_m \partial_m \hat{G}_{r,p}^{E,J^e}(\mathbf{x}, \mathbf{x}_A, \omega) \right)^* \hat{G}_{r,q}^{E,J^e}(\mathbf{x}, \mathbf{x}_B, \omega) \right. \\
& \left. - \left( \hat{G}_{r,p}^{E,J^e}(\mathbf{x}, \mathbf{x}_A, \omega) \right)^* n_m \partial_m \hat{G}_{r,q}^{E,J^e}(\mathbf{x}, \mathbf{x}_B, \omega) \right\} d^2\mathbf{x} \\
& - \frac{1}{j\omega\mu} \oint_{\partial\mathbb{D}} \left\{ n_m \left( \hat{G}_{r,p}^{E,J^e}(\mathbf{x}, \mathbf{x}_A, \omega) \right)^* \partial_r \hat{G}_{m,q}^{E,J^e}(\mathbf{x}, \mathbf{x}_B, \omega) \right. \\
& \left. - n_m \left( \partial_r \hat{G}_{m,p}^{E,J^e}(\mathbf{x}, \mathbf{x}_A, \omega) \right)^* \hat{G}_{r,q}^{E,J^e}(\mathbf{x}, \mathbf{x}_B, \omega) \right\} d^2\mathbf{x}. \quad (2.68)
\end{aligned}$$

Because the electric permittivity is constant in a small region around  $\partial\mathbb{D}$ , the electric field is divergence free, i.e.,  $\partial_r \hat{G}_{r,p(q)}^{E,J^e}(\mathbf{x}, \mathbf{x}_{A(B)}, \omega) = 0$ . This means

that one can write

$$\begin{aligned}
2\Re \left\{ \hat{G}_{p,q}^{E,J^e}(\mathbf{x}_A, \mathbf{x}_B, \omega) \right\} = & \\
& - \frac{1}{j\omega\mu} \oint_{\partial\mathbb{D}} \left\{ \left( n_m \partial_m \hat{G}_{r,p}^{E,J^e}(\mathbf{x}, \mathbf{x}_A, \omega) \right)^* \hat{G}_{r,q}^{E,J^e}(\mathbf{x}, \mathbf{x}_B, \omega) \right. \\
& \left. - \left( \hat{G}_{r,p}^{E,J^e}(\mathbf{x}, \mathbf{x}_A, \omega) \right)^* n_m \partial_m \hat{G}_{r,q}^{E,J^e}(\mathbf{x}, \mathbf{x}_B, \omega) \right\} d^2\mathbf{x} \\
& - \frac{1}{j\omega\mu} \oint_{\partial\mathbb{D}} n_m \partial_r \left\{ \left( \hat{G}_{r,p}^{E,J^e}(\mathbf{x}, \mathbf{x}_A, \omega) \right)^* \hat{G}_{m,q}^{E,J^e}(\mathbf{x}, \mathbf{x}_B, \omega) \right. \\
& \left. - \left( \hat{G}_{m,p}^{E,J^e}(\mathbf{x}, \mathbf{x}_A, \omega) \right)^* \hat{G}_{r,q}^{E,J^e}(\mathbf{x}, \mathbf{x}_B, \omega) \right\} d^2\mathbf{x}. \quad (2.69)
\end{aligned}$$

The second integral on the right-hand side of the above equation has a vanishing contribution. This can be shown by decomposing the partial derivative in its normal and tangential components:

$$\partial_r = n_r (n_j \partial_j) - \epsilon_{mij} n_i \epsilon_{jkl} n_k \partial_l. \quad (2.70)$$

Making use of this relation, the second integral on the right-hand side of equation 2.69 can be written as

$$\begin{aligned}
& \frac{1}{j\omega\mu} \oint_{\partial\mathbb{D}} n_m \partial_r \left\{ \left( \hat{G}_{r,p}^{E,J^e}(\mathbf{x}, \mathbf{x}_A, \omega) \right)^* \hat{G}_{m,q}^{E,J^e}(\mathbf{x}, \mathbf{x}_B, \omega) \right. \\
& \left. - \left( \hat{G}_{m,p}^{E,J^e}(\mathbf{x}, \mathbf{x}_A, \omega) \right)^* \hat{G}_{r,q}^{E,J^e}(\mathbf{x}, \mathbf{x}_B, \omega) \right\} d^2\mathbf{x} = \\
& \frac{1}{j\omega\mu} \oint_{\partial\mathbb{D}} n_m n_r (n_j \partial_j) \left\{ \left( \hat{G}_{r,p}^{E,J^e}(\mathbf{x}, \mathbf{x}_A, \omega) \right)^* \hat{G}_{m,q}^{E,J^e}(\mathbf{x}, \mathbf{x}_B, \omega) \right. \\
& \left. - \left( \hat{G}_{m,p}^{E,J^e}(\mathbf{x}, \mathbf{x}_A, \omega) \right)^* \hat{G}_{r,q}^{E,J^e}(\mathbf{x}, \mathbf{x}_B, \omega) \right\} d^2\mathbf{x} \\
& - \frac{1}{j\omega\mu} \oint_{\partial\mathbb{D}} n_m \epsilon_{mij} n_i \epsilon_{jkl} n_k \partial_l \left\{ \left( \hat{G}_{r,p}^{E,J^e}(\mathbf{x}, \mathbf{x}_A, \omega) \right)^* \hat{G}_{m,q}^{E,J^e}(\mathbf{x}, \mathbf{x}_B, \omega) \right. \\
& \left. - \left( \hat{G}_{m,p}^{E,J^e}(\mathbf{x}, \mathbf{x}_A, \omega) \right)^* \hat{G}_{r,q}^{E,J^e}(\mathbf{x}, \mathbf{x}_B, \omega) \right\} d^2\mathbf{x}. \quad (2.71)
\end{aligned}$$

The first integral on the right-hand side of equation 2.71 is zero, which can be verified by directly expanding the notation after substituting the subscripts  $m = 1, 2, 3$  and  $r = 1, 2, 3$ . To analyze the second integral, the boundary  $\partial\mathbb{D}$

is split into two parts  $\partial\mathbb{D}_1$  and  $\partial\mathbb{D}_2$ , which share a common bounding curve  $\mathcal{L}$ ; the unit tangent vectors  $\tau$  and  $-\tau$  of  $\mathcal{L}$  point in opposite directions. Then,

$$\begin{aligned}
& \frac{1}{j\omega\mu} \oint_{\partial\mathbb{D}} n_m \partial_r \left\{ \left( \hat{G}_{r,p}^{E,J^e}(\mathbf{x}, \mathbf{x}_A, \omega) \right)^* \hat{G}_{m,q}^{E,J^e}(\mathbf{x}, \mathbf{x}_B, \omega) \right. \\
& \quad \left. - \left( \hat{G}_{m,p}^{E,J^e}(\mathbf{x}, \mathbf{x}_A, \omega) \right)^* \hat{G}_{r,q}^{E,J^e}(\mathbf{x}, \mathbf{x}_B, \omega) \right\} d^2\mathbf{x} = \\
& - \frac{1}{j\omega\mu} \int_{\partial\mathbb{D}_1} n_m \epsilon_{rij} n_i \epsilon_{jkl} n_k \partial_l \left\{ \left( \hat{G}_{r,p}^{E,J^e}(\mathbf{x}, \mathbf{x}_A, \omega) \right)^* \hat{G}_{m,q}^{E,J^e}(\mathbf{x}, \mathbf{x}_B, \omega) \right. \\
& \quad \left. - \left( \hat{G}_{m,p}^{E,J^e}(\mathbf{x}, \mathbf{x}_A, \omega) \right)^* \hat{G}_{r,q}^{E,J^e}(\mathbf{x}, \mathbf{x}_B, \omega) \right\} d^2\mathbf{x} \\
& - \frac{1}{j\omega\mu} \int_{\partial\mathbb{D}_2} n_m \epsilon_{rij} n_i \epsilon_{jkl} n_k \partial_l \left\{ \left( \hat{G}_{r,p}^{E,J^e}(\mathbf{x}, \mathbf{x}_A, \omega) \right)^* \hat{G}_{m,q}^{E,J^e}(\mathbf{x}, \mathbf{x}_B, \omega) \right. \\
& \quad \left. - \left( \hat{G}_{m,p}^{E,J^e}(\mathbf{x}, \mathbf{x}_A, \omega) \right)^* \hat{G}_{r,q}^{E,J^e}(\mathbf{x}, \mathbf{x}_B, \omega) \right\} d^2\mathbf{x}. \quad (2.72)
\end{aligned}$$

Application of Stoke's curl theorem to the right-hand side of the above equation produces

$$\begin{aligned}
& \frac{1}{j\omega\mu} \oint_{\partial\mathbb{D}} n_m \partial_r \left\{ \left( \hat{G}_{r,p}^{E,J^e}(\mathbf{x}, \mathbf{x}_A, \omega) \right)^* \hat{G}_{m,q}^{E,J^e}(\mathbf{x}, \mathbf{x}_B, \omega) \right. \\
& \quad \left. - \left( \hat{G}_{m,p}^{E,J^e}(\mathbf{x}, \mathbf{x}_A, \omega) \right)^* \hat{G}_{r,q}^{E,J^e}(\mathbf{x}, \mathbf{x}_B, \omega) \right\} d^2\mathbf{x} = \\
& - n_m \frac{1}{j\omega\mu} \oint_{\mathcal{L}} \epsilon_{mij} n_i \tau_j \left\{ \left( \hat{G}_{r,p}^{E,J^e}(\mathbf{x}, \mathbf{x}_A, \omega) \right)^* \hat{G}_{m,q}^{E,J^e}(\mathbf{x}, \mathbf{x}_B, \omega) \right. \\
& \quad \left. - \left( \hat{G}_{m,p}^{E,J^e}(\mathbf{x}, \mathbf{x}_A, \omega) \right)^* \hat{G}_{r,q}^{E,J^e}(\mathbf{x}, \mathbf{x}_B, \omega) \right\} d\mathbf{x} \\
& + \frac{1}{j\omega\mu} \oint_{\mathcal{L}} n_m \epsilon_{mij} n_i \tau_j \left\{ \left( \hat{G}_{r,p}^{E,J^e}(\mathbf{x}, \mathbf{x}_A, \omega) \right)^* \hat{G}_{m,q}^{E,J^e}(\mathbf{x}, \mathbf{x}_B, \omega) \right. \\
& \quad \left. - \left( \hat{G}_{m,p}^{E,J^e}(\mathbf{x}, \mathbf{x}_A, \omega) \right)^* \hat{G}_{r,q}^{E,J^e}(\mathbf{x}, \mathbf{x}_B, \omega) \right\} d\mathbf{x}, \quad (2.73)
\end{aligned}$$

which equals zero because the unit normal vector points in the same direction

for each of the line integrals. In this way, equation 2.69 finally becomes

$$2\Re \left\{ \hat{G}_{p,q}^{E,J^e}(\mathbf{x}_A, \mathbf{x}_B, \omega) \right\} = -\frac{1}{j\omega\mu} \oint_{\partial\mathbb{D}} \left\{ \left( n_m \partial_m \hat{G}_{p,r}^{E,J^e}(\mathbf{x}_A, \mathbf{x}, \omega) \right)^* \hat{G}_{q,r}^{E,J^e}(\mathbf{x}_B, \mathbf{x}, \omega) - \left( \hat{G}_{p,r}^{E,J^e}(\mathbf{x}_A, \mathbf{x}, \omega) \right)^* n_m \partial_m \hat{G}_{q,r}^{E,J^e}(\mathbf{x}_B, \mathbf{x}, \omega) \right\} d^2\mathbf{x}, \quad (2.74)$$

where the reciprocity relation 2.62 was used.

Following a similar analysis path as the one for equations 2.42 till 2.51, i.e., taking the medium outside  $\partial\mathbb{D}$  to be homogeneous and isotropic, making a high-frequency approximation, and assuming  $\partial\mathbb{D}$  to be a sphere with sufficiently large radius, one can finally write

$$2\Re \left\{ \hat{G}_{p,q}^{E,J^e}(\mathbf{x}_A, \mathbf{x}_B, \omega) \right\} \approx -\frac{2}{c\mu} \oint_{\partial\mathbb{D}} \left( \hat{G}_{p,r}^{E,J^e}(\mathbf{x}_A, \mathbf{x}, \omega) \right)^* \hat{G}_{q,r}^{E,J^e}(\mathbf{x}_B, \mathbf{x}, \omega) d^2\mathbf{x}, \quad (2.75)$$

where  $c = \left( \frac{1}{\varepsilon\mu} \right)^{\frac{1}{2}}$  is the propagation velocity outside  $\partial\mathbb{D}$ . The approximation in the above equation refers only to amplitude errors, but when  $\partial\mathbb{D}$  differs significantly from a sphere these errors might be significant. Nevertheless, the application of relation 2.75 will retrieve correctly the phases of all arrivals. That is why relation 2.75 is considered acceptable for EMI for practical applications.

### ■ 2.1.11 EMI relations for transient sources

In the previous subsection, the sources along the boundary  $\partial\mathbb{D}$  were assumed impulsive. In practice, the sources will rather be band-limited. Consider electric current sources characterized by a wavelet with a spectrum  $\hat{s}^j(\mathbf{x}, \omega)$  for  $j = 1, 2, 3$ . In this case, at the points  $\mathbf{x}_A$  and  $\mathbf{x}_B$  the observed electric fields for both states would be

$$\hat{E}_{p(q),j}^{obs}(\mathbf{x}_{A(B)}, \mathbf{x}, \omega) = \hat{G}_{p(q),j}^{E,J^e}(\mathbf{x}_{A(B)}, \mathbf{x}, \omega) \hat{s}^j(\mathbf{x}, \omega). \quad (2.76)$$

Substituting equation 2.76 into the EMI relation 2.75 results in

$$2\Re \left\{ \hat{G}_{p,q}^{E,J^e}(\mathbf{x}_A, \mathbf{x}_B, \omega) \right\} \hat{S}_0(\omega) \approx - \frac{2}{c\mu} \oint_{\partial\mathbb{D}} \hat{F}^j(\mathbf{x}, \omega) \left( \hat{E}_{p,j}^{obs}(\mathbf{x}_A, \mathbf{x}, \omega) \right)^* \hat{E}_{q,j}^{obs}(\mathbf{x}_B, \mathbf{x}, \omega) d^2\mathbf{x}. \quad (2.77)$$

In the above equation,

$$\hat{F}^j(\mathbf{x}, \omega) = \frac{\hat{S}_0(\omega)}{\hat{S}^j(\mathbf{x}, \omega)} \quad (2.78)$$

is a shaping filter with  $\hat{S}^j(\mathbf{x}, \omega)$  the power spectrum of the electric current sources along  $\partial\mathbb{D}$  and  $\hat{S}_0(\omega)$  an average, arbitrary chosen power spectrum. The EMI relation 2.77 can be applied in practice if separate recordings can be made from each of the transient sources on  $\partial\mathbb{D}$ . The shaping filter  $\hat{F}^j(\mathbf{x}, \omega)$  compensates for the known different power spectra of the sources.

### ■ 2.1.12 EMI relations for noise sources

It is not always possible to have separate recordings from the electrical current sources along  $\partial\mathbb{D}$ . To overcome this problem, alternatively one can assume the sources to be mutually uncorrelated with an equal power spectrum  $\hat{S}(\omega)$ . For simultaneously acting sources, at the observation points  $\mathbf{x}_A$  and  $\mathbf{x}_B$  the recorded electric fields will be

$$\hat{E}_p^{obs}(\mathbf{x}_A, \omega) = \oint_{\partial\mathbb{D}} \hat{G}_{p,i}^{E,J^e}(\mathbf{x}_A, \mathbf{x}, \omega) \hat{N}_i(\mathbf{x}, \omega) d^2\mathbf{x} \quad (2.79a)$$

$$\hat{E}_q^{obs}(\mathbf{x}_B, \omega) = \oint_{\partial\mathbb{D}} \hat{G}_{q,j}^{E,J^e}(\mathbf{x}_B, \mathbf{x}', \omega) \hat{N}_j(\mathbf{x}', \omega) d^2\mathbf{x}', \quad (2.79b)$$

where  $\hat{N}_i(\mathbf{x}, \omega)$  and  $\hat{N}_j(\mathbf{x}', \omega)$  represent the spectra of the electric source at  $\mathbf{x}$  and  $\mathbf{x}'$ , respectively. Because the sources are assumed uncorrelated for any  $i \neq j$  and  $\mathbf{x} \neq \mathbf{x}'$ , it follows that

$$\langle \hat{N}_i^*(\mathbf{x}, \omega) \hat{N}_j(\mathbf{x}', \omega) \rangle = \frac{2}{c\mu} \delta_{ij} \delta(\mathbf{x} - \mathbf{x}') \hat{S}(\omega). \quad (2.80)$$

Using the above property, the correlation of the observed electric fields at  $\mathbf{x}_A$  and  $\mathbf{x}_B$  is

$$\langle \hat{E}_p^{obs*}(\mathbf{x}_A, \omega) \hat{E}_q^{obs}(\mathbf{x}_B, \omega) \rangle = \oint_{\partial\mathbb{D}} \frac{2}{c\mu} \left( \hat{G}_{p,j}^{E,J^e}(\mathbf{x}_A, \mathbf{x}, \omega) \right)^* \hat{G}_{q,j}^{E,J^e}(\mathbf{x}_B, \mathbf{x}, \omega) \hat{S}(\omega) d^2\mathbf{x}. \quad (2.81)$$

Comparing equation 2.81 to equation 2.75, it can be written that

$$2\Re \left\{ \hat{G}_{p,q}^{E,J^e}(\mathbf{x}_A, \mathbf{x}_B, \omega) \right\} \hat{S}(\omega) \approx -\langle \hat{E}_p^{obs*}(\mathbf{x}_A, \omega) \hat{E}_q^{obs}(\mathbf{x}_B, \omega) \rangle, \quad (2.82)$$

which means that the crosscorrelation of the observed electromagnetic noise at two points will retrieve the electromagnetic Green's function between these two points convolved with the power spectrum of the noise.

## 2.2 SI relations based on a one-way wavefield reciprocity

### ■ 2.2.1 Reciprocity theorems

Consider a 3D inhomogeneous, lossless medium. In this medium, one chooses a domain  $\mathbb{D}$  with mass density  $\rho(\mathbf{x})$  and compressibility  $\kappa(\mathbf{x})$ , if the medium is acoustic, or with compliance  $s_{ijkl}(\mathbf{x})$  in case of an elastic medium; domain  $\mathbb{D}$  contains no discontinuities in the medium parameters. This domain is bounded by  $\partial\mathbb{D}$  with an outward-pointing normal vector  $\mathbf{n}$ . The boundary consists of two parallel planes, which stretch to infinity and are horizontal. The top plane is  $\partial\mathbb{D}_0$  and the bottom one is  $\partial\mathbb{D}_m$ . The  $x_3$  axis points downwards.

Choosing the preferred direction of propagation to be the vertical direction (along the  $x_3$  axis), the one-way wavefield equation can be written in the space-frequency domain in matrix-vector form as

$$\partial_3 \hat{\mathbf{P}}(\mathbf{x}, \omega) - \hat{\mathbf{B}}(\mathbf{x}, \omega) \hat{\mathbf{P}}(\mathbf{x}, \omega) = \hat{\mathbf{S}}(\mathbf{x}, \omega). \quad (2.83)$$

In the above equation,  $\hat{\mathbf{P}}(\mathbf{x}, \omega)$  represents the flux-normalized one-way wave quantities and  $\hat{\mathbf{S}}(\mathbf{x}, \omega)$  represents the flux-normalized one-way source quantities. Table 2.7 shows the expansion of these quantities in case of an acoustic

Parameter	Acoustic medium	Elastic medium
$\hat{\mathbf{P}}(\mathbf{x}, \omega)$	$\begin{pmatrix} \hat{P}^+(\mathbf{x}, \omega) \\ \hat{P}^-(\mathbf{x}, \omega) \end{pmatrix}$	$\begin{pmatrix} \hat{\Phi}^+(\mathbf{x}, \omega) \\ \hat{\Psi}_{x_1}^+(\mathbf{x}, \omega) \\ \hat{\Psi}_{x_2}^+(\mathbf{x}, \omega) \\ \hat{\Phi}^-(\mathbf{x}, \omega) \\ \hat{\Psi}_{x_1}^-(\mathbf{x}, \omega) \\ \hat{\Psi}_{x_2}^-(\mathbf{x}, \omega) \end{pmatrix}$
$\hat{\mathbf{S}}(\mathbf{x}, \omega)$	$\begin{pmatrix} \hat{S}^+(\mathbf{x}, \omega) \\ \hat{S}^-(\mathbf{x}, \omega) \end{pmatrix}$	$\begin{pmatrix} \hat{S}_{\Phi}^+(\mathbf{x}, \omega) \\ \hat{S}_{\Psi_{x_1}}^+(\mathbf{x}, \omega) \\ \hat{S}_{\Psi_{x_2}}^+(\mathbf{x}, \omega) \\ \hat{S}_{\Phi}^-(\mathbf{x}, \omega) \\ \hat{S}_{\Psi_{x_1}}^-(\mathbf{x}, \omega) \\ \hat{S}_{\Psi_{x_2}}^-(\mathbf{x}, \omega) \end{pmatrix}$

**Table 2.7:** Expansion of the variables in equation 2.83 in case of an acoustic and an elastic medium. The superscripts + and – denote downgoing and upgoing propagation, respectively,  $\hat{P}^{\pm}$  stands for one-way wavefield,  $\hat{S}^{\pm}$  - for one-way source field,  $\hat{\Phi}$  is the P-wave potential,  $\hat{\Psi}_{x_1}$  and  $\hat{\Psi}_{x_2}$  are the S-wave potentials with polarizations in the  $x_2x_3$ - and  $x_1x_3$ -plane, respectively,  $\hat{S}_{\Phi}$  is the source P-wave potential, and  $\hat{S}_{\Psi_{x_1}}$  and  $\hat{S}_{\Psi_{x_2}}$  are the source S-wave potentials with  $x_2x_3$ - and  $x_1x_3$ -polarization, respectively.

and an elastic medium.  $\hat{\mathbf{B}}(\mathbf{x}, \omega)$  is a one-way pseudo-differential operator matrix defined as

$$\hat{\mathbf{B}}(\mathbf{x}, \omega) = -j\omega\hat{\mathbf{\Lambda}}(\mathbf{x}, \omega) + \hat{\mathbf{\Theta}}(\mathbf{x}, \omega), \quad (2.84)$$

where the first term  $-j\omega\hat{\mathbf{\Lambda}}(\mathbf{x}, \omega)$  accounts for the vertical propagation of the one-way wavefield, while the operator matrix

$$\hat{\mathbf{\Theta}}(\mathbf{x}, \omega) = -\hat{\mathbf{L}}^{-1}(\mathbf{x}, \omega) \partial_3 \hat{\mathbf{L}}(\mathbf{x}, \omega) \quad (2.85)$$

accounts for the vertical scattering of the one-way wavefield due to variations of the medium parameters in the vertical direction [Corones et al., 1983; Fishman et al., 1987; Wapenaar and Berkhout, 1989; de Hoop, 1992; Wapenaar and Grimbergen, 1996; Haines and de Hoop, 1996]. In equation 2.85,  $\hat{\mathbf{L}}(\mathbf{x}, \omega)$  is a composition operator turning the one-way wavefields into two-way wavefields and  $\hat{\mathbf{L}}^{-1}(\mathbf{x}, \omega)$  is a decomposition operator turning the two-way wavefields into one-way wavefields.

Two independent states  $\mathcal{A}$  and  $\mathcal{B}$  are taken in the domain  $\mathbb{D}$ . State  $\mathcal{A}$  is described in the space-frequency domain by the one-way wavefield quantity  $\hat{\mathbf{P}}_{\mathcal{A}}(\mathbf{x}, \omega)$ , by the one-way source quantity  $\hat{\mathbf{S}}_{\mathcal{A}}(\mathbf{x}, \omega)$ , and by the operator matrix  $\hat{\mathbf{B}}_{\mathcal{A}}(\mathbf{x}, \omega)$ . State  $\mathcal{B}$  is characterized by the same variables, but the corresponding subscripts  $\mathcal{A}$  are substituted by the subscript  $\mathcal{B}$ .

The one-way interaction quantity describing the local convolution of the wavefields in the two states, which is the counterpart of the two-way acoustic interaction quantity 2.2, is

$$\begin{aligned} \partial_3 \left\{ \hat{\mathbf{P}}_{\mathcal{A}}^T(\mathbf{x}, \omega) \mathbf{N} \hat{\mathbf{P}}_{\mathcal{B}}(\mathbf{x}, \omega) \right\} &= \left\{ \partial_3 \hat{\mathbf{P}}_{\mathcal{A}}^T(\mathbf{x}, \omega) \right\} \mathbf{N} \hat{\mathbf{P}}_{\mathcal{B}}(\mathbf{x}, \omega) \\ &+ \hat{\mathbf{P}}_{\mathcal{A}}^T(\mathbf{x}, \omega) \mathbf{N} \left\{ \partial_3 \hat{\mathbf{P}}_{\mathcal{B}}(\mathbf{x}, \omega) \right\}, \end{aligned} \quad (2.86)$$

where  $\mathbf{N} = \text{antidiag}(1, -1)$ .

Substitution of the one-way wave equation 2.83 for the states  $\mathcal{A}$  and  $\mathcal{B}$  in equation 2.86 results in

$$\begin{aligned} \partial_3 \left\{ \hat{\mathbf{P}}_{\mathcal{A}}^T(\mathbf{x}, \omega) \mathbf{N} \hat{\mathbf{P}}_{\mathcal{B}}(\mathbf{x}, \omega) \right\} &= \\ \left( \hat{\mathbf{B}}_{\mathcal{A}}(\mathbf{x}, \omega) \hat{\mathbf{P}}_{\mathcal{A}}(\mathbf{x}, \omega) \right)^T \mathbf{N} \hat{\mathbf{P}}_{\mathcal{B}}(\mathbf{x}, \omega) &+ \hat{\mathbf{P}}_{\mathcal{A}}^T(\mathbf{x}, \omega) \mathbf{N} \hat{\mathbf{B}}_{\mathcal{B}}(\mathbf{x}, \omega) \hat{\mathbf{P}}_{\mathcal{B}}(\mathbf{x}, \omega) \\ + \hat{\mathbf{P}}_{\mathcal{A}}^T(\mathbf{x}, \omega) \mathbf{N} \hat{\mathbf{S}}_{\mathcal{B}}(\mathbf{x}, \omega) &+ \hat{\mathbf{S}}_{\mathcal{A}}^T(\mathbf{x}, \omega) \mathbf{N} \hat{\mathbf{P}}_{\mathcal{B}}(\mathbf{x}, \omega). \end{aligned} \quad (2.87)$$



Equation 2.87 represents the local form of the one-way wavefield convolution-type reciprocity theorem [Wapenaar and Grimbergen, 1996].

Integration of equation 2.87 over the domain  $\mathbb{D}$  and application of Gauss' divergence theorem to the left-hand side of equation 2.87 gives

$$\begin{aligned} \int_{\mathbb{D}} \left\{ \hat{\mathbf{P}}_{\mathcal{A}}^T(\mathbf{x}, \omega) \hat{\mathbf{B}}_{\mathcal{A}}^T(\mathbf{x}, \omega) \mathbf{N} \hat{\mathbf{P}}_{\mathcal{B}}(\mathbf{x}, \omega) + \hat{\mathbf{P}}_{\mathcal{A}}^T(\mathbf{x}, \omega) \mathbf{N} \hat{\mathbf{B}}_{\mathcal{B}}(\mathbf{x}, \omega) \hat{\mathbf{P}}_{\mathcal{B}}(\mathbf{x}, \omega) \right. \\ \left. + \hat{\mathbf{P}}_{\mathcal{A}}^T(\mathbf{x}, \omega) \mathbf{N} \hat{\mathbf{S}}_{\mathcal{B}}(\mathbf{x}, \omega) + \hat{\mathbf{S}}_{\mathcal{A}}^T(\mathbf{x}, \omega) \mathbf{N} \hat{\mathbf{P}}_{\mathcal{B}}(\mathbf{x}, \omega) \right\} d^3 \mathbf{x} = \\ \oint_{\partial \mathbb{D}} \left\{ \hat{\mathbf{P}}_{\mathcal{A}}^T(\mathbf{x}, \omega) \mathbf{N} \hat{\mathbf{P}}_{\mathcal{B}}(\mathbf{x}, \omega) \right\} n_3 d^2 \mathbf{x}. \quad (2.88) \end{aligned}$$

Equation 2.88 represents the global form of the one-way wavefield convolution-type reciprocity theorem.

Making use of the symmetry property

$$\hat{\mathbf{B}}_{\mathcal{A}}^T(\mathbf{x}, \omega) \mathbf{N} = -\mathbf{N} \hat{\mathbf{B}}_{\mathcal{A}}(\mathbf{x}, \omega) \quad (2.89)$$

and assuming the medium parameters in both states to be the same, which means that the one-way pseudo-differential operator matrices for the two states are equal  $\hat{\mathbf{B}}_{\mathcal{A}}(\mathbf{x}, \omega) = \hat{\mathbf{B}}_{\mathcal{B}}(\mathbf{x}, \omega)$ , then the first two terms in the left-hand side of equation 2.88 cancel and the convolution-type reciprocity relation simplifies to

$$\begin{aligned} \int_{\mathbb{D}} \left\{ \hat{\mathbf{P}}_{\mathcal{A}}^T(\mathbf{x}, \omega) \mathbf{N} \hat{\mathbf{S}}_{\mathcal{B}}(\mathbf{x}, \omega) + \hat{\mathbf{S}}_{\mathcal{A}}^T(\mathbf{x}, \omega) \mathbf{N} \hat{\mathbf{P}}_{\mathcal{B}}(\mathbf{x}, \omega) \right\} d^3 \mathbf{x} = \\ \oint_{\partial \mathbb{D}} \left\{ \hat{\mathbf{P}}_{\mathcal{A}}^T(\mathbf{x}, \omega) \mathbf{N} \hat{\mathbf{P}}_{\mathcal{B}}(\mathbf{x}, \omega) \right\} n_3 d^2 \mathbf{x}. \quad (2.90) \end{aligned}$$

Instead of equation 2.86, as a starting point can be taken the interaction quantity describing the local correlation of the wavefields in the two state:

$$\begin{aligned} \partial_3 \left\{ \hat{\mathbf{P}}_{\mathcal{A}}^\dagger(\mathbf{x}, \omega) \mathbf{J} \hat{\mathbf{P}}_{\mathcal{B}}(\mathbf{x}, \omega) \right\} = \left\{ \partial_3 \hat{\mathbf{P}}_{\mathcal{A}}^\dagger(\mathbf{x}, \omega) \right\} \mathbf{J} \hat{\mathbf{P}}_{\mathcal{B}}(\mathbf{x}, \omega) \\ + \hat{\mathbf{P}}_{\mathcal{A}}^\dagger(\mathbf{x}, \omega) \mathbf{J} \left\{ \partial_3 \hat{\mathbf{P}}_{\mathcal{B}}(\mathbf{x}, \omega) \right\}, \quad (2.91) \end{aligned}$$

where  $\mathbf{J} = \text{diag}(1, -1)$ . In such a case, the substitution of the one-way

wave equation 2.83 for the states  $\mathcal{A}$  and  $\mathcal{B}$  in equation 2.91 results in

$$\begin{aligned} \partial_3 \left\{ \hat{\mathbf{P}}_{\mathcal{A}}^\dagger(\mathbf{x}, \omega) \mathbf{J} \hat{\mathbf{P}}_{\mathcal{B}}(\mathbf{x}, \omega) \right\} = \\ \hat{\mathbf{P}}_{\mathcal{A}}^\dagger(\mathbf{x}, \omega) \mathbf{J} \hat{\mathbf{B}}_{\mathcal{B}}(\mathbf{x}, \omega) \hat{\mathbf{P}}_{\mathcal{B}}(\mathbf{x}, \omega) + \left( \hat{\mathbf{B}}_{\mathcal{A}}(\mathbf{x}, \omega) \hat{\mathbf{P}}_{\mathcal{A}}(\mathbf{x}, \omega) \right)^\dagger \mathbf{J} \hat{\mathbf{P}}_{\mathcal{B}}(\mathbf{x}, \omega) \\ + \hat{\mathbf{P}}_{\mathcal{A}}^\dagger(\mathbf{x}, \omega) \mathbf{J} \hat{\mathbf{S}}_{\mathcal{B}}(\mathbf{x}, \omega) + \hat{\mathbf{S}}_{\mathcal{A}}^\dagger(\mathbf{x}, \omega) \mathbf{J} \hat{\mathbf{P}}_{\mathcal{B}}(\mathbf{x}, \omega). \end{aligned} \quad (2.92)$$

The above equation represents the local form of the one-way wavefield correlation-type reciprocity theorem [Wapenaar and Grimbergen, 1996].

Integration of equation 2.92 over the domain  $\mathbb{D}$  and application of Gauss' divergence theorem to the left-hand side of this equation gives

$$\begin{aligned} \int_{\mathbb{D}} \left\{ \hat{\mathbf{P}}_{\mathcal{A}}^\dagger(\mathbf{x}, \omega) \mathbf{J} \hat{\mathbf{B}}_{\mathcal{B}}(\mathbf{x}, \omega) \hat{\mathbf{P}}_{\mathcal{B}}(\mathbf{x}, \omega) + \hat{\mathbf{P}}_{\mathcal{A}}^\dagger(\mathbf{x}, \omega) \hat{\mathbf{B}}_{\mathcal{A}}^\dagger(\mathbf{x}, \omega) \mathbf{J} \hat{\mathbf{P}}_{\mathcal{B}}(\mathbf{x}, \omega) \right. \\ \left. + \hat{\mathbf{P}}_{\mathcal{A}}^\dagger(\mathbf{x}, \omega) \mathbf{J} \hat{\mathbf{S}}_{\mathcal{B}}(\mathbf{x}, \omega) + \hat{\mathbf{S}}_{\mathcal{A}}^\dagger(\mathbf{x}, \omega) \mathbf{J} \hat{\mathbf{P}}_{\mathcal{B}}(\mathbf{x}, \omega) \right\} d^3 \mathbf{x} = \\ \oint_{\partial \mathbb{D}} \left\{ \hat{\mathbf{P}}_{\mathcal{A}}^\dagger(\mathbf{x}, \omega) \mathbf{J} \hat{\mathbf{P}}_{\mathcal{B}}(\mathbf{x}, \omega) \right\} n_3 d^2 \mathbf{x}. \end{aligned} \quad (2.93)$$

Equation 2.93 represents the global form of the one-way wavefield correlation-type reciprocity theorem.

The one-way pseudo-differential operator matrix obeys the following symmetry property [Wapenaar and Grimbergen, 1996]:

$$\hat{\mathbf{B}}_{\mathcal{A}}^\dagger(\mathbf{x}, \omega) \mathbf{J} \approx -\mathbf{J} \hat{\mathbf{B}}_{\mathcal{A}}(\mathbf{x}, \omega), \quad (2.94)$$

where the approximation sign is used as the evanescent waves have been neglected. When the medium parameters in both states are the same  $\hat{\mathbf{B}}_{\mathcal{A}}(\mathbf{x}, \omega) = \hat{\mathbf{B}}_{\mathcal{B}}(\mathbf{x}, \omega)$  and neglecting the evanescent fields, then the first two terms in the left-hand side of equation 2.93 cancel and

$$\begin{aligned} \int_{\mathbb{D}} \left\{ \hat{\mathbf{P}}_{\mathcal{A}}^\dagger(\mathbf{x}, \omega) \mathbf{J} \hat{\mathbf{S}}_{\mathcal{B}}(\mathbf{x}, \omega) + \hat{\mathbf{S}}_{\mathcal{A}}^\dagger(\mathbf{x}, \omega) \mathbf{J} \hat{\mathbf{P}}_{\mathcal{B}}(\mathbf{x}, \omega) \right\} d^3 \mathbf{x} = \\ \oint_{\partial \mathbb{D}} \left\{ \hat{\mathbf{P}}_{\mathcal{A}}^\dagger(\mathbf{x}, \omega) \mathbf{J} \hat{\mathbf{P}}_{\mathcal{B}}(\mathbf{x}, \omega) \right\} n_3 d^2 \mathbf{x}. \end{aligned} \quad (2.95)$$

Let the top boundary  $\partial \mathbb{D}_0$  lie at  $x_{3,0} + \epsilon$  and  $\partial \mathbb{D}_m$  at level  $x_{3,m} - \epsilon$ , where  $\epsilon$  is chosen infinitesimally small. Just above  $\partial \mathbb{D}_0$  there is a free surface at  $x_{3,0}$

and the half-space below  $\partial\mathbb{D}_m$  is taken to be homogeneous. The domain  $\mathbb{D}$  is taken to be source-free, i.e.  $\hat{\mathbf{S}}_{\mathcal{A}} = \hat{\mathbf{S}}_{\mathcal{B}} = 0$ . At  $\partial\mathbb{D}_0$ ,  $n_3 = -1$ , while at  $\partial\mathbb{D}_m$ ,  $n_3 = +1$ . For these choices, equations 2.90 and 2.95 can be written as

$$\int_{\partial\mathbb{D}_0} \hat{\mathbf{P}}_{\mathcal{A}}^T(\mathbf{x}, \omega) \mathbf{N} \hat{\mathbf{P}}_{\mathcal{B}}(\mathbf{x}, \omega) d^2\mathbf{x} = \int_{\partial\mathbb{D}_m} \hat{\mathbf{P}}_{\mathcal{A}}^T(\mathbf{x}, \omega) \mathbf{N} \hat{\mathbf{P}}_{\mathcal{B}}(\mathbf{x}, \omega) d^2\mathbf{x} \quad (2.96)$$

and

$$\int_{\partial\mathbb{D}_0} \hat{\mathbf{P}}_{\mathcal{A}}^\dagger(\mathbf{x}, \omega) \mathbf{J} \hat{\mathbf{P}}_{\mathcal{B}}(\mathbf{x}, \omega) d^2\mathbf{x} = \int_{\partial\mathbb{D}_m} \hat{\mathbf{P}}_{\mathcal{A}}^\dagger(\mathbf{x}, \omega) \mathbf{J} \hat{\mathbf{P}}_{\mathcal{B}}(\mathbf{x}, \omega) d^2\mathbf{x}, \quad (2.97)$$

respectively.

### ■ 2.2.2 SI relations for impulsive sources in an acoustic medium

The following choices are made for the states  $\mathcal{A}$  and  $\mathcal{B}$ . There are impulsive sources of downgoing waves at points  $\mathbf{x}_{\mathcal{A}} = (\mathbf{x}_{H,A}, x_{3,0})$  and  $\mathbf{x}_{\mathcal{B}} = (\mathbf{x}_{H,B}, x_{3,0})$ , with  $\mathbf{x}_H = (x_1, x_2)$ , for states  $\mathcal{A}$  and  $\mathcal{B}$ , respectively. The half-space below  $\partial\mathbb{D}_m$  is taken source-free. Let the reflection response of the domain, including the internal multiples, to downgoing waves be  $\hat{R}^+$ . Note that in the reflection response the + sign means that downgoing waves have been reflected. Then, the upgoing wavefield at  $\partial\mathbb{D}_0$  would represent the reflection response  $\hat{R}^+(\mathbf{x}, \mathbf{x}_{\mathcal{A}(\mathcal{B})}, \omega)$  of the domain  $\mathbb{D}$ , while the downgoing wavefield would consist of a delta function at the source position plus the back-reflected upgoing wavefield (see Table 2.8). At the bottom boundary  $\partial\mathbb{D}_m$ , the wavefield would consist only of downgoing waves, i.e., it would represent only the transmission  $\hat{T}^+(\mathbf{x}, \mathbf{x}_{\mathcal{A}(\mathcal{B})}, \omega)$  response of the domain to downgoing waves (from where also the + sign).

When the parameters from the middle and the right columns of Table 2.8 are substituted in equation 2.96, the result is

$$\hat{R}^+(\mathbf{x}_{\mathcal{A}}, \mathbf{x}_{\mathcal{B}}, \omega) = \hat{R}^+(\mathbf{x}_{\mathcal{B}}, \mathbf{x}_{\mathcal{A}}, \omega). \quad (2.98)$$

If the choice in state  $\mathcal{A}$  for an impulsive source of downgoing waves placed just above  $\partial\mathbb{D}_0$  is changed to a choice for an impulsive source of upgoing waves placed just below  $\partial\mathbb{D}_m$ , then the wavefields could be described in terms of the domain  $\mathbb{D}$ 's reflection response to upgoing waves  $\hat{R}^-$  and transmission response to upgoing waves  $\hat{T}^-$  as given in Table 2.9. If the middle and the right columns of Table 2.9 are substituted in equation 2.96, then the

Parameter	State $\mathcal{A}$	State $\mathcal{B}$
$\hat{\mathbf{P}}$ at $\partial\mathbb{D}_0$	$\hat{P}^+(\mathbf{x}, \mathbf{x}_A, \omega) = \delta(\mathbf{x}_H - \mathbf{x}_{H,A})$ $+ r^- \hat{R}^+(\mathbf{x}, \mathbf{x}_A, \omega)$ $\hat{P}^-(\mathbf{x}, \mathbf{x}_A, \omega) = \hat{R}^+(\mathbf{x}, \mathbf{x}_A, \omega)$	$\hat{P}^+(\mathbf{x}, \mathbf{x}_B, \omega) = \delta(\mathbf{x}_H - \mathbf{x}_{H,B})$ $+ r^- \hat{R}^+(\mathbf{x}, \mathbf{x}_B, \omega)$ $\hat{P}^-(\mathbf{x}, \mathbf{x}_B, \omega) = \hat{R}^+(\mathbf{x}, \mathbf{x}_B, \omega)$
$\hat{\mathbf{P}}$ at $\partial\mathbb{D}_m$	$\hat{P}^+(\mathbf{x}, \mathbf{x}_A, \omega) = \hat{T}^+(\mathbf{x}, \mathbf{x}_A, \omega)$ $\hat{P}^-(\mathbf{x}, \mathbf{x}_A, \omega) = 0$	$\hat{P}^+(\mathbf{x}, \mathbf{x}_B, \omega) = \hat{T}^+(\mathbf{x}, \mathbf{x}_B, \omega)$ $\hat{P}^-(\mathbf{x}, \mathbf{x}_B, \omega) = 0$

**Table 2.8:** Choice of parameters for the acoustical states  $\mathcal{A}$  and  $\mathcal{B}$  to be used in the one-way wavefield reciprocity theorems, where  $r^- = -1$  is the reflection coefficient of the free surface and  $\mathbf{x}_A$  and  $\mathbf{x}_B$  are just above  $\partial\mathbb{D}_0$ .

Parameter	State $\mathcal{A}$	State $\mathcal{B}$
$\hat{\mathbf{P}}$ at $\partial\mathbb{D}_0$	$\hat{P}^+(\mathbf{x}, \mathbf{x}_A, \omega) = r^- \hat{T}^-(\mathbf{x}, \mathbf{x}_A, \omega)$ $\hat{P}^-(\mathbf{x}, \mathbf{x}_A, \omega) = \hat{T}^-(\mathbf{x}, \mathbf{x}_A, \omega)$	$\hat{P}^+(\mathbf{x}, \mathbf{x}_B, \omega) = \delta(\mathbf{x}_H - \mathbf{x}_{H,B})$ $+ r^- \hat{R}^+(\mathbf{x}, \mathbf{x}_B, \omega)$ $\hat{P}^-(\mathbf{x}, \mathbf{x}_B, \omega) = \hat{R}^+(\mathbf{x}, \mathbf{x}_B, \omega)$
$\hat{\mathbf{P}}$ at $\partial\mathbb{D}_m$	$\hat{P}^+(\mathbf{x}, \mathbf{x}_A, \omega) = \hat{R}^-(\mathbf{x}, \mathbf{x}_A, \omega)$ $\hat{P}^-(\mathbf{x}, \mathbf{x}_A, \omega) = \delta(\mathbf{x}_H - \mathbf{x}_{H,A})$	$\hat{P}^+(\mathbf{x}, \mathbf{x}_B, \omega) = \hat{T}^+(\mathbf{x}, \mathbf{x}_B, \omega)$ $\hat{P}^-(\mathbf{x}, \mathbf{x}_B, \omega) = 0$

**Table 2.9:** Alternative choice of parameters for the acoustical states  $\mathcal{A}$  and  $\mathcal{B}$  to be used in the one-way wavefield convolution-type reciprocity theorem, where  $\mathbf{x}_A$  is just below  $\partial\mathbb{D}_m$  and  $\mathbf{x}_B$  is just above  $\partial\mathbb{D}_0$ .

result is

$$\hat{T}^+(\mathbf{x}_A, \mathbf{x}_B, \omega) = \hat{T}^-(\mathbf{x}_B, \mathbf{x}_A, \omega), \quad (2.99)$$

meaning that the transmission responses of the domain  $\mathbb{D}$  to downgoing and upgoing waves are equal. Note that this is true only because the two-way wavefields were decomposed into flux-normalized one-way wavefields. Note, that in the above reciprocity relation, the source and the receiver are at different depth levels. The above relation is valid only in the case of flux-normalized wavefield decomposition. When the wavefields are decomposed with pressure normalization, the upgoing transmission field is not equal to the downgoing transmission field [Wapenaar and Grimbergen, 1996].

Let now substitute the parameters from the middle and the right columns of Table 2.8 in equation 2.97. The use of the sifting property of the delta function results in

$$\begin{aligned} \left\{ \hat{R}^+(\mathbf{x}_B, \mathbf{x}_A, \omega) \right\}^* + \hat{R}^+(\mathbf{x}_A, \mathbf{x}_B, \omega) &= \delta(\mathbf{x}_{H,B} - \mathbf{x}_{H,A}) \\ &- \int_{\partial\mathbb{D}_m} \left\{ \hat{T}^+(\mathbf{x}, \mathbf{x}_A, \omega) \right\}^* \hat{T}^+(\mathbf{x}, \mathbf{x}_B, \omega) d^2\mathbf{x}. \end{aligned} \quad (2.100)$$

Application of the source-receiver reciprocities 2.98 and 2.99 finally gives the one-way acoustic wavefield SI relation

$$\begin{aligned} 2\Re \left\{ \hat{R}^+(\mathbf{x}_A, \mathbf{x}_B, \omega) \right\} &= \delta(\mathbf{x}_{H,B} - \mathbf{x}_{H,A}) \\ &- \int_{\partial\mathbb{D}_m} \left\{ \hat{T}^-(\mathbf{x}_A, \mathbf{x}, \omega) \right\}^* \hat{T}^-(\mathbf{x}_B, \mathbf{x}, \omega) d^2\mathbf{x}. \end{aligned} \quad (2.101)$$

The above equation shows that the reflection response that one would observe when the receivers and the sources are at the surface, can be retrieved from the correlation of transmission observations at the surface due to subsurface sources. Equation 2.101 was derived under the assumption of a homogeneous half space below the level of the subsurface source. When this is not the case, non-physical artefacts (ghost events) may arise in the retrieved reflection response. These ghost events will be strongly weakened or may even disappear when the subsurface sources are sufficiently random in their vertical distribution. The reason for this, as was explained in section 2.1.2, is in the non-coherent summation of the ghost events from the different correlation products (see also numerical results in Draganov et al. [2004]).

### ■ 2.2.3 SI relation for transient sources in an acoustic medium

When the sources in the subsurface are not impulsive but characterized by a band-limited wavelet  $\hat{s}(\mathbf{x}, \omega)$ , the observed one-way transmission responses at the points  $\mathbf{x}_A$  and  $\mathbf{x}_B$  in the two states are

$$\hat{T}^{obs}(\mathbf{x}_{A(B)}, \mathbf{x}, \omega) = \hat{T}^{-}(\mathbf{x}_{A(B)}, \mathbf{x}, \omega) \hat{s}(\mathbf{x}, \omega). \quad (2.102)$$

Substitution of the above equation for states  $\mathcal{A}$  and  $\mathcal{B}$  into the SI relation 2.101 results in

$$2\Re \left\{ \hat{R}^{+}(\mathbf{x}_A, \mathbf{x}_B, \omega) \right\} \hat{S}_0(\omega) = \delta(\mathbf{x}_{H,B} - \mathbf{x}_{H,A}) \hat{S}_0(\omega) - \int_{\partial\mathbb{D}_m} \hat{F}(\mathbf{x}, \omega) \left\{ \hat{T}^{obs}(\mathbf{x}_A, \mathbf{x}, \omega) \right\}^* \hat{T}^{obs}(\mathbf{x}_B, \mathbf{x}, \omega) d^2\mathbf{x}, \quad (2.103)$$

where  $\hat{S}_0(\omega)$  is an average, arbitrarily chosen power spectrum and

$$\hat{F}(\mathbf{x}, \omega) = \frac{\hat{S}_0(\omega)}{\hat{S}(\mathbf{x}, \omega)}, \quad (2.104)$$

is a shaping filter with  $\hat{S}(\mathbf{x}, \omega) = \hat{s}^*(\mathbf{x}, \omega) \hat{s}(\mathbf{x}, \omega)$  the power spectrum of the sources. The above SI relation can be used when separate recordings can be taken at  $\mathbf{x}_A$  and  $\mathbf{x}_B$  from each of the transient sources on  $\partial\mathbb{D}_m$ . The shaping filter  $\hat{F}(\mathbf{x}, \omega)$  compensates for the different power spectra of the sources.

### ■ 2.2.4 SI relation for noise sources in an acoustic medium

When no separate transmission recordings are available from each of the subsurface sources, one can find an alternative solution by assuming that the sources along  $\partial\mathbb{D}_m$  act simultaneously and are mutually uncorrelated, each with the same individual power spectrum  $\hat{S}(\omega)$ . In that case,

$$\hat{T}^{obs}(\mathbf{x}_A, \omega) = \int_{\partial\mathbb{D}_m} \hat{T}^{-}(\mathbf{x}_A, \mathbf{x}, \omega) \hat{N}(\mathbf{x}, \omega) d^2\mathbf{x}, \quad (2.105a)$$

$$\hat{T}^{obs}(\mathbf{x}_B, \omega) = \int_{\partial\mathbb{D}_m} \hat{T}^{-}(\mathbf{x}_B, \mathbf{x}, \omega) \hat{N}(\mathbf{x}', \omega) d^2\mathbf{x}', \quad (2.105b)$$

with  $\hat{N}(\mathbf{x}, \omega)$  and  $\hat{N}(\mathbf{x}', \omega)$  the spectra of the noise sources at  $\mathbf{x}$  and  $\mathbf{x}'$ , respectively, where

$$\langle \hat{N}^*(\mathbf{x}, \omega) \hat{N}(\mathbf{x}', \omega) \rangle = \delta(\mathbf{x} - \mathbf{x}') \hat{S}(\omega). \quad (2.106)$$

Thus, crosscorrelation of the left-hand sides of equations 2.105 can be written as

$$\begin{aligned} \left\langle \left\{ \hat{T}^{obs}(\mathbf{x}_A, \omega) \right\}^* \hat{T}^{obs}(\mathbf{x}_B, \omega) \right\rangle = \\ \int_{\partial \mathbb{D}_m} \left\{ \hat{T}^-(\mathbf{x}_A, \mathbf{x}, \omega) \right\}^* \hat{T}^-(\mathbf{x}_B, \mathbf{x}, \omega) \hat{S}(\omega) d^2 \mathbf{x}. \end{aligned} \quad (2.107)$$

Comparing the equation above with equation 2.101, it can be concluded that

$$\begin{aligned} 2\Re \left\{ \hat{R}^+(\mathbf{x}_A, \mathbf{x}_B, \omega) \right\} \hat{S}(\omega) = \delta(\mathbf{x}_{H,B} - \mathbf{x}_{H,A}) \hat{S}(\omega) \\ - \left\langle \left\{ \hat{T}^{obs}(\mathbf{x}_A, \omega) \right\}^* \hat{T}^{obs}(\mathbf{x}_B, \omega) \right\rangle. \end{aligned} \quad (2.108)$$

The above relation was derived by [Wapenaar et al. \[2002\]](#) and proved Claerbout's conjecture for the retrieval of the reflection response from the crosscorrelation of transmission responses from noise sources in a 3D inhomogeneous lossless medium.

### ■ 2.2.5 SI relations for a direct migration of noise recordings

Equation 2.84 can be used to derive a useful relation for direct migration of noise measurements at the surface. With this relation, one can migrate the recorded noise transmission responses, instead of first retrieving the reflection responses at all the surface points for all retrieved source positions followed by migration. This direct migration is based on the shot-profile migration scheme [[Claerbout, 1971](#)], which consists of downward extrapolation of the one-way wavefields followed by crosscorrelation. The method was proposed by Artman and was proved by Wapenaar [[Artman et al., 2004](#)]. Downward extrapolation of  $\hat{R}^+(\mathbf{x}_A, \mathbf{x}_B, \omega)$  to some level in the subsurface

can be described by [Wapenaar and Berkhout, 1989]

$$\hat{R}^+(\boldsymbol{\xi}_A, \boldsymbol{\xi}_B, \omega) = \int_{\partial\mathbb{D}_0} \int_{\partial\mathbb{D}_0} \left\{ \hat{W}^+(\boldsymbol{\xi}_A, \mathbf{x}_A, \omega) \right\}^* \hat{R}^+(\mathbf{x}_A, \mathbf{x}_B, \omega) \times \left\{ \hat{W}^-(\mathbf{x}_B, \boldsymbol{\xi}_B, \omega) \right\}^* d^2\mathbf{x}_B d^2\mathbf{x}_A, \quad (2.109)$$

where  $\hat{R}^+(\boldsymbol{\xi}_A, \boldsymbol{\xi}_B, \omega)$  is the extrapolated reflection response that one would observe at point  $\boldsymbol{\xi}_A$  in the subsurface when there would be a source at  $\boldsymbol{\xi}_B$  and  $\hat{W}^+(\boldsymbol{\xi}_A, \mathbf{x}_A, \omega)$  and  $\hat{W}^-(\mathbf{x}_B, \boldsymbol{\xi}_B, \omega)$  are forward extrapolation operators (see Wapenaar and Berkhout [1989] for the definition of these operators). Substitution of equation 2.108 into equation 2.109 gives

$$\hat{R}^+(\boldsymbol{\xi}_A, \boldsymbol{\xi}_B, \omega) \hat{S}(\omega) = - \int_{\partial\mathbb{D}_0} \int_{\partial\mathbb{D}_0} \left\{ \hat{W}^+(\boldsymbol{\xi}_A, \mathbf{x}_A, \omega) \right\}^* \times \left\langle \left\{ \hat{T}^{obs}(\mathbf{x}_A, \omega) \right\}^* \hat{T}^{obs}(\mathbf{x}_B, \omega) \right\rangle \left\{ \hat{W}^-(\mathbf{x}_B, \boldsymbol{\xi}_B, \omega) \right\}^* d^2\mathbf{x}_B d^2\mathbf{x}_A + \text{acausal terms}. \quad (2.110)$$

Rearranging the right-hand side of the above equation, making use of the reciprocity relation for the forward-extrapolation operator  $\hat{W}^-(\mathbf{x}_B, \boldsymbol{\xi}_B, \omega) = \hat{W}^+(\boldsymbol{\xi}_B, \mathbf{x}_B, \omega)$ , and using the fact that the reflection response of the free-surface is  $r^- = -1$ , one obtains

$$\hat{R}^+(\boldsymbol{\xi}_A, \boldsymbol{\xi}_B, \omega) \hat{S}(\omega) = \left\langle \int_{\partial\mathbb{D}_0} \left\{ \hat{W}^+(\boldsymbol{\xi}_A, \mathbf{x}_A, \omega) r^- \hat{T}^{obs}(\mathbf{x}_A, \omega) \right\}^* d^2\mathbf{x}_B \times \int_{\partial\mathbb{D}_0} \left\{ \hat{W}^+(\boldsymbol{\xi}_B, \mathbf{x}_B, \omega) \right\}^* \hat{T}^{obs}(\mathbf{x}_B, \omega) d^2\mathbf{x}_A \right\rangle + \text{acausal terms}. \quad (2.111)$$

The above equation shows that the reflection response at a subsurface level is retrieved by inverse extrapolation of an observed transmission response  $\hat{T}^{obs}(\mathbf{x}_B, \omega)$  for all  $\mathbf{x}_B$  to some subsurface level and forward extrapolation of a downward-reflected observed transmission response  $\hat{T}^{obs}(\mathbf{x}_A, \omega)$  for all  $\mathbf{x}_A$  to the same subsurface level followed by crosscorrelation. If subsequently, a summation is performed over all frequencies, an image of the



subsurface at that level is obtained. The direct migration of observed noise transmission responses and the shot-profile migration of retrieved reflection responses produce identical results. The choice for one or the other depends on the specific application.

### ■ 2.2.6 SI relations for impulsive sources in an elastic medium

To obtain the elastodynamic SI relations for one-way wavefields, similar choices are made for the states  $\mathcal{A}$  and  $\mathcal{B}$  as in the acoustic case. Just like in the acoustic case, one can choose impulsive sources of downgoing waves at points  $\mathbf{x}_{\mathcal{A}} = (\mathbf{x}_{H,\mathcal{A}}, x_{3,0})$  and  $\mathbf{x}_{\mathcal{B}} = (\mathbf{x}_{H,\mathcal{B}}, x_{3,0})$  for states  $\mathcal{A}$  and  $\mathcal{B}$ , respectively. An alternative choice is: impulsive sources of upgoing waves at point  $\mathbf{x}_{\mathcal{A}} = (\mathbf{x}_{H,\mathcal{A}}, x_{3,m})$  and of downgoing waves at  $\mathbf{x}_{\mathcal{B}} = (\mathbf{x}_{H,\mathcal{B}}, x_{3,0})$  for states  $\mathcal{A}$  and  $\mathcal{B}$ , respectively. With these choices, the wavefields at the top and bottom boundary can be expressed in terms of reflection and transmission responses, as it was done in Tables 2.8 and 2.9, but now the scalar quantities are replaced by their elastodynamic vector and matrix counterparts:

$$\hat{\mathbf{P}}^{\pm}(\mathbf{x}, \mathbf{x}_{\mathcal{A}(\mathcal{B})}, \omega) = \begin{pmatrix} \hat{\Phi}^{\pm} \\ \hat{\Psi}_x^{\pm} \\ \hat{\Psi}_y^{\pm} \end{pmatrix}(\mathbf{x}, \mathbf{x}_{\mathcal{A}(\mathcal{B})}, \omega), \quad (2.112a)$$

$$\hat{\mathbf{R}}^{\pm}(\mathbf{x}, \mathbf{x}_{\mathcal{A}(\mathcal{B})}, \omega) = \begin{pmatrix} \hat{R}_{\phi,\phi}^{\pm} & \hat{R}_{\phi,\psi_x}^{\pm} & \hat{R}_{\phi,\psi_y}^{\pm} \\ \hat{R}_{\psi_x,\phi}^{\pm} & \hat{R}_{\psi_x,\psi_x}^{\pm} & \hat{R}_{\psi_x,\psi_y}^{\pm} \\ \hat{R}_{\psi_y,\phi}^{\pm} & \hat{R}_{\psi_y,\psi_x}^{\pm} & \hat{R}_{\psi_y,\psi_y}^{\pm} \end{pmatrix}(\mathbf{x}, \mathbf{x}_{\mathcal{A}(\mathcal{B})}, \omega), \quad (2.112b)$$

$$\hat{\mathbf{T}}^{\pm}(\mathbf{x}, \mathbf{x}_{\mathcal{A}(\mathcal{B})}, \omega) = \begin{pmatrix} \hat{T}_{\phi,\phi}^{\pm} & \hat{T}_{\phi,\psi_x}^{\pm} & \hat{T}_{\phi,\psi_y}^{\pm} \\ \hat{T}_{\psi_x,\phi}^{\pm} & \hat{T}_{\psi_x,\psi_x}^{\pm} & \hat{T}_{\psi_x,\psi_y}^{\pm} \\ \hat{T}_{\psi_y,\phi}^{\pm} & \hat{T}_{\psi_y,\psi_x}^{\pm} & \hat{T}_{\psi_y,\psi_y}^{\pm} \end{pmatrix}(\mathbf{x}, \mathbf{x}_{\mathcal{A}(\mathcal{B})}, \omega), \quad (2.112c)$$

$$\hat{\mathbf{f}}^{-}(\mathbf{x}) = \begin{pmatrix} \hat{r}_{\phi,\phi}^{-} & \hat{r}_{\phi,\psi_x}^{-} & \hat{r}_{\phi,\psi_y}^{-} \\ \hat{r}_{\psi_x,\phi}^{-} & \hat{r}_{\psi_x,\psi_x}^{-} & \hat{r}_{\psi_x,\psi_y}^{-} \\ \hat{r}_{\psi_y,\phi}^{-} & \hat{r}_{\psi_y,\psi_x}^{-} & \hat{r}_{\psi_y,\psi_y}^{-} \end{pmatrix}(\mathbf{x}). \quad (2.112d)$$

In the above equations, the right subscript denotes the incident wavefield, while the left subscript denotes the scattered wavefield. The operator matrix

$\hat{\mathbf{f}}^-(\mathbf{x})$  obeys the properties

$$\{\hat{\mathbf{f}}^-(\mathbf{x})\}^t = \hat{\mathbf{f}}^-(\mathbf{x}), \quad (2.113a)$$

$$\{\hat{\mathbf{f}}^-(\mathbf{x})\}^\dagger \hat{\mathbf{f}}^-(\mathbf{x}) = \mathbf{I}, \quad (2.113b)$$

where  $\mathbf{I}$  is the 3x3 identity matrix.

When the elastodynamic counterparts 2.112 of the acoustic quantities from the middle and the right columns of Table 2.8 are substituted in the one-way wavefield convolution-type reciprocity relation 2.96, the result is

$$\hat{\mathbf{R}}^+(\mathbf{x}_A, \mathbf{x}_B, \omega) = \left\{ \hat{\mathbf{R}}^+(\mathbf{x}_B, \mathbf{x}_A, \omega) \right\}^T. \quad (2.114)$$

If the elastodynamic counterparts 2.112 of the acoustic quantities from the middle and the right columns of Table 2.9 are substituted into equation 2.96, the result is

$$\hat{\mathbf{T}}^+(\mathbf{x}_A, \mathbf{x}_B, \omega) = \left\{ \hat{\mathbf{T}}^-(\mathbf{x}_B, \mathbf{x}_A, \omega) \right\}^T. \quad (2.115)$$

Substituting the elastodynamic counterparts 2.112 of the acoustic quantities from the middle and the right columns of Table 2.8 into equation 2.97, using the reciprocity relations 2.114 and 2.115, and making use of the property 2.112b of the free-surface reflection operator matrix, one obtains

$$\begin{aligned} -\hat{\mathbf{f}}^-(\mathbf{x}_A) \hat{\mathbf{R}}^+(\mathbf{x}_A, \mathbf{x}_B, \omega) - \left\{ \hat{\mathbf{R}}^+(\mathbf{x}_A, \mathbf{x}_B, \omega) \right\}^* \left\{ \hat{\mathbf{f}}^-(\mathbf{x}_B) \right\}^\dagger = \\ \mathbf{I} \delta(\mathbf{x}_{H,B} - \mathbf{x}_{H,A}) - \int_{\partial \mathbb{D}_m} \left\{ \hat{\mathbf{T}}^-(\mathbf{x}_A, \mathbf{x}, \omega) \right\}^* \left\{ \hat{\mathbf{T}}^-(\mathbf{x}_B, \mathbf{x}, \omega) \right\}^T d^2 \mathbf{x}. \end{aligned} \quad (2.116)$$

The equation above is the elastodynamic one-way wavefield SI relation.

### ■ 2.2.7 SI relation for transient sources in an elastic medium

When the sources in the subsurface are band-limited with wavelet with frequency spectrum  $\hat{\mathbf{S}}(\mathbf{x}, \omega)$ , the one-way transmission matrix at the points  $\mathbf{x}_A$  and  $\mathbf{x}_B$  at the surface can be seen as a band-pass filtered variant of the impulse-response transmission matrix 2.112c and can be written as

$$\hat{\mathbf{T}}^{obs}(\mathbf{x}_{A(B)}, \mathbf{x}, \omega) = \hat{\mathbf{T}}^-(\mathbf{x}_{A(B)}, \mathbf{x}, \omega) \hat{\mathbf{S}}(\mathbf{x}, \omega), \quad (2.117)$$

where  $\hat{\mathbf{s}}(\mathbf{x}, \omega) = \text{diag} \left( \hat{S}_{\Phi}^{-}(\mathbf{x}, \omega), \hat{S}_{\Psi_x}^{-}(\mathbf{x}, \omega), \hat{S}_{\Psi_y}^{-}(\mathbf{x}, \omega) \right)$ . In that case, one can introduce equation 2.117 for states  $\mathcal{A}$  and  $\mathcal{B}$  into the elastodynamic one-way SI relation 2.116 to obtain

$$\begin{aligned} & - \hat{\mathbf{r}}^{-}(\mathbf{x}_A) \hat{\mathbf{R}}^{+}(\mathbf{x}_A, \mathbf{x}_B, \omega) \hat{S}_0(\omega) \\ & - \left\{ \hat{\mathbf{R}}^{+}(\mathbf{x}_A, \mathbf{x}_B, \omega) \right\}^* \left\{ \hat{\mathbf{r}}^{-}(\mathbf{x}_B) \right\}^{\dagger} \hat{S}_0(\omega) = \mathbf{I} \delta(\mathbf{x}_{H,B} - \mathbf{x}_{H,A}) \hat{S}_0(\omega) \\ & - \int_{\partial \mathbb{D}_m} \left\{ \hat{\mathbf{T}}^{obs}(\mathbf{x}_A, \mathbf{x}, \omega) \right\}^* \hat{\mathbf{F}}(\mathbf{x}, \omega) \left\{ \hat{\mathbf{T}}^{obs}(\mathbf{x}_B, \mathbf{x}, \omega) \right\}^T d^2 \mathbf{x}, \quad (2.118) \end{aligned}$$

where

$$\hat{\mathbf{F}}(\mathbf{x}, \omega) = \begin{pmatrix} \frac{\hat{S}_0(\omega)}{\hat{S}_{\Phi}^{-*}(\mathbf{x}, \omega) \hat{S}_{\Phi}^{-}(\mathbf{x}, \omega)} & 0 & 0 \\ 0 & \frac{\hat{S}_0(\omega)}{\hat{S}_{\Psi_x}^{-*}(\mathbf{x}, \omega) \hat{S}_{\Psi_x}^{-}(\mathbf{x}, \omega)} & 0 \\ 0 & 0 & \frac{\hat{S}_0(\omega)}{\hat{S}_{\Psi_y}^{-*}(\mathbf{x}, \omega) \hat{S}_{\Psi_y}^{-}(\mathbf{x}, \omega)} \end{pmatrix} \quad (2.119)$$

is a matrix that compensates for the different source-type spectra at the different source points with  $\hat{S}_0(\omega)$  an average, arbitrary chosen power spectrum. The above SI relation can be used when separate recordings can be taken at  $\mathbf{x}_A$  and  $\mathbf{x}_B$  from each of the transient sources on  $\partial \mathbb{D}_m$ .

## ■ 2.2.8 SI relation for noise sources in an elastic medium

In the presence of simultaneously acting, mutually uncorrelated noise sources in the subsurface along the boundary  $\partial \mathbb{D}_m$  with equal individual power spectrum  $\hat{S}(\omega)$ , the one-way transmission matrix for states  $\mathcal{A}$  and  $\mathcal{B}$  would be

$$\hat{\mathbf{T}}^{obs}(\mathbf{x}_A, \omega) = \int_{\partial \mathbb{D}_m} \hat{\mathbf{T}}^{-}(\mathbf{x}_A, \mathbf{x}, \omega) \hat{\mathbf{N}}(\mathbf{x}, \omega) d^2 \mathbf{x} \quad (2.120a)$$

$$\hat{\mathbf{T}}^{obs}(\mathbf{x}_B, \omega) = \int_{\partial \mathbb{D}_m} \hat{\mathbf{T}}^{-}(\mathbf{x}_B, \mathbf{x}', \omega) \hat{\mathbf{N}}(\mathbf{x}', \omega) d^2 \mathbf{x}', \quad (2.120b)$$

where  $\hat{\mathbf{N}}(\mathbf{x}, \omega) = \left( \hat{N}_{\Phi}(\mathbf{x}, \omega), \hat{N}_{\Psi_x}(\mathbf{x}, \omega), \hat{N}_{\Psi_y}(\mathbf{x}, \omega) \right)^T$  contains the noise spectra for the different noise types. As the sources are mutually uncorre-

lated, the crosscorrelation of the noise spectra would give

$$\left\langle \left\{ \hat{\mathbf{N}}(\mathbf{x}, \omega) \right\}^* \left\{ \hat{\mathbf{N}}(\mathbf{x}', \omega) \right\} \right\rangle = \begin{pmatrix} \delta(\mathbf{x} - \mathbf{x}') & 0 & 0 \\ 0 & \delta(\mathbf{x} - \mathbf{x}') & 0 \\ 0 & 0 & \delta(\mathbf{x} - \mathbf{x}') \end{pmatrix} \hat{S}(\omega). \quad (2.121)$$

In such a way, the crosscorrelation of the left-hand sides of equations 2.120 can be written as

$$\left\langle \left\{ \hat{\mathbf{T}}^{obs}(\mathbf{x}_A, \omega) \right\}^* \left\{ \hat{\mathbf{T}}^{obs}(\mathbf{x}_B, \omega) \right\}^T \right\rangle = \int_{\partial\mathbb{D}_m} \left\{ \hat{\mathbf{T}}^-(\mathbf{x}_A, \mathbf{x}, \omega) \right\}^* \left\{ \hat{\mathbf{T}}^-(\mathbf{x}_B, \mathbf{x}, \omega) \right\}^T \hat{S}(\omega) d^2\mathbf{x}. \quad (2.122)$$

Comparing the equation above to equation 2.116, it can be concluded that

$$\begin{aligned} & -\hat{\mathbf{r}}^-(\mathbf{x}_A) \hat{\mathbf{R}}^+(\mathbf{x}_A, \mathbf{x}_B, \omega) \hat{S}(\omega) \\ & - \left\{ \hat{\mathbf{R}}^+(\mathbf{x}_A, \mathbf{x}_B, \omega) \right\}^* \left\{ \hat{\mathbf{r}}^-(\mathbf{x}_B) \right\}^\dagger \hat{S}(\omega) = \mathbf{I} \delta(\mathbf{x}_{H,B} - \mathbf{x}_{H,A}) \hat{S}(\omega) \\ & - \left\langle \left\{ \hat{\mathbf{T}}^{obs}(\mathbf{x}_A, \omega) \right\}^* \left\{ \hat{\mathbf{T}}^{obs}(\mathbf{x}_B, \omega) \right\}^T \right\rangle. \end{aligned} \quad (2.123)$$

The above equation shows that the flux-normalized components of the reflection response matrix can be retrieved by crosscorrelating the corresponding flux-normalized components of the recorded at the surface noise transmission response.



## Retrieval of the reflection response: numerical modelling results

---

[Rickett and Claerbout \[1996\]](#) and [Rickett \[1996\]](#) tested Claerbout's conjecture that for a 3D inhomogeneous acoustic medium, one should crosscorrelate the seismic noise transmission responses at two points at the free surface to retrieve the seismic reflection response between these two points. First, they used phase-shift modelling of random incident plane waves to show that crosscorrelating noise traces gives the correct reflection kinematics for acoustic horizontally layered and point-diffractor models. Later, they applied finite-difference modelling to check the robustness of retrieved reflection seismograms for acoustic models with moderate lateral velocity variation in the case of sources of ambient noise taken to be at infinity (planar wavefronts) and sources within the zone of interest (curved wavefronts). The modelling results in this section can be seen as a continuation of Rickett and Claerbout's research, but based on the firm theoretical derivations shown in Chapter 2 and expanded to elastic and electromagnetic waves. [Van Manen et](#)

al. [2005] and Van Manen et al. [2006] used relations similar to 2.15 and 2.37 to develop efficient modelling scheme for acoustic and elastic waves. Using this scheme, they showed that the Green's function between any two points inside a domain could be modelled from the crosscorrelation of recordings from monopole and dipole sources, in the acoustic case, and from volume-force and deformation-rate sources, in the elastic case, surrounding the domain. For exploration or seismological purposes, though, it is interesting to retrieve the reflection response at the Earth's surface and this is what is investigated in the following text.

In this chapter, several SI and EMI relations, derived in Section 2.1 from two-way wavefield reciprocity relations, are investigated for application in exploration with the help of numerical-modelling data. The modelling is performed with 2D finite-difference and 2D finite-element schemes. The interferometric relations are applied for the retrieval of reflection responses at the Earth's surface. For the acoustic and the elastic cases, the Earth's surface is a free surface, meaning that the acoustic pressure and the elastodynamic stress normal to the Earth's surface vanish at the surface. As explained in Sections 2.1.3 and 2.1.7, this means that for the retrieval of the reflection response only crosscorrelation of responses from subsurface sources are required. Using stationary-phase arguments [Wapenaar and Fokkema, 2006], it can be shown that the responses from sources close to Earth's surface will contribute mainly to a retrieval of waves traveling along the surface, while responses from sources deeper in the subsurface will mainly contribute to the retrieval of reflected waves. For this reason, the modelling is performed with sources placed deep in the subsurface. Results are shown of the retrieval of the reflection response in cases of transient and noise sources in the subsurface.

The interferometric relations in Section 2.1 were derived for the case of a lossless medium. Here also the quality of the retrieved results is investigated when the propagating waves experience losses in the medium.

For the electromagnetic case, the Earth's surface is not a free surface. This requires that for the retrieval of the reflection response at the receiver locations sources be present all around these receivers. In practical situations, this means that one needs to record responses from sources above as well as below the receivers. Using numerical-modelling data, results are shown from the retrieval of the electromagnetic reflection response for the case of

recordings from noise sources above and below the receivers.

### 3.1 Retrieval of the acoustic reflection response

In Sections 2.1.2-2.1.5 relations were derived for the retrieval of new acoustic recordings from the crosscorrelation of existing acoustic recordings. For exploration or seismological purposes, it is interesting to retrieve the reflection response at the Earth's surface. As explained in section 2.1.3, to retrieve the reflection response between two receivers at the surface, one needs to crosscorrelate recorded responses only from sources in the subsurface. Furthermore, using stationary-phase arguments [Wapenaar and Fokkema, 2006], it can be shown that crosscorrelation of recordings from sources close to the surface will mainly contribute to the retrieval of waves propagating along the surface, while crosscorrelation of recordings from sources deeper in the subsurface (transmission recordings) will contribute mainly to the retrieval of reflected arrivals. Relation 2.23 was derived for the case of recordings from impulsive sources. In practice, the subsurface sources are always band-limited. For this reason, in the following the acoustic SI relations 2.25 and 2.30 are investigated in the case of transient and noise sources in the subsurface, respectively. The derived relations are valid for any 3D inhomogeneous lossless medium, but for illustrative purposes 2D examples are shown. These examples were obtained from transmission recordings at the free surface generated with a finite-difference modelling scheme using DELPHI software.

#### ■ 3.1.1 Retrieval of the acoustic reflection response from recordings from transient subsurface sources

Consider a lossless 2D acoustic subsurface model as shown in Figure 3.1. A receiver array, represented by the triangles, is placed along the free surface. The receiver array starts at 1200 m and goes to 6800 m with spacing between receivers of 10 m. The subsurface consists of three layers, where a part of the boundary between the first two layers has the shape of a syncline. From relation 2.25 and the explanation in Section 2.1.3 it follows that in order to retrieve reflection arrivals, one needs to crosscorrelate recordings from sources along the part of the boundary  $\partial\mathbb{D}$  lying in the subsurface, i.e., along



$\partial\mathbb{D}_m$ . The subsurface sources, represented by the stars, lie at depth 775 m. In the horizontal direction, the sources are placed every 25 m starting from 1200 m and going until 6800 m. The source wavelet has the form of a first derivative of a Gaussian function with a peak frequency of 25 Hz. The source separation is chosen to be smaller than half the dominant wavelength in the layer with the lowest propagation velocity. Such choice of source spacing allows to consider the source distribution as continuous. The medium below the source level is homogeneous.

If a source in the subsurface is set off, along the receivers at the surface a transmission common-source gather is recorded. Figure 3.2(a) shows a transmission common-source panel from a subsurface source at horizontal distance 4000 m. By setting off each of the subsurface sources separately in time, 225 transmission common-source gathers are obtained.

For the retrieval of the reflection response with the help of equation 2.25 the following procedure is performed. A receiver position is chosen at which

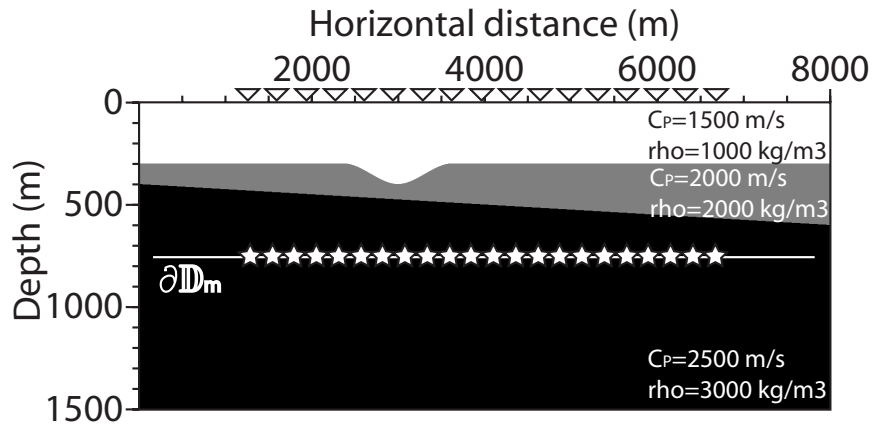


**Figure 3.1:** A lossless 2D acoustic subsurface model. There are 561 receivers (represented by the triangles) at the free surface starting from 1200 m until 6800 m, with spacing 10 m. There are 225 transient sources (the stars) in the subsurface along a boundary  $\partial\mathbb{D}_m$ . The subsurface sources are placed every 25 m starting from 1200 m and going until 6800 m.

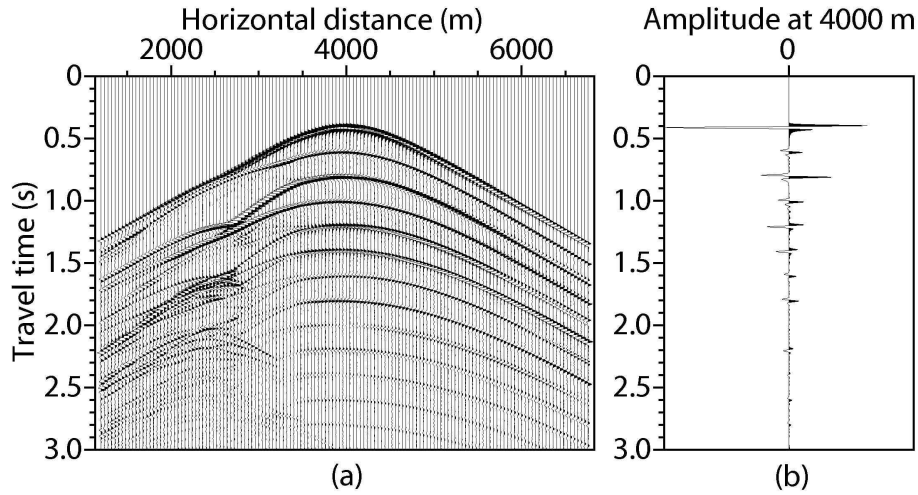


**Figure 3.2:** (a) A transmission gather as observed along the receivers at the free surface due to a subsurface source at horizontal distance 4000 m. The amplitudes are clipped to bring forward later arrivals. (b) A transmission trace observed at the receiver at horizontal distance 4000 m due to the same source as in (a).

a source is to be retrieved, for example at  $\mathbf{x}_B = (4000, 0)$  m. The trace at this position is extracted from one transmission common-source gather, see Figure 3.2(b). Such a trace represents  $p^{obs}(\mathbf{x}_B, \mathbf{x}, t)$  in the equation and will be called a "master trace". A trace at another receiver location, representing  $p^{obs}(\mathbf{x}_A, \mathbf{x}, t)$ , is extracted from the same transmission common-source gather and crosscorrelated with the master trace. The crosscorrelation result represents the integrand in equation 2.25 for a single source position  $\mathbf{x}$ . The correlation process between the master trace and the trace  $p^{obs}(\mathbf{x}_A, \mathbf{x}, t)$  is repeated for all 225 subsurface sources to produce 225 correlation traces. When placed one after the other, the correlation traces make a correlation panel which represents the integrand in equation 2.25 for multiple source positions  $\mathbf{x}$ . Figure 3.3(a) shows an example correlation panel for a master trace at  $\mathbf{x}_B = (4000, 0)$  m and a second trace at  $\mathbf{x}_A = (4000, 0)$  m, i.e, when the master trace has been autocorrelated. The horizontal axis represents subsurface source position. According to the integral in equation 2.25, the traces

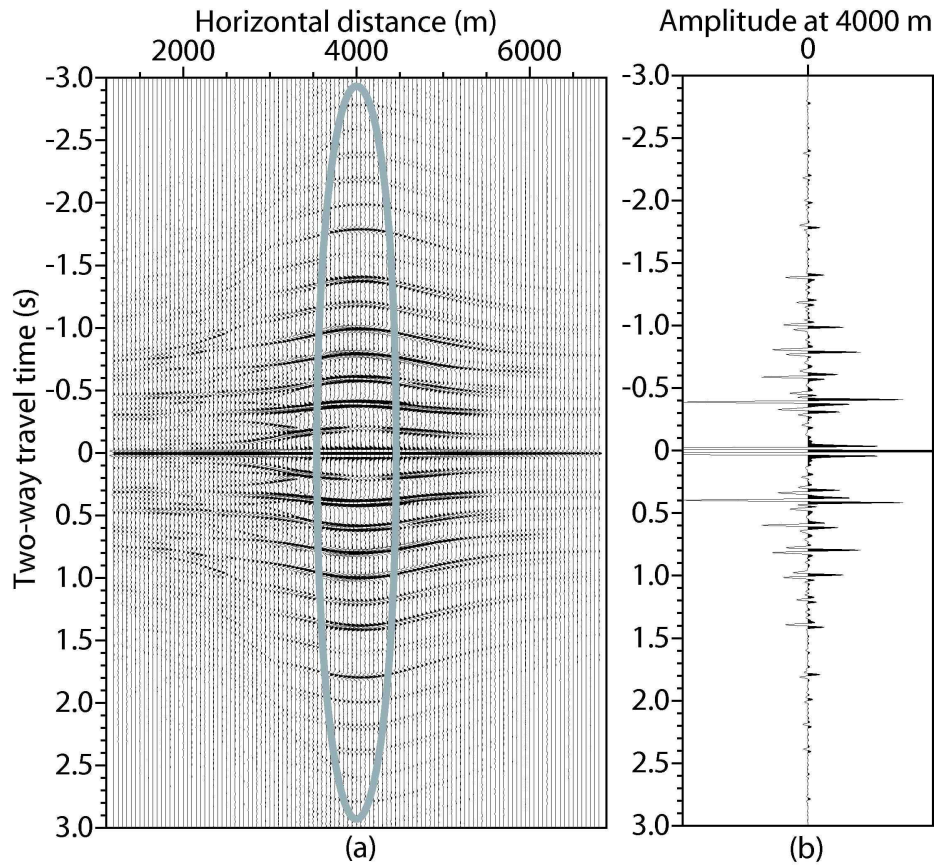


**Figure 3.3:** (a) A correlation panel obtained from the correlation of a master trace at  $\mathbf{x}_B = (4000, 0)$  m with a trace at  $\mathbf{x}_A = (4000, 0)$  m for each subsurface source position. (b) The result from the summation of the traces in (a) along the subsurface source positions. The grey ellipse in (a) highlights the stationary-phase region which, after summation, produces the correct events in (b).

in the correlation panel are summed together to produce a retrieved reflection trace and its time-reversed version at  $\mathbf{x}_A$  as if from a transient source at  $\mathbf{x}_B$ . The source wavelet of the retrieved trace is the autocorrelation of the subsurface source wavelet. Figure 3.3(b) depicts the resulting trace from the summation of the traces in Figure 3.3(a) along the subsurface source positions. This trace represents a retrieved reflection trace at  $\mathbf{x}_A = (4000, 0)$  m due to a surface source at  $\mathbf{x}_B = (4000, 0)$  m, i.e., a retrieved zero-offset trace. Inspecting Figure 3.3, it can be observed that the retrieved reflection events are produced from the constructive interference of correlation traces lying in the stationary-phase region (highlighted by the grey ellipse in Figure 3.3(a)). Between these retrieved events, there are additional weak events resulting from the incomplete destructive interference at the ends of the source array. Keeping the master trace position fixed and repeating the above-described correlation and summation procedure for  $\mathbf{x}_A$  chosen at each of the available receiver positions, a reflection common-source gather and its time-reversed version are retrieved as if from a surface source at the position of the master trace. Figure 3.4 shows the retrieved reflection common-source gather and its time-reversed version for a retrieved source position at  $\mathbf{x}_B = (4000, 0)$  m. Note that in this gather the trace at horizontal distance 4000 m is actually the trace from Figure 3.3(b). The "x"-like event at the middle of the figure represents a temporal and spatial delta function smeared both in time and space due to the limited subsurface source aperture. Equation 2.25 predicts that the retrieved reflection common-source gather and its time-reversed version, i.e., the causal and anti-causal parts in the figure, should be symmetric over the time-zero axis. It can be observed that this is indeed the case for retrieved traces around the zero-offset trace. For these traces the subsurface source distribution is optimal and all stationary-phase regions are completely present in the respective correlation panels. It can also be observed that the retrieved causal and anti-causal parts of the traces close to the ends of the receiver array are not symmetric any more. This result can be understood by looking at Figure 3.5, which depicts the correlation panel from the cross-correlation of an observed trace at  $\mathbf{x}_A = (2000, 0)$  m with a master trace at  $\mathbf{x}_B = (4000, 0)$  m for each subsurface source position. In this case, the stationary-phase region, that will contribute to the retrieval of reflection arrivals at negative times, has moved to the end of the subsurface source array and parts of this region are outside the limits of the subsurface array. In the

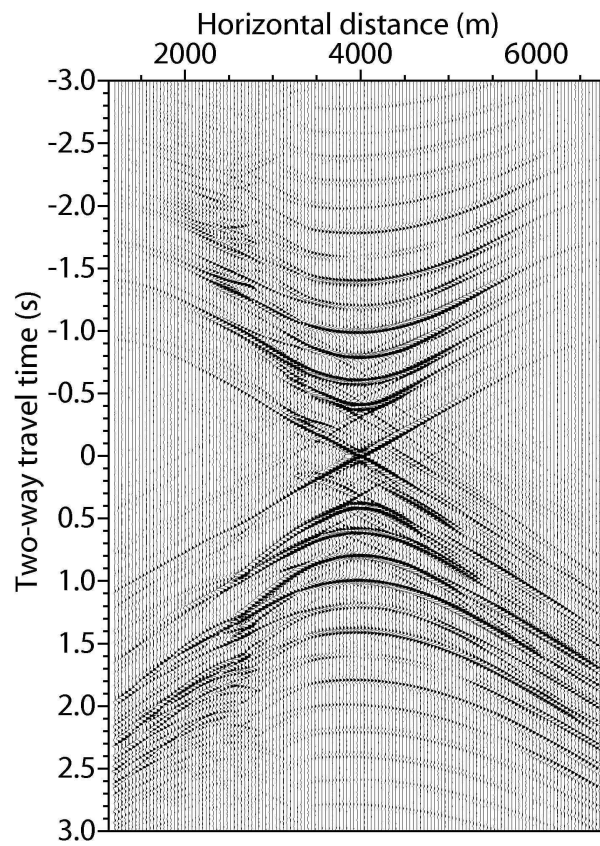


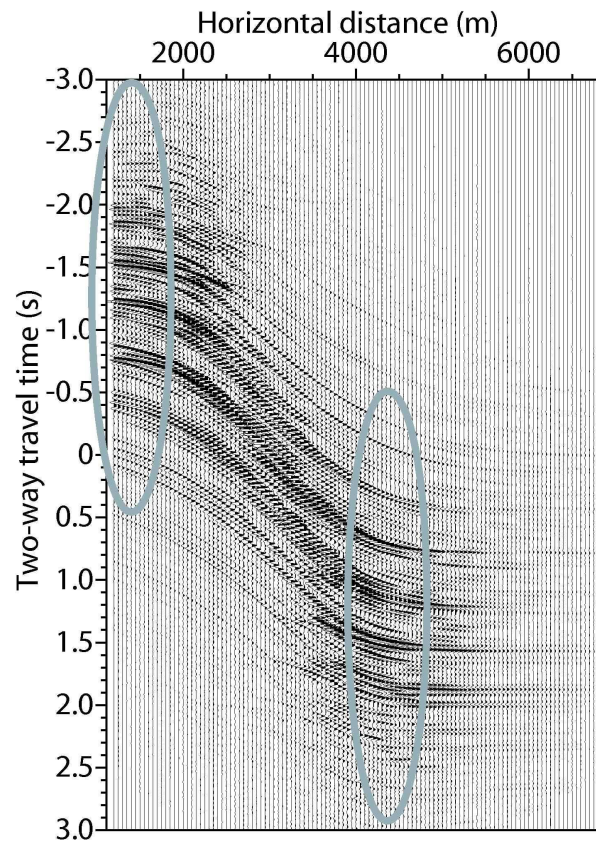
**Figure 3.4:** A retrieved reflection common-source gather and its time-reversed version for a retrieved source position at  $\mathbf{x}_B = (4000, 0)$  m.

consecutive integration over the subsurface source position, the constructive interference in the negative times will not be complete and the retrieved events will appear at times earlier than expected. This gives rise to the "curling" at the ends of the reflection hyperbolae in the anti-causal part. At the same time, the stationary-phase region at positive times is well inside the limits of the subsurface source array, see Figure 3.5.

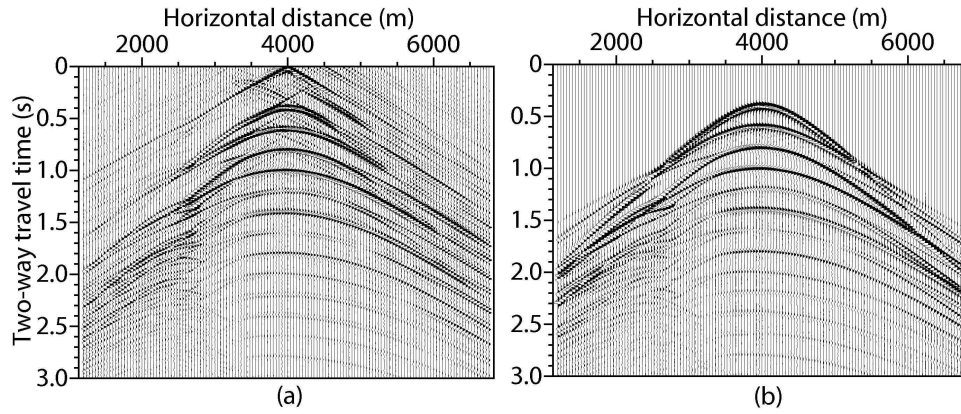
From the above explanation it follows that when limits of the subsurface source array are long enough to capture, or illuminate, the needed stationary-phase regions, the anti-causal part of the retrieved result can simply be muted. When this is not the case, or in more realistic situations, when no information is available about the subsurface and the subsurface sources, both the retrieved causal and anti-causal parts should be taken into consideration as some reflection events can be retrieved at positive times and some at negative. In this and the following section, the anti-causal part of the retrieved results is muted.

Figure 3.6 shows the retrieved reflection common-source gather for a retrieved source position at  $\mathbf{x}_B = (4000, 0)$  m, after muting the negative times, and the reflection common-source gather, after removing the direct-wave arrival, obtained directly through numerical modelling. Equation 2.25 shows that for practical applications the recorded transmission responses should be deconvolved before crosscorrelation, while the reflection response should be convolved with a desired wavelet. Here, though, another approach is followed. The numerically modelled reflection response was obtained using the same wavelet as the transmission responses, i.e., a first derivative of a Gaussian wavelet. Because of this, the directly modelled reflection response is convolved with the a first derivative of a Gaussian wavelet, resulting in a negative autocorrelation of the source wavelet, which is produced by crosscorrelating the modelled transmission responses. After equalizing in the above-mentioned way the wavelets in the directly modelled reflection gather and the retrieved reflection gather, the events they contain can be compared. Looking at the two gathers in the figure, it can be seen that the primary reflections and their multiples have been kinematically correctly retrieved. The limited subsurface source aperture leads, as explained above, to an incomplete destructive interference of events away from the stationary region, which gives rise to the linear crossing events above the apices of the reflection hyperbolae in the retrieved common-source gather. Due to the fact





**Figure 3.5:** A correlation panel obtained from the correlation of a master trace at  $\mathbf{x}_B = (4000, 0)$  m with a trace at  $\mathbf{x}_A = (2000, 0)$  m for each subsurface source position.



**Figure 3.6:** (a) A retrieved reflection common-source gather for a retrieved surface source position at  $\mathbf{x}_B = (4000, 0)$  m. (b) A reflection common-source gather obtained directly through numerical modelling. The direct-wave arrival has been removed from (b).

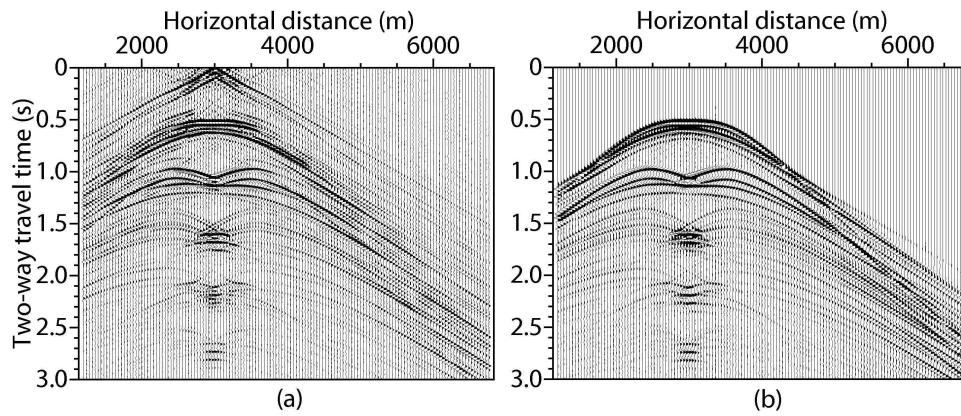


**Figure 3.7:** As in Figure 3.6 but for a retrieved surface source position at  $\mathbf{x}_B = (3000, 0)$  m.



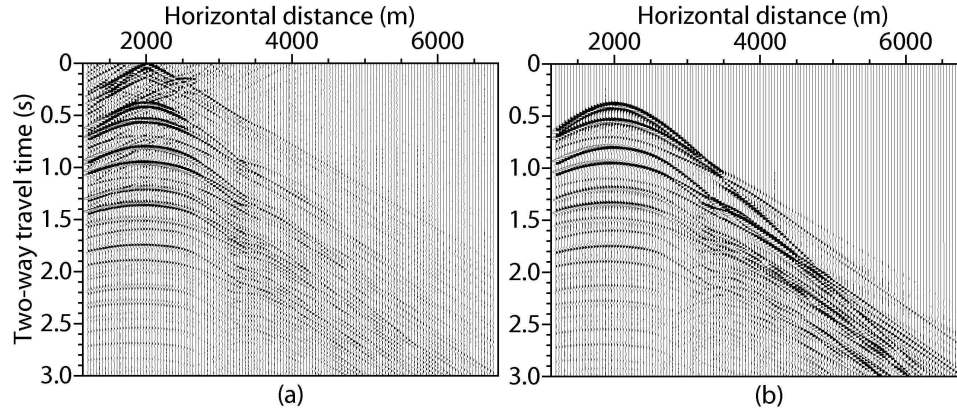


**Figure 3.8:** As in Figure 3.6 but for a retrieved surface source position at  $\mathbf{x}_B = (2000, 0)$  m.

that no use was made of sources close to the surface, refraction events are not properly reconstructed.

By changing the master-trace position, the retrieved surface source position is changing too. Figures 3.7 and 3.8 show the comparison between retrieved reflection common-source gathers and reflection gathers directly obtained through numerical modelling for surface source positions at horizontal distances 3000 m and 2000 m, respectively. From these figures it is visible that when the master trace position approaches the end of the subsurface source array, the quality of the retrieved reflection arrivals opposite to this end diminishes.

Equation 2.25 was derived with the assumption that the medium outside  $\partial\mathbb{D}$  is homogeneous and isotropic. In accordance with this assumption, the examples above were obtained for a model where the medium below  $\partial\mathbb{D}_m$  was homogeneous. Consider now a model as in Figure 3.9, where there is an extra reflector below the source level. This obviously does not comply with the assumptions in the derivation of equation 2.25. Figure 3.10 shows a common-source transmission gather for this model when a transient source at horizontal distance 4000 m is set off. The presence of the reflector under the source level results in extra reflection events, like the ones indicated by

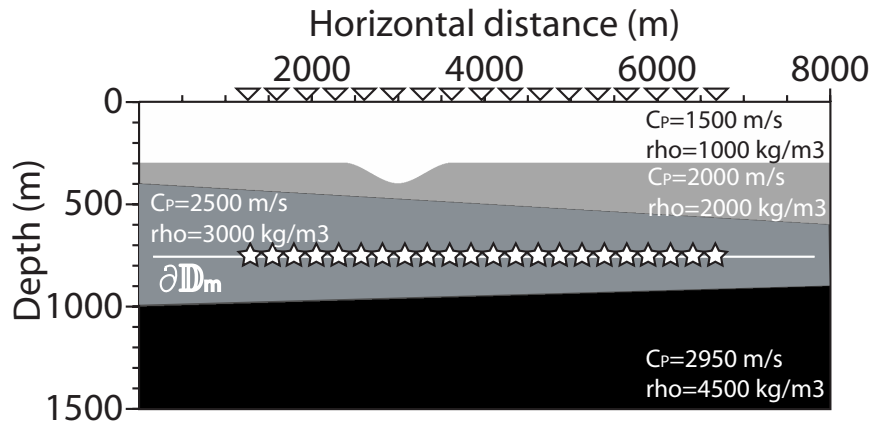


**Figure 3.9:** A lossless 2D acoustic subsurface model. The difference with the model in Figure 3.1 is in the extra reflector below the source level. The source and receiver array geometries are the same.

the black pointers and with apices at around 0.54 s and 0.76 s. If the master trace is chosen to be  $\mathbf{x}_B = (4000, 0)$  m and one autocorrelates this trace for each subsurface source position, a correlation panel is obtained as the one in Figure 3.11. Compared to the correlation panel in Figure 3.3(a), inside the stationary-phase region in Figure 3.11(a) there are several additional events. These events, when summed along the source position (the integration in equation 2.25 along  $\partial\mathbb{D}_m$ ), produce additional arrivals in the retrieved zero-offset trace in Figure 3.11(b), like the ones at around 0.14 s, 0.54 s, and 0.95 s. For easier interpretation of these events, a comparison is shown in Figure 3.12 between a retrieved reflection common-source gather and a reflection common-source gather directly obtained through numerical modelling for a surface source position at horizontal distance 4000 m. Comparison of the two gathers shows that the application of equation 2.25 has retrieved correctly all the reflection events and their multiples, including the reflection arrival from the reflector lying below  $\partial\mathbb{D}_m$  with an apex at around 0.95 s and the multiples associated with it. At the same time, it can be observed that the retrieval process has produced additional events, like the ones indicated by

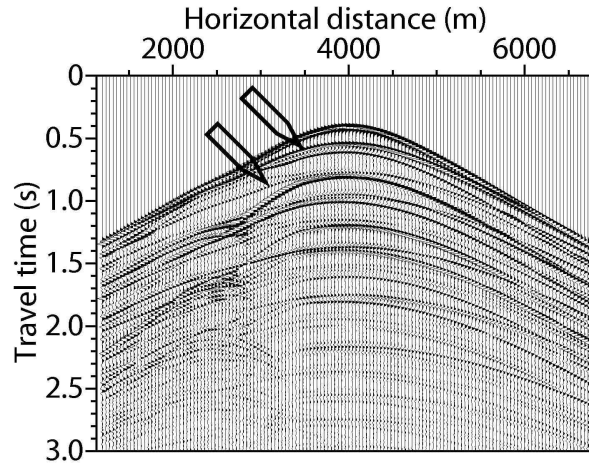


**Figure 3.10:** A transmission gather due to a subsurface source at horizontal distance 4000 m in the presence of a reflector below the source level. The amplitudes are clipped to bring forward later arrivals. The first two arrivals resulting from the presence of the extra reflector are indicated by the pointers.

the black pointers and with apices at around 0.14 s and 0.54 s, which are not present in the numerically modelled reflection gather. These ghost events arise from the presence of the reflector below  $\partial\mathbb{D}_m$  (see equations 2.21 and 2.22).

Consider now a situation where the subsurface sources lie along a sufficiently irregular boundary  $\partial\mathbb{D}_m$ . An example of this is depicted in Figure 3.13, where the subsurface sources are randomly distributed in depth between 700 m and 850 m. At the same time, the horizontal separation of the sources is kept constant at 25 m. As explained at the end of Section 2.1.2, the random-depth distribution of the subsurface sources will cause destructive interference of the ghost events. This can be seen in Figure 3.14. The continuously aligned correlated events, whose troughs at 0.14 s and 0.54 s are clearly visible in the stationary-phase zone in Figure 3.11(a), are quite random in the stationary-phase zone in Figure 3.14(a). At the same time, the correlated event with a trough at 0.95 s is still continuously aligned. Application of the integral in equation 2.25 along the boundary  $\partial\mathbb{D}_m$  results

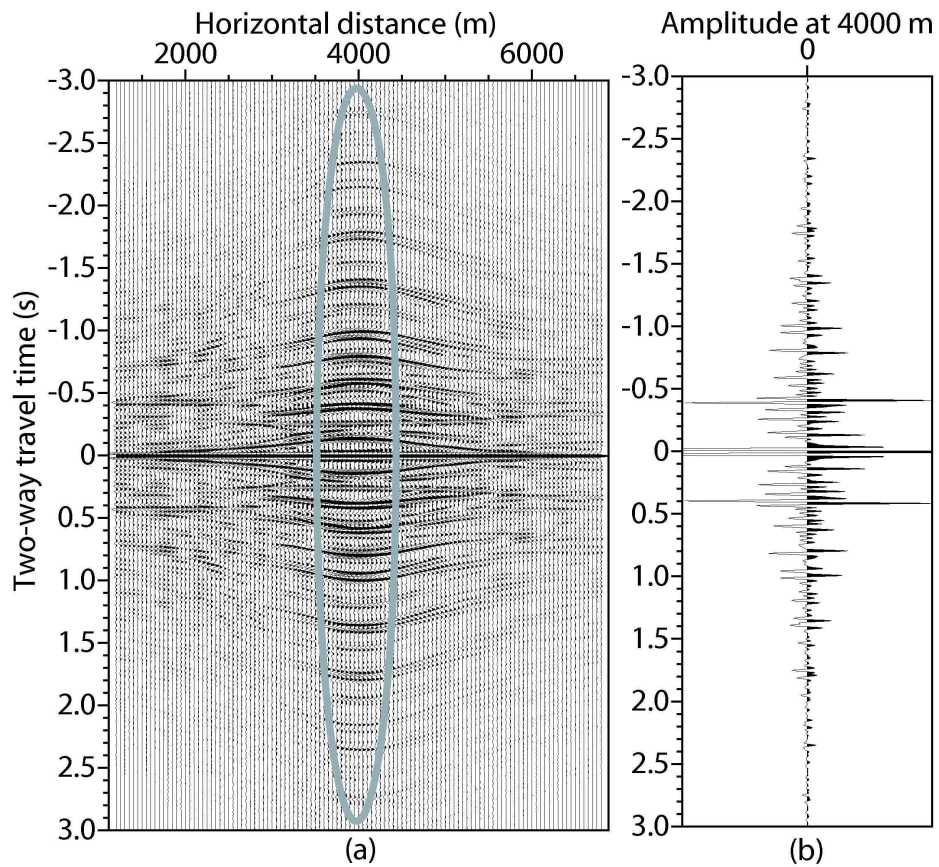


**Figure 3.11:** (a) A correlation panel obtained from the autocorrelation of a master trace at  $x_B = (4000, 0)$  m in the presence of a reflector below the source level. (b) The result from the summation of the traces in (a) along the subsurface source positions. The presence of a reflector below the sources results in the appearance of additional events.

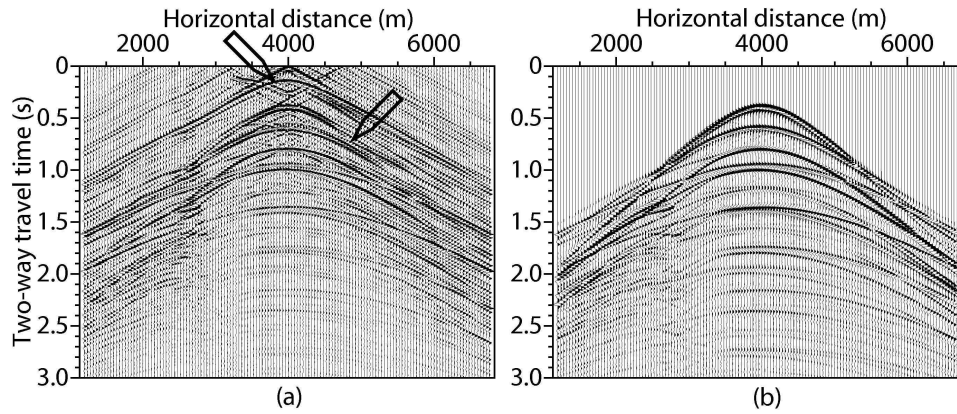


**Figure 3.12:** (a) A retrieved reflection common-source gather for a retrieved surface source position at  $\mathbf{x}_B = (4000, 0)$  m for the subsurface model in Figure 3.9. (b) A reflection common-source gather obtained directly through numerical modelling for the same model. The application of equation 2.25 in the presence of a reflector below the subsurface source level results in a retrieval of ghost events like the ones indicated by the pointers. The ghosts' apices are at 0.14 s and 0.54 s.

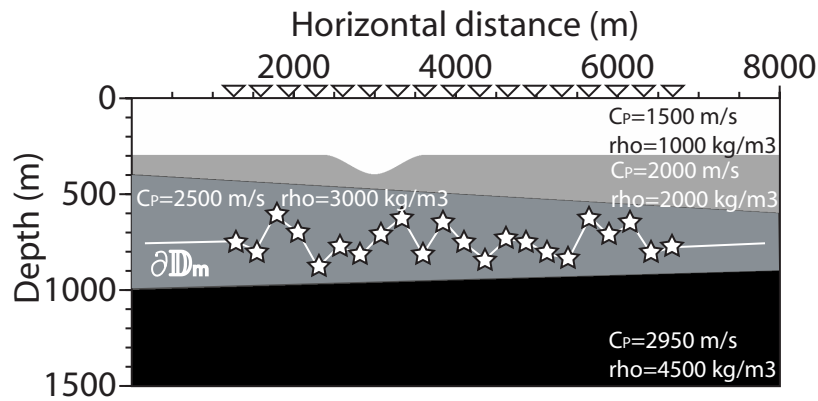


**Figure 3.13:** A subsurface model as in Figure 3.9, but now the subsurface sources are distributed randomly in depth between 700 m and 850 m.



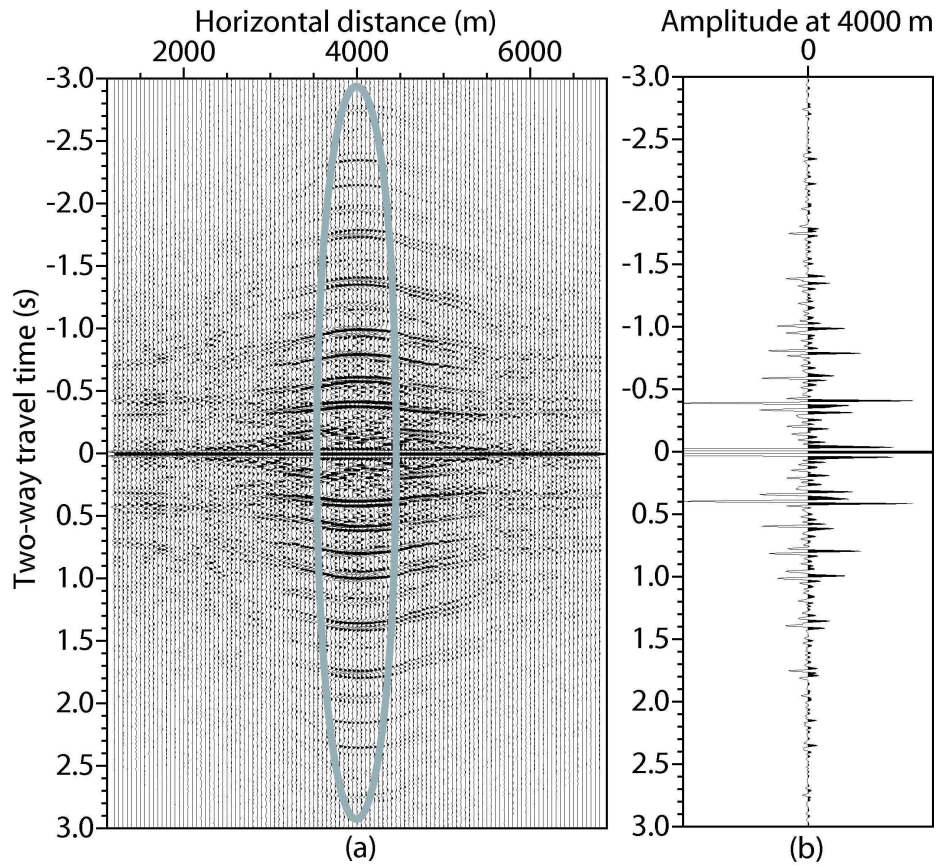


**Figure 3.14:** As in Figure 3.11, but for subsurface sources with random depth distribution. The correlated events that after summation produce ghosts, are here not well-aligned anymore and their summation will result in destructive interference.

in the retrieved reflection zero-offset trace and its time-reversed version, as depicted in Figure 3.14(b), where the retrieved ghost arrivals at 0.14 s and 0.54 s are strongly weakened, while the reflection arrival from the reflector below  $\partial\mathbb{D}_m$  is retrieved correctly. This fact is easier to observe in Figure 3.15 where the retrieved reflection common-source gather (a) for a retrieved surface source position at horizontal distance 4000 m is compared to the reflection gather obtained through direct numerical modelling (b).

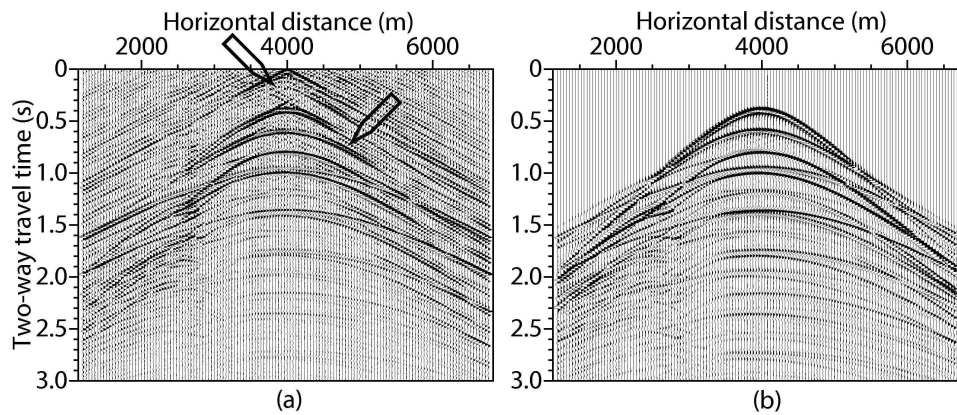


**Figure 3.15:** As in Figure 3.12 but for subsurface sources distributed randomly in depth. The retrieved ghost events from the application of equation 2.25 are strongly weakened (see the pointers).

The SI relation 2.25, as well as the other SI and EMI relations, were derived with the assumption that the medium, where the Green's function is retrieved, is lossless. To investigate the effect of losses on the retrieval results, a subsurface model is used as in Figure 3.13, but now each layer has a loss factor  $Q$ . Two cases are studied. In the first case, the  $Q$ -factor of each layer is taken twice the square root of the propagation velocity, which results in amplitude losses of the propagating waves through each of the layers of 0.00585 dB/m, 0.0038 dB/m, 0.0027 dB/m, and 0.0021 dB/m, from top to bottom respectively. In the second case, the  $Q$ -factor is taken equal to the square root of the propagation velocities and then the respective amplitude

losses in the layers are 0.0117 dB/m, 0.0076 dB/m, 0.0054 dB/m, and 0.0042 dB/m. The source and receiver geometry are the same as in Figure 3.13. Figure 3.16 shows transmission common-source gathers for both cases where both gathers were clipped with the same value as the one used to clip the arrivals in the transmission common-source gather without losses in Figure 3.10 (note that the subsurface sources are not at the same depth). In Figures 3.17 and 3.18 are shown the retrieved reflection common-source gathers (a) from crosscorrelation of transmission recordings in the presence of losses in the medium and the directly modelled reflection gathers in a lossy medium (b) for the two loss cases described above. For a better comparison of the results, the smeared delta function has been muted in the retrieved reflection gathers. Further, both the retrieved and the directly-modelled reflection gathers have been scaled with the maximum value of the trace at horizontal position 4000 m. The comparison of the results in both figures shows that the crosscorrelation process has retrieved the expected reflection arrivals. At the same time, the quality of the retrieved reflection events decreases away from the retrieved source position. It can also be observed that when the amplitude losses in the medium increase, non-physical events, like the events indicated by the black pointers and with apices at around 0.19 s, 0.35 s, 0.55 s, and 0.75 s in panel (a) in Figure 3.18 start appearing in the retrieved result. These loss-related events are present in the retrieved results for both loss cases, but are more visible for the case of stronger losses. The loss-related ghosts arise from events present in the correlation panels. In the correlation panels obtained from modelled without losses, the amplitudes of these events are orders smaller than the events producing the true reflections. In the correlation panels obtained from modelling with losses, the amplitudes of the events, which produce the loss-related ghosts, become of the order of the other events and thus after stacking the correlation panel the result is the appearance of loss-related ghosts.

### ■ 3.1.2 Retrieval of the acoustic reflection response from recordings from white-noise subsurface sources

In the previous section, the SI relation 2.25 was investigated for the retrieval of the reflection response from crosscorrelation of transmission recordings from transient sources. The application of this relation requires separate



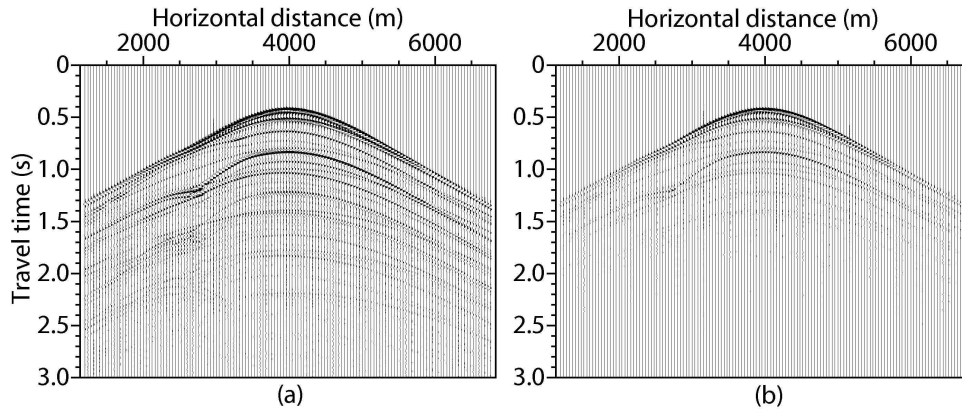


**Figure 3.16:** Transmission common-source gathers for the model in Figure 3.13 for constant losses in the layers with  $Q$ -factors (a) twice the square root of the propagation velocities (78, 90, 100, and 108 from shallow to deep, respectively) and (b) the square root of the propagation velocities (39, 45, 50, and 54 from shallow to deep, respectively).

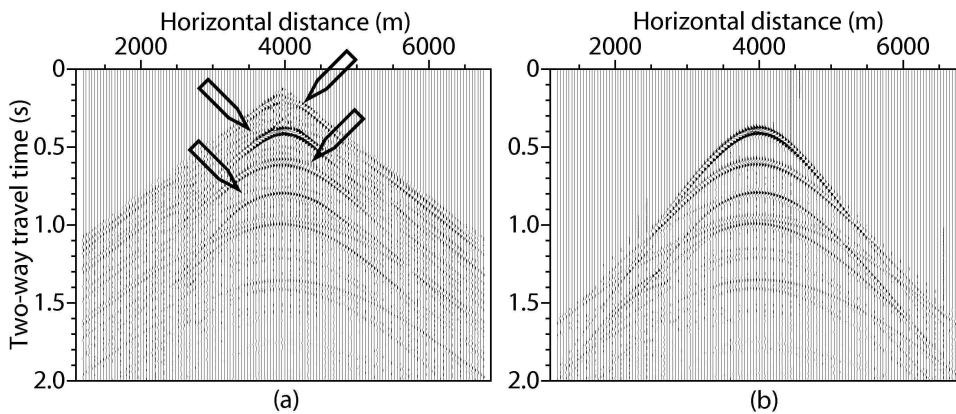


**Figure 3.17:** As in Figure 3.12, but for subsurface sources distributed randomly in depth and for medium with losses where each layer has a constant  $Q$ -factor equal to twice the square root of the propagation velocity. The pointers indicate loss-related ghosts.

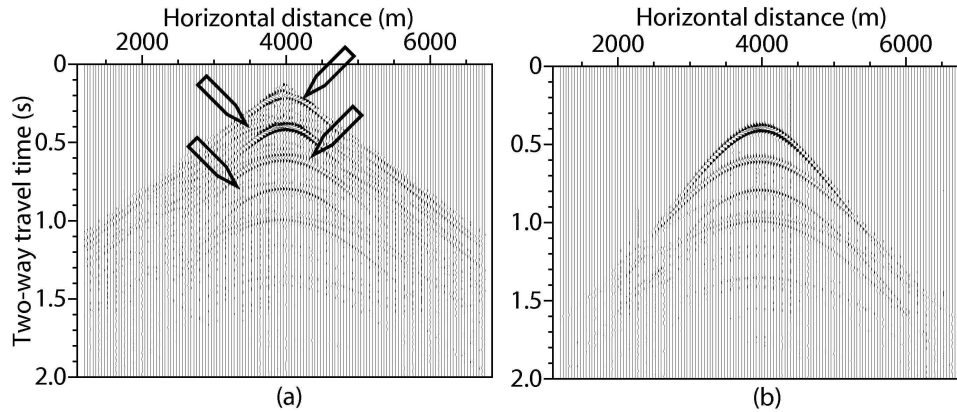


**Figure 3.18:** As in Figure 3.12 but for subsurface sources distributed randomly in depth and for medium with losses where each layer has a constant  $Q$ -factor equal to the square root of the propagation velocity. The pointers indicate loss-related ghosts.

recording of the transmission response from each of the subsurface sources. But it is not always possible and/or feasible to obtain such recordings. For this reason, in this section the SI relation 2.30 is investigated for the retrieval of the reflection response from crosscorrelation of transmission noise recordings. The conclusions from the previous section are valid also for recordings from white-noise subsurface sources. That is why, here the subsurface model and source and receiver geometries from Figure 3.13 are considered where the propagating fields experience no losses in the medium. The subsurface sources are now taken to be white-noise source. Rickett and Claerbout [1996] showed that the signal-to-noise ratio of the retrieved reflections from a horizontally layered medium increases as  $\sqrt{\text{noise-recording length}}$ . As explained in Section 2.1.5, the longer the noise recording, the better fulfilled the assumption of uncorrelated in time noise sources. Furthermore, in practice the noise sources can become active at different times, which means that the longer the recording, the more noise sources will be captured. To make the modelling easier, it is assumed that the noise sources act simultaneously, which reduces the modelling times.

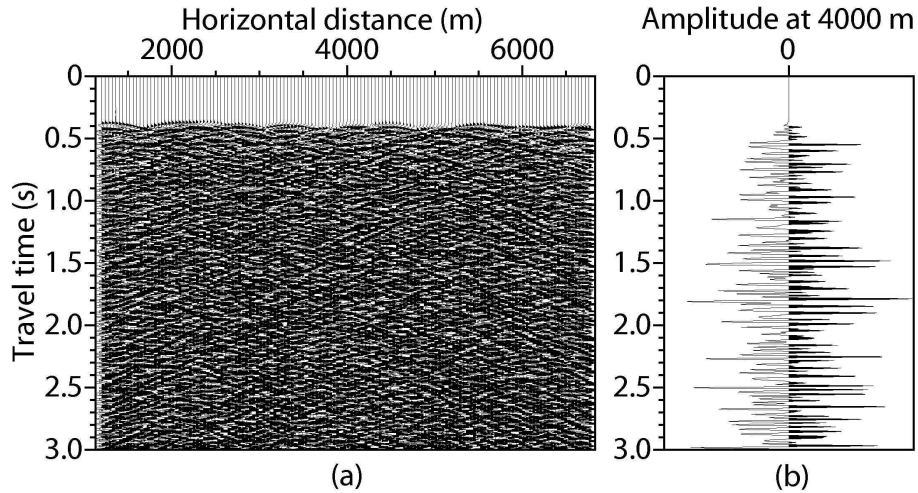


**Figure 3.19:** The first 3 seconds from a transmission gather recorded in the presence of simultaneously acting subsurface white-noise sources. The total length of the record is 66 min. The subsurface model and the source and receiver geometries are the same as in Figure 3.13.

Figure 3.19(a) shows the observed transmission gather along the receiver array when the subsurface white-noise sources have acted simultaneously. The panel shows only the first 3 seconds from a recording that was 66 minutes long. According to equation 2.30, in order to retrieve the reflection response between two receivers, the observed noise traces at these two receivers should be crosscorrelated. Figure 3.19(b) depicts the trace at horizontal distance 4000 m from the gather in 3.19(a). This trace is chosen as a master trace and represents  $p_{obs}(\mathbf{x}_B, t)$ . This trace is crosscorrelated with the transmission gather in Figure 3.19(a), which then represents  $p_{obs}(\mathbf{x}_A, t)$  for a variable  $\mathbf{x}_A$ . The crosscorrelation result, after muting the non-causal part, is shown in Figure 3.20, where it is compared to the directly modelled reflection response. The crosscorrelation has resulted in the retrieval of all reflection events (primary and multiples). Only the later reflection arrivals are not clearly visible as their signal-to-noise ratio is very low. As shown in Draganov and Wapenaar [2004] for a 2D inhomogeneous medium, the

longer the noise recordings the clearer the retrieval of the later reflection arrivals.

The above results were obtained for subsurface noise sources horizontally spaced from each other with less than half the dominant wavelength (25 m) and in such a way that their distribution could be assumed continuous. In practice, especially with noise sources in the subsurface, such an optimal distribution will normally not be the case. The effect on the retrieval results from non-optimal subsurface source distribution is illustrated in Figure 3.21. The retrieved reflection common-source gathers were obtained from crosscorrelation of transmission noise recordings when the subsurface sources were spaced from each other with (a) half the dominant wavelength (repeated from Figure 3.20(a) for convenience), (b) one wavelength, (c) three wavelengths, and (d) twenty wavelengths. It can be observed that the larger the distance between the subsurface sources the lower the quality of the retrieved results. For the extreme source spacing of twenty wavelengths, the reflection events are retrieved incorrectly. This result can be explained by considering the situation with transient sources in the subsurface. The re-

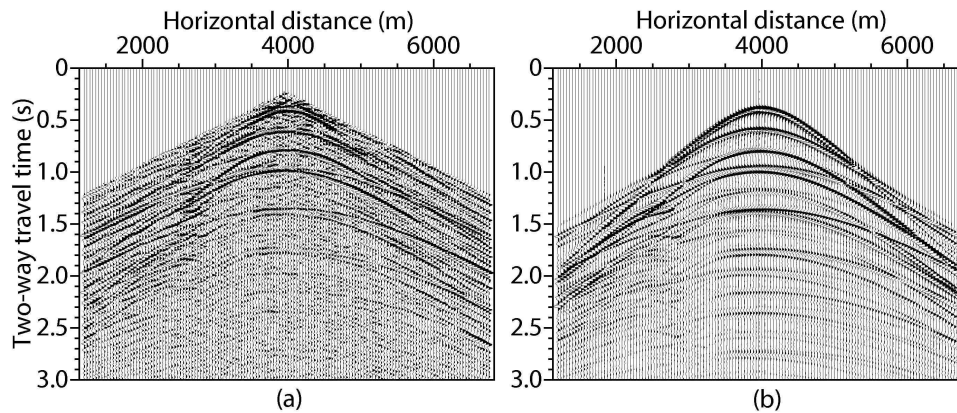


**Figure 3.20:** (a) A retrieved reflection common-source gather for a retrieved surface source position at  $\mathbf{x}_B = (4000, 0)$  m from the crosscorrelation of 66-minute-long transmission recordings from white-noise sources. (b) A reflection common-source gather obtained directly through numerical modelling.



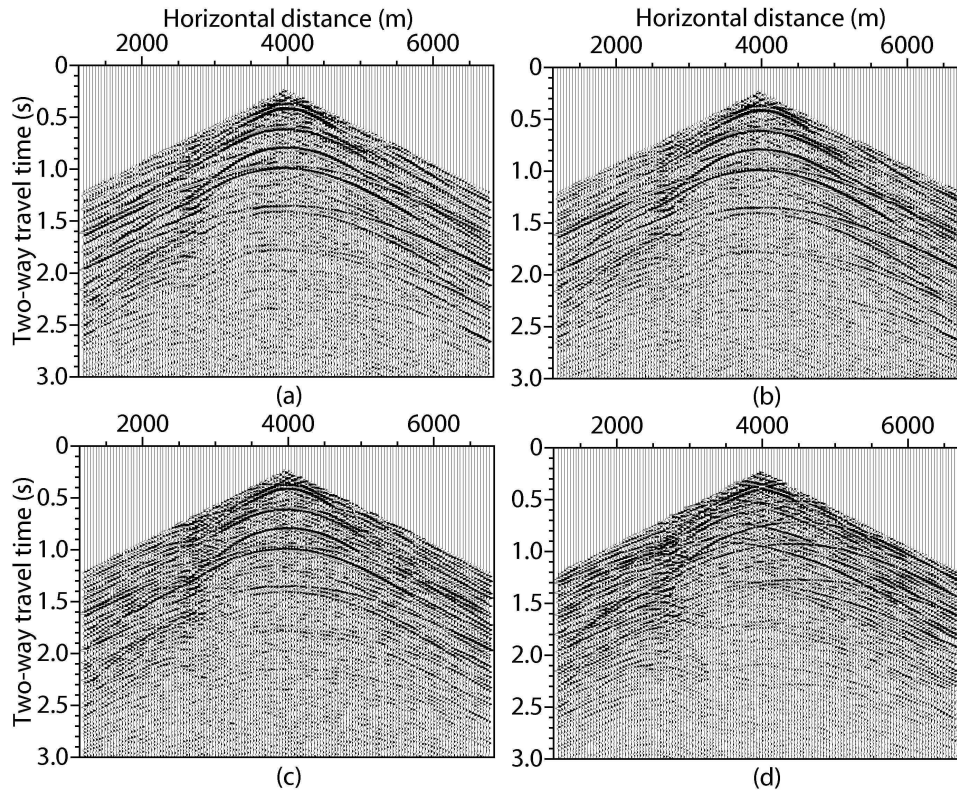


**Figure 3.21:** A retrieved reflection common-source gather for a retrieved surface source position at  $\mathbf{x}_B = (4000, 0)$  m when the white-noise sources in the subsurface are (a) spaced half the dominant wavelength or 25 m apart, (b) one wavelength or 50 m apart, (c) three wavelengths or 150 m apart, and (d) twenty wavelengths or 1000 m apart.

retrieved events result from the constructive interference of wavelets in the stationary-phase region during integration over the boundary  $\partial\mathbb{D}_m$  (see Figure 3.14 for example). This integration is intrinsically present in relation 2.30 as can be seen from equations 2.27-2.29. When the spacing between the sources increases, there are less constructively interfering wavelets in the stationary-phase region and the result is incomplete retrieval of events or even

that the retrieval of events is incorrect.

Even though some reflections can be incompletely or incorrectly retrieved, the strength of the SI method is that the retrieval process can be applied at all receiver positions, creating in this way redundant reflection information. This reflection information can further be used in a migration procedure. The migration process will (at least partly) compensate for the incomplete retrieval of the reflections [Wapenaar et al., 2004a]. This can be understood by considering that the migration process incorporates an integral over the receiver positions, which would "capture" stationary-phase points, that were missed in the retrieval process. This is depicted in Figure 3.22, which shows the migration results from retrieved reflection gathers in the presence of subsurface white-noise sources with spacing of (a) half a wavelength, (b) one wavelength, (c) three wavelengths, and (d) twenty wavelengths, respec-

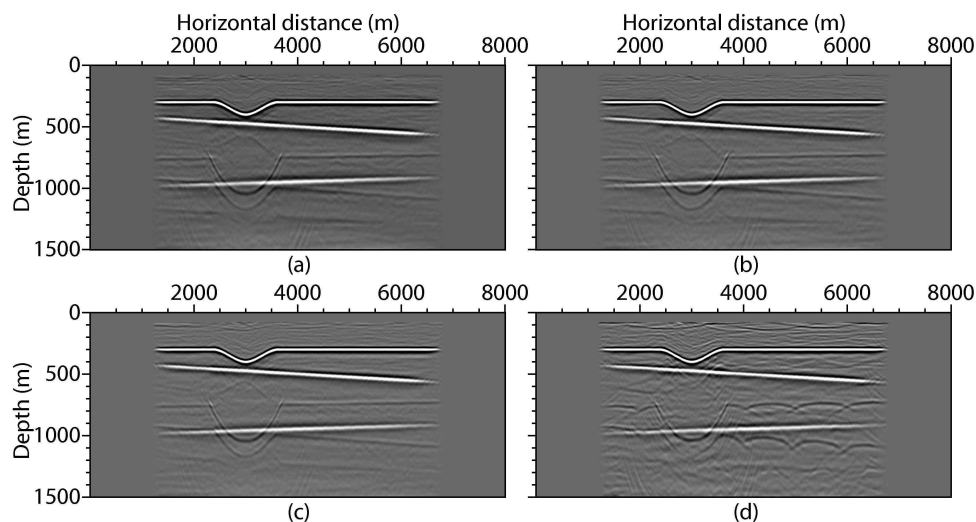


**Figure 3.22:** Results from a pre-stack depth migration algorithm applied to retrieved reflection data when the subsurface noise sources had been separated with (a) half the dominant wavelength or 25 m, (b) one wavelength or 50 m, (c) three wavelengths or 150 m, and (d) twenty wavelengths or 1000 m.

tively. The images were obtained using shot-profile pre-stack depth migration [Claerbout, 1971; Berkhout, 1982]. The migration was performed with the exact velocity model to emphasize the characteristics of the obtained depth images. For the same reason, no multiple elimination scheme was applied. The images in Figure 3.22 clearly show that the reflector boundaries between the different layers have been correctly imaged, even for the extreme case of subsurface noise-source spacing of twenty wavelengths. In practice the migration is performed with approximate velocity models. In such cases, the migration of retrieved reflection gathers behaves in a similar way as the migration of conventional reflection gathers. Figure 3.23(a) shows the approximate velocity model used to migrate the retrieved reflection results from the crosscorrelation of transmission recordings for a subsurface noise-source spacing of twenty wavelengths. The velocity model was built presuming that the velocity of the first layer is known exactly, while the velocities of the deeper layers are 10 % lower than the velocity values used for numerical modelling. The layer boundaries are taken at incorrect depths and assumed horizontal. The migration result is shown in Figure 3.23(b). It can be seen that the layer boundaries are imaged, but, as expected, the boundaries are at wrong depths and with artefacts.

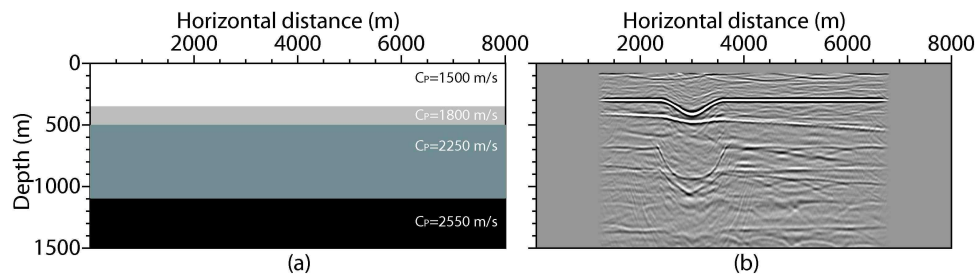


**Figure 3.23:** (a) Approximate subsurface velocity model. (b) Result from a pre-stack depth migration using the velocity model in (a) applied to retrieved reflection data when the subsurface noise sources had been twenty wavelengths (1000 m) apart.

## 3.2 Retrieval of the elastodynamic reflection response

In Sections 2.1.6-2.1.9 SI relations were derived for the retrieval of new elastodynamic seismic recordings from the crosscorrelation of existing recordings. Just like in Section 3.1, here are shown examples of the retrieval of the reflection response from the crosscorrelation of observed transmission responses from sources deep in the subsurface. The absence of sources close to the surface will result in the suppression (or even absence) of surface waves in the retrieved results. With the help of 2D examples, the elastodynamic SI relations 2.54 and 2.59 are investigated in the presence of transient and noise sources in the subsurface, respectively. These examples were obtained from transmission recordings at the free surface generated with a finite-element modelling scheme [Zhang and Verschuur, 2002].

### ■ 3.2.1 Retrieval of the elastodynamic reflection response from recordings from transient subsurface sources

To investigate the SI relation 2.54, a lossless 2D elastic subsurface model was used (see Figure 3.24). Along the free surface, there are seismic receivers, represented by the triangles, which record the particle velocity in three directions. The subsurface consists of a homogeneous layer with two bodies in the form of lenses. The receiver array extends from horizontal distance 2100 m until horizontal distance 5700 m with receiver spacing of 15 m. Because the medium is bounded from above by a free surface, to retrieve reflection arrivals, one needs recordings from sources along the subsurface part  $\partial\mathbb{D}_m$  of the boundary  $\partial\mathbb{D}$  (see equation 2.54 and the explanation in Section 2.1.7). In Figure 3.24 the boundary  $\partial\mathbb{D}_m$  is a horizontal line at depth 756 m. The subsurface sources lie in the horizontal direction between 2100 m and 5796 m with a spacing of 21 m. The source wavelet has the form of a first derivative of a Gaussian function with a peak frequency of 20 Hz. Thus, the source spacing is less than half the dominant wavelength of the lowest propagation velocity for shear waves.

Equation 2.54 was derived for the general 3D case. As here a 2D medium is considered, the vibrations in the direction of axis  $x_2$  decouple from the vibrations in the direction of the axes  $x_1$  and  $x_3$ . This means that in the SI relation 2.54 the subscripts  $p$  and  $q$  take on the values 1 and 3, which denote



horizontal and vertical direction, respectively. The subscript  $K$  can take the values 0 and 2, meaning that there can be subsurface sources of P-waves and SV-waves, respectively. This means that in the right-hand side of the equation, there will be a summation of two integrals – an integral over P-wave sources and an integral over SV-wave sources. Note that the P- and the SV-wave sources lie at the same subsurface positions.

If a subsurface source is set off, then at the surface the elastodynamic transmission response is observed. Figure 3.25 shows the transmission common-source gathers observed at the surface for a subsurface source at horizontal distance 3900 m. The panels (a) and (b) show the observed vertical and horizontal component, respectively, of the particle velocity for a subsurface P-wave source. The panels (c) and (d) show the observed particle velocity in the vertical and in the horizontal direction, respectively, for a subsurface SV-wave source.

To retrieve an observed vertical particle velocity reflection recording at a

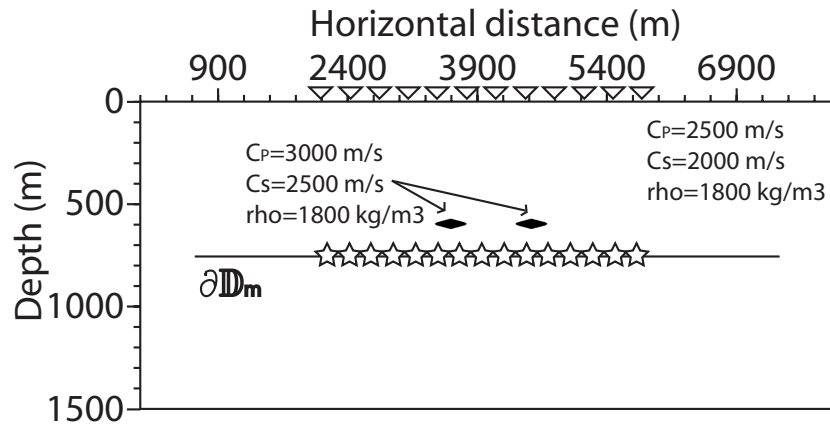


**Figure 3.24:** A lossless 2D elastic subsurface model. There are 241 receivers (represented by the triangles) at the free surface starting from 2100 m until 5700 m, with spacing 15 m. There are 172 transient sources (the stars) in the subsurface along a boundary  $\partial\mathbb{D}_m$ . The subsurface sources are placed every 21 m starting from 2100 m and going until 5691 m.

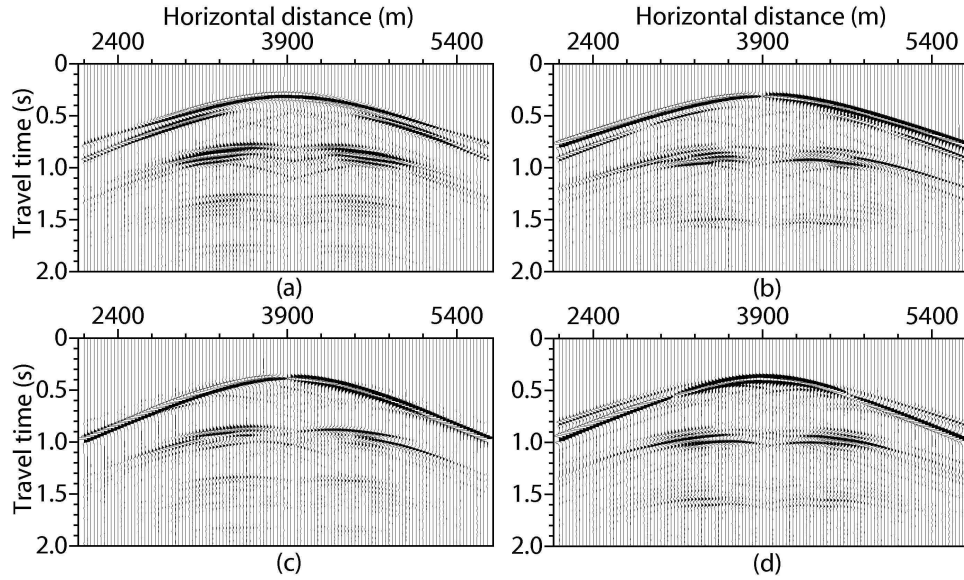


**Figure 3.25:** Transmission common-source gathers observed at the surface for a subsurface source at horizontal distance 3900 m. (a) Observed vertical particle velocity  $v_{3,0}^{obs}(\mathbf{x}_A, \mathbf{x}, t)$  due to a P-wave source. (b) Observed horizontal particle velocity  $v_{3,0}^{obs}(\mathbf{x}_A, \mathbf{x}, t)$  due to a P-wave source. (c) Observed vertical particle velocity  $v_{1,0}^{obs}(\mathbf{x}_A, \mathbf{x}, t)$  due to a SV-wave source. (d) Observed horizontal particle velocity  $v_{1,2}^{obs}(\mathbf{x}_A, \mathbf{x}, t)$  due to a SV-wave source. The amplitudes are clipped to bring forward later arrivals.

receiver location due to a surface source acting in the vertical direction at another receiver location, for example at horizontal distance 3900 m, the following is done. A master trace, representing  $v_{3,0}^{obs}(\mathbf{x}_B, \mathbf{x}, t)$  at location 3900 m is extracted from the transmission gather for a P-wave subsurface source in Figure 3.25(a). This trace is correlated with the same gather, where the gather represents  $v_{3,0}^{obs}(\mathbf{x}_A, \mathbf{x}, t)$  for a variable  $\mathbf{x}_A$ , producing a P-source correlation panel for this source position. The above two steps are repeated for all subsurface P-wave source positions. This is followed by summation of all the P-source correlation panels (the integral over the P-wave sources in relation 2.54). The result is shown in Figure 3.26(a). The same procedure is

followed also for the correlation of the transmission recordings from the SV-wave subsurface sources, where the subscript 0 is replaced by the subscript 2, see Figure 3.26(b). Note that due to the absence of shallow subsurface sources, in neither of the two panels surface-wave events can be observed. Following the SI relation 2.54, the last step to be done to retrieve the reflection response is to sum the panels in (a) and (b) in Figure 3.26. The result, shown in Figure 3.27(a), represents the retrieved vertical particle velocity due to a vertical force source at horizontal position 3900 m after muting the anti-causal part and the smeared delta function.

To retrieve the horizontal component of the observed particle velocity due to a surface source at horizontal distance 3900 m acting in the vertical direction, a procedure can be followed similar to the one for the retrieval of the vertical component of the particle velocity. Here, though, for a P-wave sub-

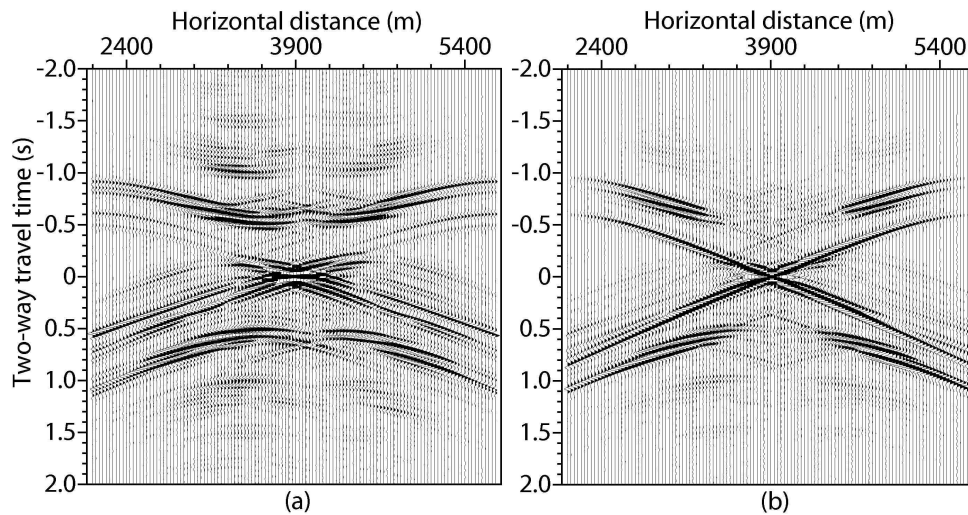


**Figure 3.26:** (a) Result from the correlation with a master trace at 3900 m after integration of P-source correlation panels. (b) Result from the correlation with a master trace at 3900 m after integration of SV-source correlation panels. The amplitudes are clipped to bring forward later arrivals.

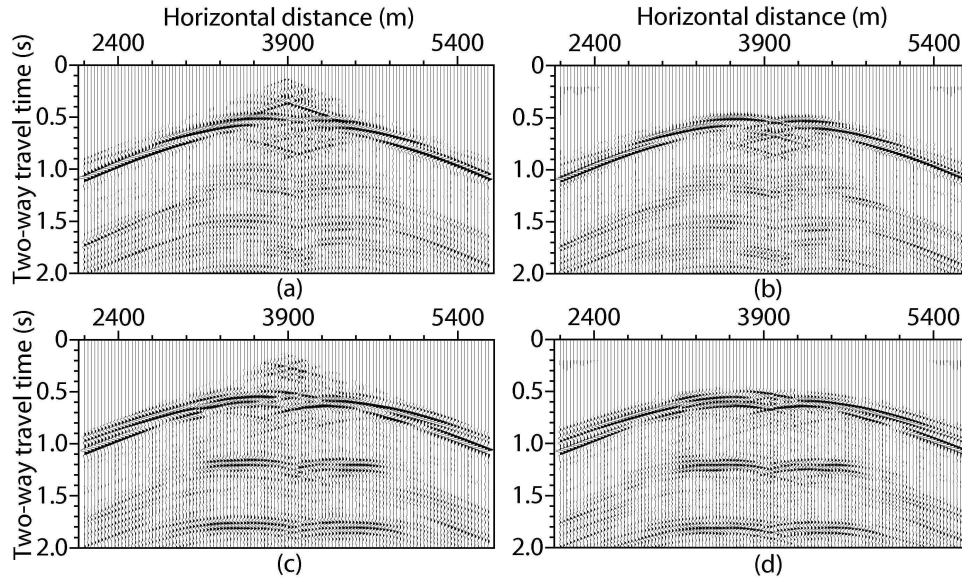


**Figure 3.27:** (a) A retrieved reflection common-source gather representing observed vertical particle velocity due to a retrieved surface vertical force source at position  $\mathbf{x}_B = (3900, 0)$  m. (b) Vertical particle velocity reflection common-source gather obtained directly through numerical modelling. The surface-wave arrivals have been removed. (c) Same as in (a) but for observed horizontal particle velocity. (d) Same as in (b) but for horizontal particle velocity. Gaining was applied to all gathers to amplify later arrivals.

surface source a master trace, representing  $v_{3,0}^{obs}(\mathbf{x}_B, \mathbf{x}, t)$ , is extracted from the transmission gather in Figure 3.25(a) and is correlated with the transmission gather in Figure 3.25(b), representing  $v_{1,0}^{obs}(\mathbf{x}_A, \mathbf{x}, t)$  for changing  $\mathbf{x}_A$ . For SV-wave subsurface sources, a master trace ( $v_{3,2}^{obs}(\mathbf{x}_B, \mathbf{x}, t)$ ) is extracted from the transmission gather in Figure 3.25(c) and is correlated with the transmission gather in Figure 3.25(d) ( $v_{1,2}^{obs}(\mathbf{x}_A, \mathbf{x}, t)$ ). The above steps are repeated for all subsurface sources, followed by summation over the subsurface source positions and source types. The obtained final result is shown in Figure 3.27(c).

The comparison of the retrieved results with the directly modelled particle velocities due to a vertical force source (Figure 3.27(b) and 3.27(d)) shows that all reflected arrivals (direct, multiples, conversions) have been correctly retrieved. The crossing linear events just above the first reflection arrival in (a) and (c) result from the limited aperture of the subsurface source array. This can be demonstrated by extending the subsurface source array.

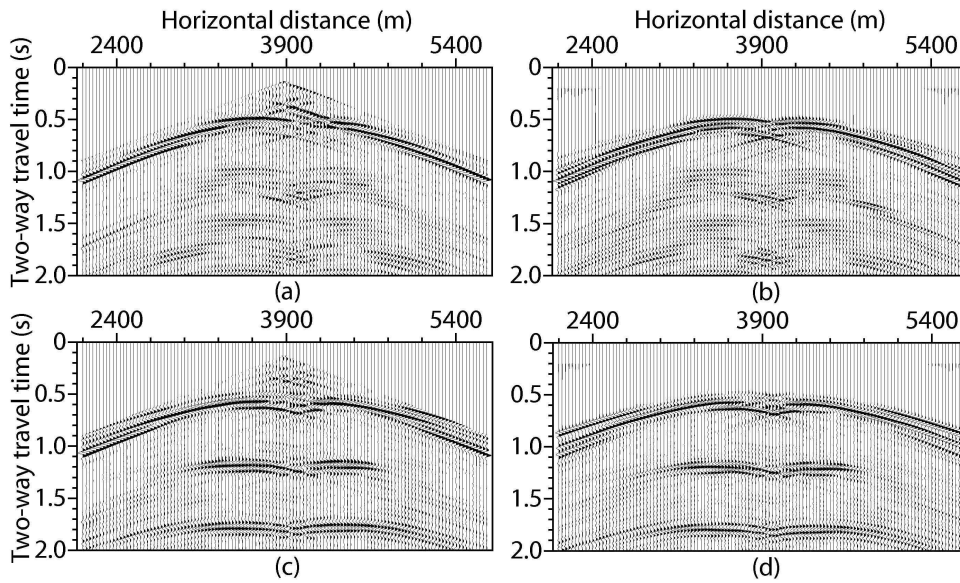


**Figure 3.28:** As in Figure 3.27 but for surface force source acting in the horizontal direction.

In Figure 3.28 similar results are shown, but this time for a force source acting in the horizontal direction at horizontal position 3900 m. The gathers in (a) and (c) were obtained following the procedures described above, but this time the master traces were extracted from the transmission gathers in Figures 3.25(b) and 3.25(d).

In the model in Figure 3.24 the medium below the boundary  $\partial\mathbb{D}_m$  was taken to be homogeneous. When this is not the case, the crosscorrelation process



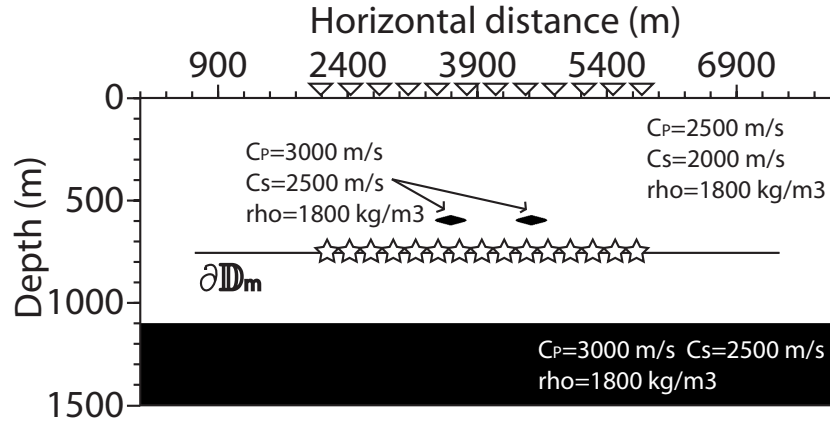


**Figure 3.29:** A subsurface model with source and receiver geometries as in Figure 3.24, but with an extra reflector below  $\partial\mathbb{D}_m$ .

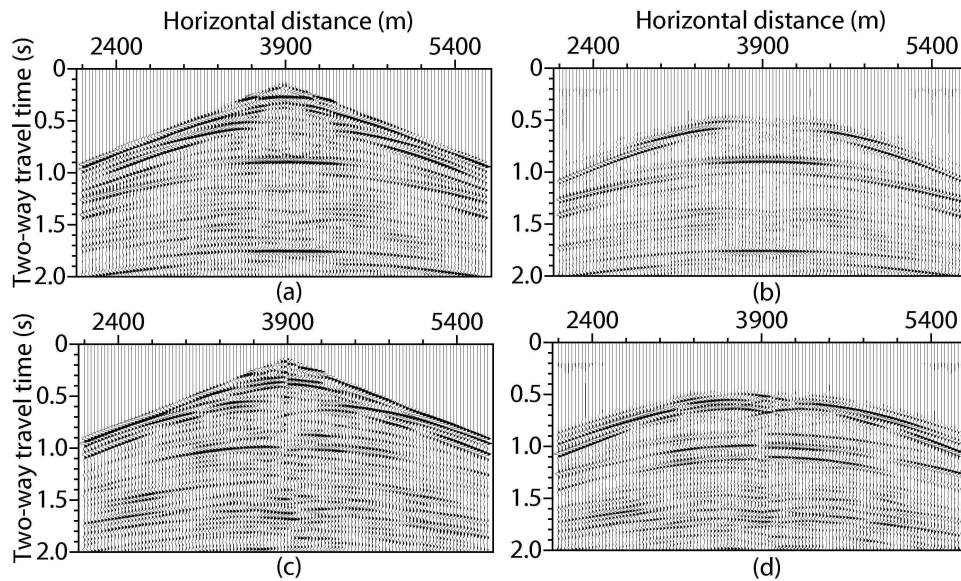


**Figure 3.30:** Reflection common-source gathers for the model in Figure 3.29. (a) Retrieved vertical particle velocity due to a retrieved surface vertical force source at position  $\mathbf{x}_B = (3900, 0)$  m. (b) Vertical particle velocity obtained directly through numerical modelling. The surface-wave arrivals have been removed. (c) Same as in (a) but for observed horizontal particle velocity. (d) Same as in (b) but for horizontal particle velocity. Gaining was applied to all gathers to amplify later arrivals.

will result in the retrieval of ghost events, see equations 2.49 and 2.50. This is illustrated for the subsurface model in Figure 3.29 in which there is an extra reflector below the boundary  $\partial\mathbb{D}_m$ . Using this model, transmission gathers are generated from subsurface P-wave and SV-wave sources. These transmission gathers are used to retrieve reflection common-source gathers in the same way as it was described above. In Figure 3.30 the comparison is shown between retrieved reflection gathers and reflection gathers obtained directly through numerical modelling of observed particle velocities when a surface force source at 3900 m would be acting in the vertical direction. It can be observed that the crosscorrelation process has produced additional events in (a) and (c) that are not present in the directly modelled reflection gathers in (b) and (d). Examples of such ghosts are the retrieved events before the first reflection arrivals, the events in (a) with apices at around 0.6 s and 1.15 s, and the event in (c) with an apex around 1.3 s.

Consider now a model, as depicted in Figure 3.31, where the subsurface sources lie over a sufficiently irregular boundary  $\partial\mathbb{D}_m$ . The subsurface source positions are chosen to be random in the vertical direction, while in the horizontal direction their spacing is kept regular at 21 m. There is an extra reflector below the source boundary. The retrieved reflection common-source gathers for this model for a vertically acting surface source at position 3900 m are shown in panels (a) and (c) of Figure 3.32. Comparing the retrieved results to the reflection gathers obtained directly through numerical modelling (panels (b) and (d) of Figure 3.32), it is observed that the ghost events are now strongly weakened.

### ■ 3.2.2 Retrieval of the elastodynamic reflection response from recordings from white-noise subsurface sources

Consider again the subsurface model from Figure 3.31. The receiver and subsurface-source geometries are kept the same. But this time it is assumed that no separate recordings from the subsurface sources are possible. This means that to retrieve the reflection response, one has to make use of SI relation 2.59.

Figure 3.33(a) shows the first two seconds of the vertical particle velocity recording, which was 35 minutes long, in the presence of white-noise sources in the subsurface. This modelled transmission recording was ob-

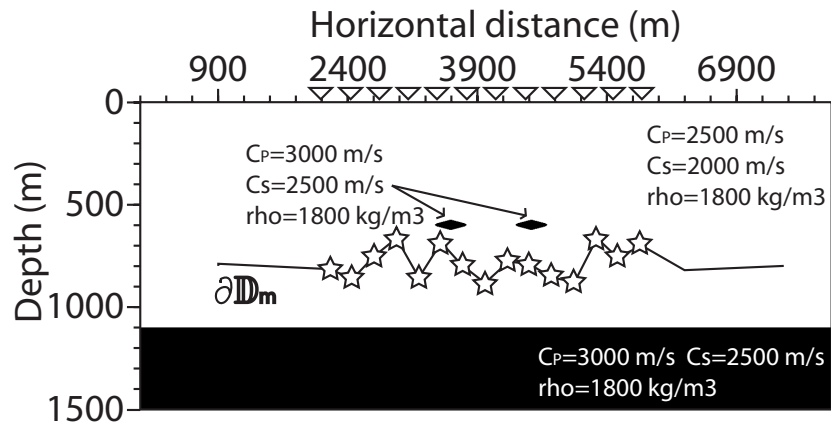


**Figure 3.31:** A subsurface model with source and receiver geometries as in Figure 3.24, but with an extra reflector below  $\partial\mathbb{D}_m$ . The subsurface source positions are randomly distributed in depth.

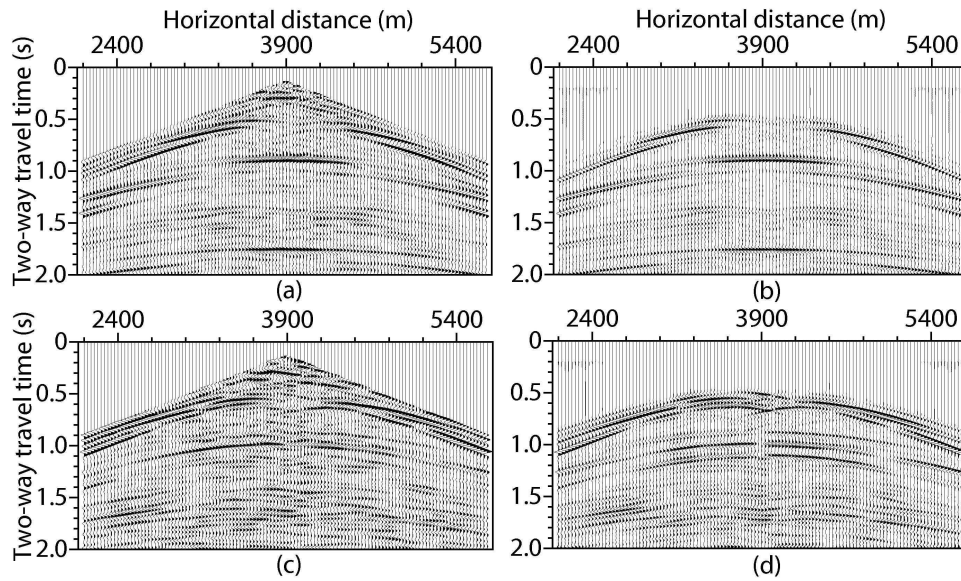


**Figure 3.32:** As in Figure 3.30, but for the model in Figure 3.31.



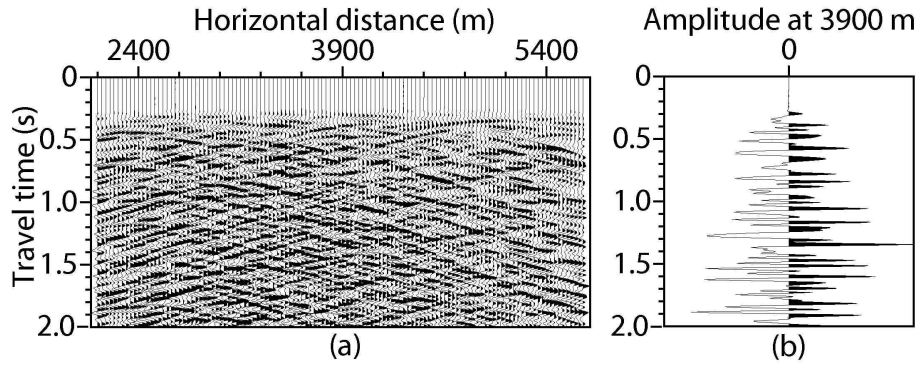


**Figure 3.33:** The first 2 seconds from a transmission gather recorded in the presence of simultaneously acting subsurface P-wave and SV-wave white-noise sources. The total length of the record is 35 min. The subsurface model and the source and receiver geometries are the same as in Figure 3.31.

tained by placing at the subsurface source positions first P-wave white-noise sources and setting them off simultaneously. This recording was then summed with a transmission recording obtained from simultaneously acting SV-wave white-noise sources, placed at the same positions as the P-wave sources. Using equation 2.59, in order to retrieve the reflection response, observed in the vertical direction, as if from a surface force source acting in the vertical direction, the following is done. A receiver position is chosen, in this case 3900 m, where the surface source position will be retrieved. A master trace, as shown in Figure 3.33(b) and representing  $v_3^{obs}(\mathbf{x}_B, t)$ , is extracted at that position from the transmission gather in Figure 3.33(a) and crosscorrelated with all the traces in the gather. The transmission gather represents  $v_3^{obs}(\mathbf{x}_A, t)$  for a variable  $\mathbf{x}_A$ . The retrieved result, after muting the anticausal part and the smeared delta function, is shown in Figure 3.34(a). To retrieve the horizontal particle velocity component for a reflection recording due to a surface vertical force source, the master trace in Figure 3.33(b) is crosscorrelated with the horizontal component of the particle velocity transmission gather from the subsurface noise sources, i.e.,  $v_1^{obs}(\mathbf{x}_A, t)$ . Figure 3.34(c) depicts the retrieved result. Panels (b) and (d) in the same figure

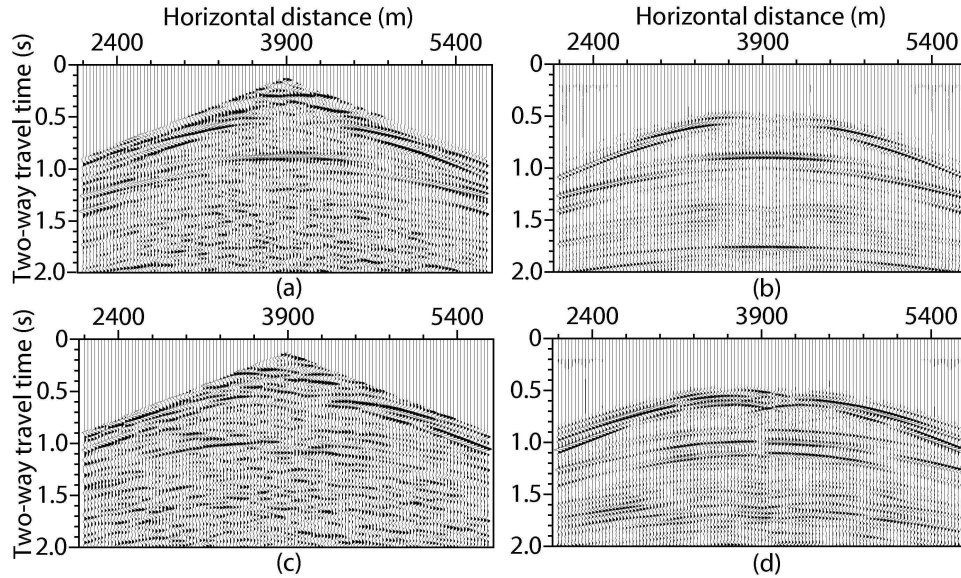


**Figure 3.34:** Reflection common-source gathers for the model in Figure 3.31, but for white-noise sources in the subsurface. (a) Retrieved vertical particle velocity due to a retrieved surface vertical force source at position  $\mathbf{x}_B = (3900, 0)$  m. (b) Vertical particle velocity obtained directly through numerical modelling. The surface-wave arrivals have been removed. (c) Same as in (a) but for observed horizontal particle velocity. (d) Same as in (b) but for horizontal particle velocity. Gaining was applied to all gathers to amplify later arrivals.

show the vertical and the horizontal particle velocity reflection common-source gathers, respectively, obtained through direct numerical modelling for a surface vertical force source at 3900 m horizontal distance. The comparison of the gathers in (a) and (c) to the gathers in (b) and (d), respectively, shows that the application of relation 2.59 has correctly retrieved the expected reflection arrivals, though the later arrivals are not clearly visible as their signal-to-noise ratio is low.

To retrieve the vertical and horizontal particle velocity components as if from a surface force source acting in the horizontal direction, a similar procedure is followed as above, but the master trace is extracted from the horizontal

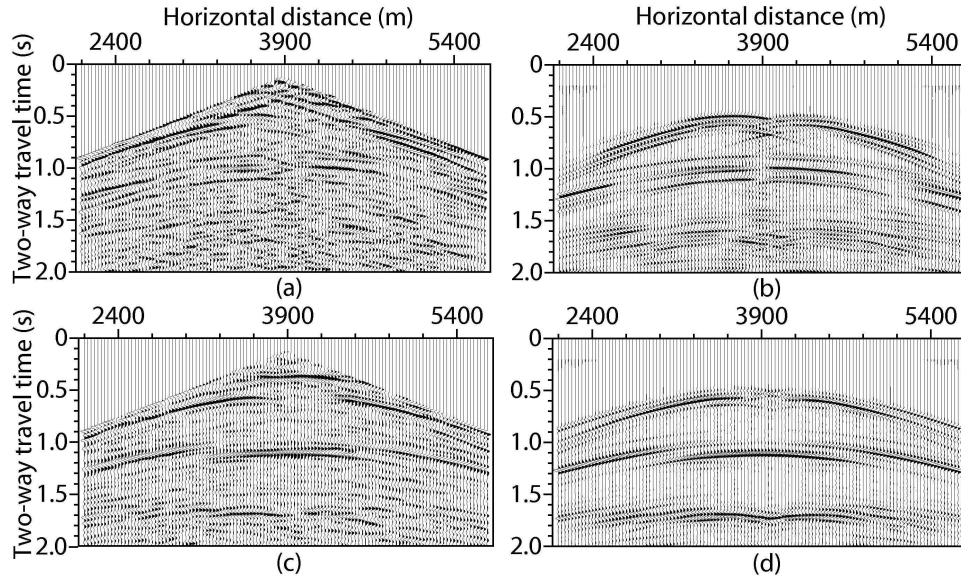


**Figure 3.35:** As in Figure 3.34, but for a surface force source acting in the horizontal direction.

component of the observed particle velocity transmission gather. The retrieved and the directly modelled results are shown in Figure 3.35.

### 3.3 Retrieval of the electromagnetic reflection response

Until now, in this chapter examples were given of the retrieval of the reflection response at the earth's surface, which for the seismic case is a free surface, i.e., a perfect reflector. In the electromagnetic case, the earth's surface is not a perfect reflector anymore. This means that to retrieve the reflection response, for example for Ground Penetrating Radar (GPR) applications, one needs to crosscorrelate recordings from sources below as well as above the observation points. Figure 3.36 shows a 2D example model, which was used to simulate electromagnetic wavefields for GPR application. It consists

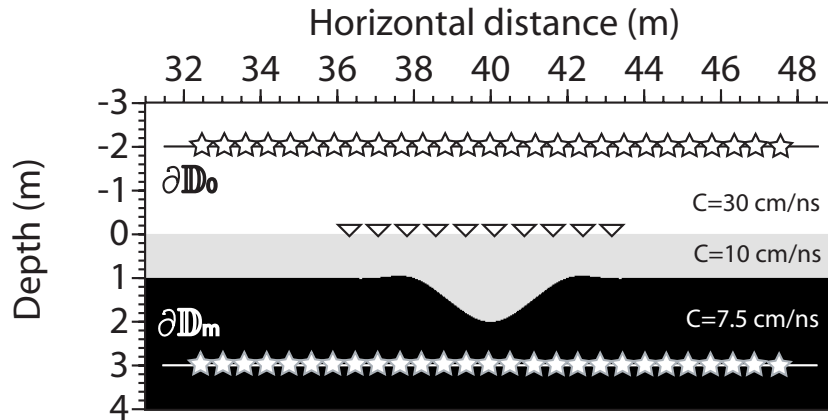


**Figure 3.36:** A lossless 2D model. There are 64 receiver antennae, represented by the triangles, at the earth's surface from horizontal distance 36.85 m until 43.15 m, with spacing of 10 cm. There are two source antenna arrays, each of 151 sources, the stars. The source antennae lie in the subsurface along the boundary  $\partial\mathbb{D}_m$  and in the air 2 m above the receivers along the boundary  $\partial\mathbb{D}_0$ . The source antennae are placed every 10 cm starting from 32.5 m and going until 47.5 m.

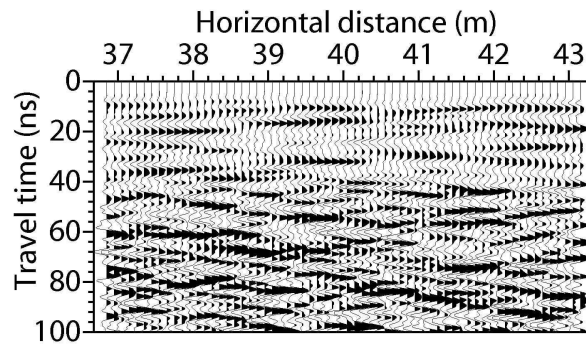


**Figure 3.37:** The first 100 ns from a transmission gather recorded in the presence of simultaneously acting white-noise electromagnetic sources below as well as above the receivers. The total length of the record is 120  $\mu\text{s}$ .

of two subsurface layers separated by a syncline-shaped boundary. The relative electric permittivities of the two layers are 9 and 16, respectively. At the surface, at zero depth of the model, a receiver antenna array is placed consisting of 64 antennae separated by 10 cm. The receiver antennae record the propagating wavefields from two source antenna arrays, one of which is in the subsurface and one in the air above the receivers. Each source array consists of 151 antennae spaced 10 cm apart starting from 32.5 m and going until 47.5 m. The sources are temporally mutually uncorrelated, emit simultaneously and are active for  $120 \mu\text{s}$ . In a usual GPR acquisition system, two parallel broad-side antennae are used, which means that for a 2D medium transverse-electric modes are emitted and recorded. Figure 3.37 shows the observed first 100 ns from the total transmission gather recording. First, at around 7 ns, the wavefields arrive from the sources in the air. At around 34 ns also the wavefields from the subsurface sources start arriving.

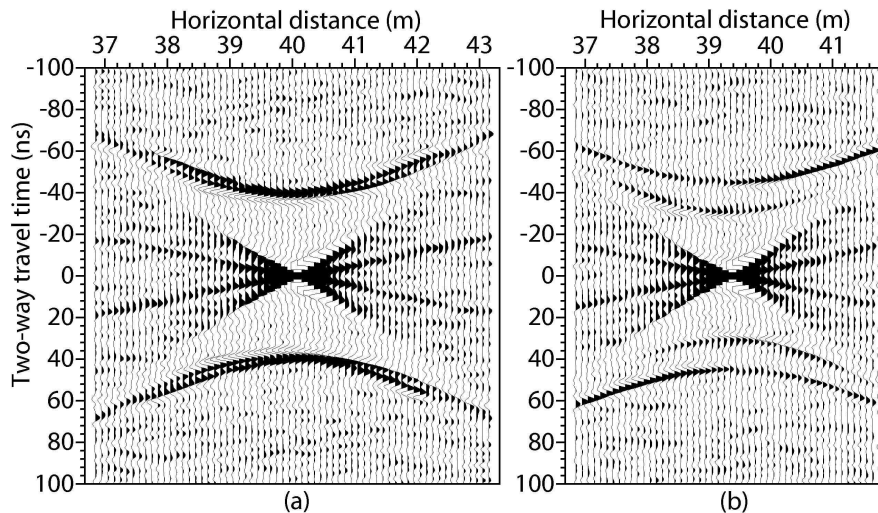


**Figure 3.38:** Causal and anti-causal retrieved common-midpoint gathers for (a) a midpoint at 40 m and (b) a midpoint at 39.3 m. The source-receiver antennae separation step is 20 cm.

With the help of equation 2.82, by choosing a point along the receiver gather,



extracting and correlating traces which lie at an equal distance from this point, one can retrieve a common-midpoint gather. Figures 3.38(a) and 3.38(b) show examples of the causal and anti-causal retrieved common-midpoint gathers with a midpoint at 40 m and 39.30 m, respectively. The source-receiver antennae separation increases with 20 cm. In (a), the source-receiver separation starts at 10 cm and increases until 6.3 m. In (b), the source-receiver separation starts at 10 cm and increases until 4.9 m. It can be observed that while for the gather in (a) the causal and the anti-causal parts of the retrieved results are nearly symmetric, for the gather in (b) the causal and the anti-causal parts are not symmetric. Due to the relatively longer source

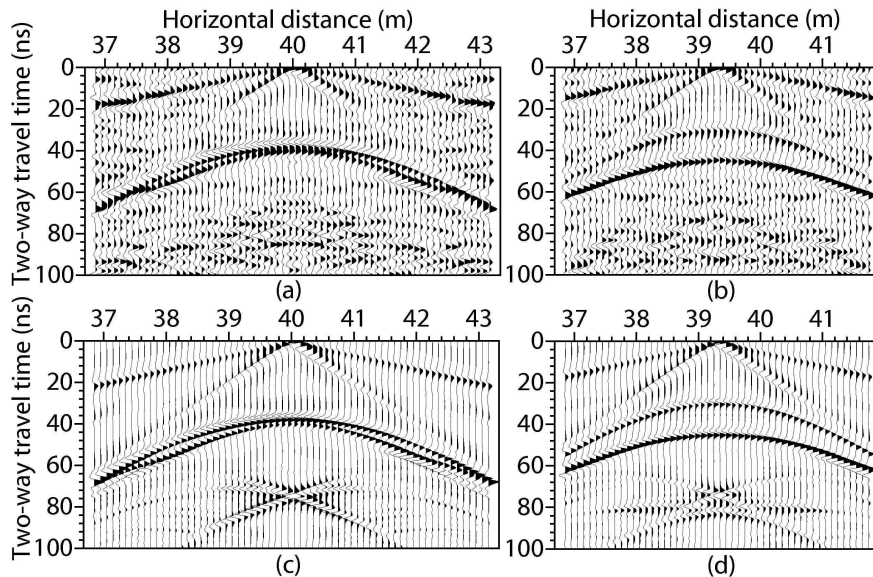


**Figure 3.39:** Common-midpoint gathers. The source-receiver antennae separation step is 20 cm. (a) Retrieved gather for a midpoint at 40 m. (b) Retrieved gather for a midpoint at 39.3 m. (c) Directly modelled gather for a midpoint at 40 m. (d) Directly modelled gather for a midpoint at 39.3 m. The retrieved results were obtained for crosscorrelation of recordings from noise sources above as well as below the receiver antennae.

antennae arrays, there is no curling at the ends of the retrieved reflection hyperbolae and it will be very beneficial to sum the causal and the anti-causal parts. Figure 3.39 shows the comparison between the retrieved common-midpoint gathers, after summing the causal and the anti-causal parts, and the directly modelled common-midpoint gathers for midpoint at 40 m for (a) and (c) and for midpoint at 39.3 m for (b) and (d). For both common-midpoint gathers the crosscorrelation process has retrieved the direct air wave, with the latest arrival at around 20 ns, the direct ground wave, with the latest arrival at around 60 ns, and the reflection arrivals from the syncline boundary. It can also be observed that compared to the causal parts in Figure 3.38, the summation of the causal and the anti-causal parts has increased the signal-to-noise ratio of the retrieved multiple of the syncline boundary. In Figure 3.39 this multiple has emerged from the noise.

In practice, it is more likely to encounter electromagnetic noise sources in the GPR range that are only above the ground. Figure 3.40 shows the retrieved common-midpoint gathers for the same midpoints as in the previous figure, but this time when only noise sources in the air are present. It can be seen that the direct ground wave is not retrieved. This is so as the stationary-phase regions that contribute to the retrieval of this arrival come only from sources in the subsurface. It can also be seen that even though the reflected events are retrieved not all the complexity is correctly retrieved.

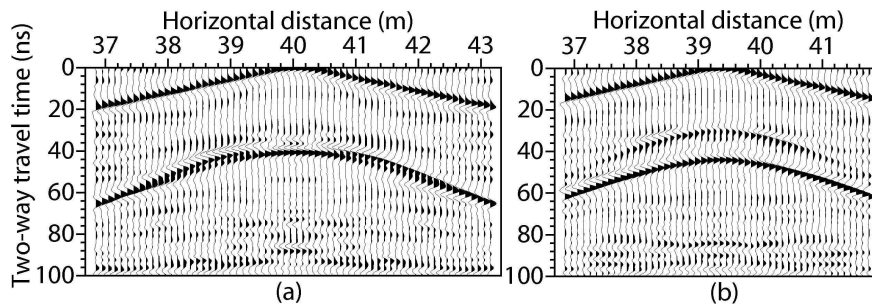


**Figure 3.40:** As in Figure 3.39, but for crosscorrelation of recordings from noise sources only above the receiver antennae.

## **Retrieval of the seismic reflection response: application to laboratory and field data**

---

In this chapter, the SI relations [2.54](#) and [2.59](#) are applied to two types of measured data. First, the transmission responses, observed on a heterogeneous granite sample and resulting from transient sources set off separately in time, are crosscorrelated for the retrieval of reflections from the main velocity contrasts in the granite sample. This is followed by results from the crosscorrelation of recorded background noise. The noise was recorded in a desert area in the Middle East to test the SI method for retrieval of the Earth's reflection response on an exploration scale.



## 4.1 Application to laboratory data from transient sources

The SI relation 2.54 for retrieval of the Green's function from the crosscorrelation of recordings from transient sources is applied to data from a controlled laboratory experiment, which was performed in the ultrasonic laboratory of Dr. Nishizawa in Tsukuba, Japan. The experiment is carried out on a block of granite with dimensions 300x300x100 mm, in which there is a cylindrical hole of 150 mm length and 15 mm diameter filled with epoxy. A sketch of the granite sample is shown in Figure 4.1. The type of the used

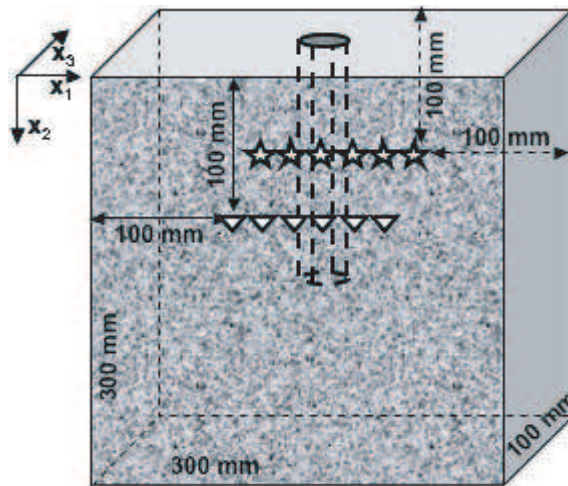


**Figure 4.1:** Oshima granite block with dimensions 300x300x100 mm. A cylindrical hole with a length of 150 mm and a diameter of 15 mm is drilled in the middle of one of the small walls and is filled with epoxy. An observation array of 101 measurement points lies on the front wall with a distance between the points of 1 mm. A source array of 21 source points lies on the back wall with a source spacing of 5 mm. The observation and source arrays are parallel to each other and the plane they lie in is perpendicular to the epoxy cylinder.

granite is "Oshima", which consists mainly of quartz, plagioclase, and biotite

with grain sizes mostly from 1 to 5 mm. The estimated average P-wave and S-wave propagation velocities for this Oshima block are 4500 m/s and 2700 m/s, respectively. The estimated P-wave and S-wave velocities for the epoxy are 2300 m/s and 1400 m/s, respectively. Even though equation 2.54 was derived for the general 3D case, for simplicity here a 2D experiment is considered. This means that in relation 2.54,  $K$  takes on only the values 0 and 2 meaning that we will need to record the response from P- and SV-sources. The observation and source line arrays are placed at opposite sides of the block lying in a plane perpendicular to the long axis of the cylinder. The observation array of 101 measurement points lies along the surface of the front wall of the granite sample; the distance between the observation points is 1 mm. At these points, only the normal component of the particle velocity is measured. This means that in relation 2.54, the subscripts  $p$  and  $q$  take on the value 3 (note the coordinate system in Figure 4.1). The measurements at the observation points are performed using a laser Doppler vibrometer (LDV). Details about the LDV and about the rest of the equipment can be found in Nishizawa et al. [1997] and in Sivaji et al. [2001].

Compared to measurements in the field, in a controlled laboratory experiment one can make use of ultrasonic compressional and shear transducers to approximate separate P- and S-wave sources. The source array, consisting of 21 source points with 5 mm distance between the individual points, is placed along the back wall of the granite block. The sources are fed with a single-cycle 250-kHz sine wavelet. For this frequency, the estimated wavelengths for P-waves and S-waves are 18 mm and 11 mm, respectively. At this scale, the granite sample is effectively heterogeneous and both compressional and shear waves are diffracted from the grains of the sample. Due to the finite diameter (5 mm) of the source transducers, their radiation pattern will not be like the desired point-source pattern [Tang et al., 1994; Nishizawa et al., 1997]. As a result, the compressional transducer will produce some amount of S-wave energy, especially at larger angles with respect to the normal to its flat surface. Still, for the chosen source-receiver geometry the main energy will be radiated in the form of P-waves. A similar effect holds for the shear transducers, which will produce some P-wave energy.

As explained at the beginning of Chapter 3, it can be shown that for the chosen 2D setup sources placed along the walls perpendicular to the observation array would contribute strongly to the retrieval of surface waves,

while sources placed along the wall opposite to the observation array (as in the experiment) will mainly contribute to the retrieval of reflection arrivals. Motivated by this reason, it was chosen to place sources only along the back wall of the granite block.

The measurements are performed in the following order. A source transducer is placed and set off at a certain source point and the resulting wavefields are measured at a point along the observation array. The electronic circuit of the LDV causes the appearance in the recorded waveforms of incoherent high-frequency noise. To eliminate this noise, the source transducer is repeatedly set off at the same position for 2000 times and at the observation point the 2000 recorded waveforms are summed to obtain a final waveform recording at that observation point. By placing a compressional transducer and recording the waveforms at all observation points in the way described above, a P-source transmission common-source gather is obtained. Similarly, placing a shear transducer and repeating the measurements, an S-source transmission common-source gather is obtained. This procedure is repeated for each of the 21 source points. Figure 4.2(a) shows an example P-source transmission common-source gather with a clear P-wave direct arrival with an apex at about 0.024 ms and Figure 4.2(b) shows an example S-source transmission common-source gather with a clear P-wave direct arrival and a clear S-wave direct arrival with an apex at around 0.039 ms. The transmission panels are 0.164 ms long aiming at recording the first few multiples of the direct P- and S-wave arrivals, i.e., the arrivals that have been reflected by both the front and the back wall of the granite block (see Figure 4.1). Even though the later-arriving conversions and multiples are not readily interpretable due to scattering from the grains, parts of the first and the second multiple arrivals of the direct P-wave with estimated apices around 0.07 ms and 0.115 ms, respectively, can be observed in Figure 4.2(c). Parts of the first multiple of the direct S-wave with an estimated apex around 0.115 ms can be seen in Figure 4.2(b).

In the transmission common-source gathers are present also inclined linear arrivals. They result from the presence of the left and right walls of the Oshima granite block (see Figure 4.1). After crosscorrelation and integration following equation 2.54, such events would contribute to retrieval of similar inclined events. These retrieved inclined events would interfere with retrieved reflections. For this reason, a frequency-wavenumber ( $f$ - $k$ ) filter is

used to eliminate the inclined events. The results from the application of the  $f$ - $k$  filter to the transmission gathers in (a) and (b) in Figure 4.2 are shown in (c) and (d), respectively, where the multiples can be observed more clearly. The presence of coherent arrivals at later times shows that the recordings are of deterministic fields. The recording of the transmission responses are stopped before diffuse fields from multiple scattering from the grains start arriving. Even though crosscorrelation of multiple scattered fields would improve the resolution of the retrieved reflections, it would require much longer transmission recordings (at least one order longer) to approximate the equipartition regime, i.e., when the wavefields have no preferred wavenumber (see, for example, Larose et al. [2006]).

In the transmission responses can also be seen nearly horizontal arrivals around 0.08 ms and 0.125 ms that arise from the presence of the top wall in Figure 4.1 and thus represent 3D (out-of-plane) events. These arrivals cannot

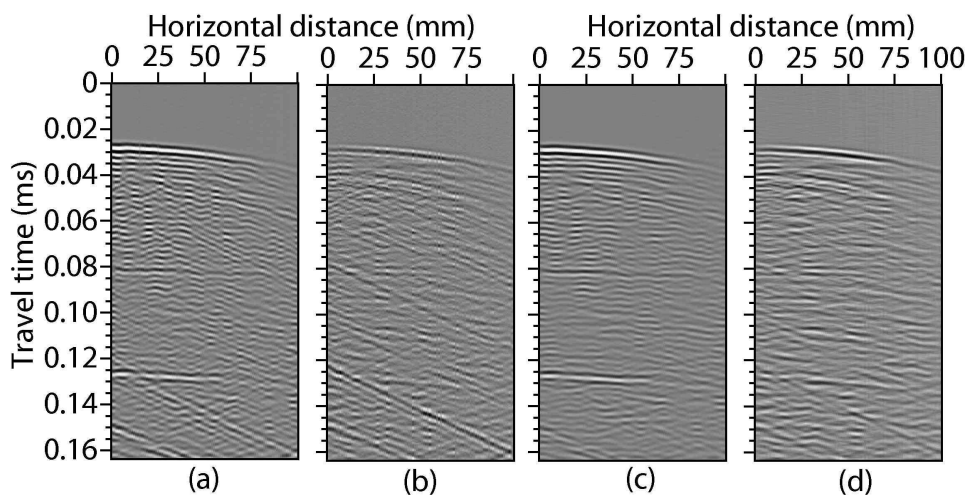


**Figure 4.2:** Transmission common-source gathers from a source transducer at 0 mm, i.e., at the left end of the arrays. The amplitudes are clipped to bring forward later arrivals. (a) Observed normal particle velocity due to a compressional source transducer. (b) Observed normal particle velocity due to a shear source transducer. (c) As in (a), but after  $f$ - $k$  filtering. (d) As in (b), but after  $f$ - $k$  filtering.

be filtered out as their behavior in the f-k domain is very similar to the direct transmission arrivals and their free-surface multiples. After crosscorrelation and integration, such out-of-plane events will cause the appearance of ghosts in the retrieved results.

By placing a source transducer at a position of an observation point and recording the resulting wavefields along the observation array, a reflection common-source gather is obtained. Such a panel will be used to verify possible retrieved reflections.

Following equation 2.54, a master trace is chosen, for example at  $\mathbf{x}_B = (50, 0)$  mm. For an f-k-filtered P-source transmission common-source gather, the master trace  $v_{3,0}^{obs}(\mathbf{x}_B, \mathbf{x}, t)$  is correlated with the whole gather. The P-source gather represents  $v_{3,0}^{obs}(\mathbf{x}_A, \mathbf{x}, t)$  for variable  $\mathbf{x}_A$  and fixed  $\mathbf{x}$ . The correlation result is deconvolved with a wavelet extracted around zero time from the autocorrelation trace. The result after the deconvolution is a P-source correlation panel. The correlation and deconvolution operations are repeated for all P-source transmission common-source gathers and the separate P-source correlation panels are summed together. The causal part of the results is shown in Figure 4.3(a). The above procedure is repeated for all S-source transmission common-source gathers as well, see Figure 4.3(b). To obtain a retrieved reflection common-source gather, panels (a) and (b) in Figure 4.3 are summed together. The retrieved reflection common-source gather represents retrieved particle velocity in a direction normal to the front wall due to a source placed at the granite block's front wall at  $\mathbf{x}_B = (50, 0)$  mm and acting in the normal direction to this wall.

After a reflection common-source gather is retrieved, it should be compared to a directly observed reflection common-source gather. Figure 4.4 shows the retrieved reflection common-source gathers for a retrieved source position at 50 mm (a) and 25 mm (d), where the star symbol indicates the source position. Figure 4.4 also shows the directly observed reflection common-source gathers for a compressional transducer at 50 mm (b) and 25 mm (e) after f-k filtering for removal of the surface waves and deconvolution. The removal of the surface waves is not a trivial task as the inhomogeneities close to the surface cause dispersion. Due to the physical presence of the source transducer the near offsets could not be recorded. The presence of inhomogeneities in the Oshima granite makes both pictures look cluttered and makes the interpretation and comparison of reflection events difficult. To facilitate the inter-

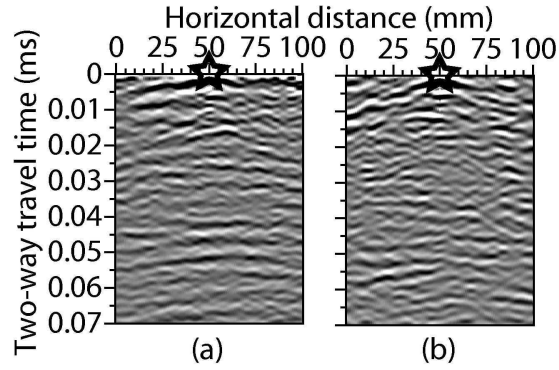


**Figure 4.3:** (a) Causal part of the result from the correlation with a master trace at 50 mm after integration of P-source correlation panels. (b) Causal part of the result from the correlation with a master trace at 50 mm after integration of S-source correlation panels. The amplitudes are clipped to bring forward later arrivals.

pretation of the main events and compare the gathers, a 2D elastic numerical modeling was performed with a finite-difference scheme using a homogeneous background velocity model with a circle in it. This circle represents the cross section of the epoxy cylinder. The dimensions and velocities of the model were the same as the dimensions and the estimated average velocities of the granite block. Gathers (c) and (f) in Figure 4.4 show the modelling results (without the surface waves) for the same source positions. Note that these modelling results should only be used for interpretation of expected reflection arrivals. The modelling results are not representative for the clutter due to the inhomogeneous background of the Oshima granite block. This means that a reflection arrival visible in a modelled common-source gather might be (partly) obscured by diffractions in the observed and the retrieved common-source gathers.

In the numerically modelled results in Figure 4.4, the most prominent events are the top-of-cylinder reflection arrivals with apices around 0.018 ms, the bottom-of-cylinder reflection arrivals with apices around 0.035 ms, and the reflection arrivals from the granite block's back wall, which arrive around 0.045 ms. The back-wall reflection event is followed by a train of conver-



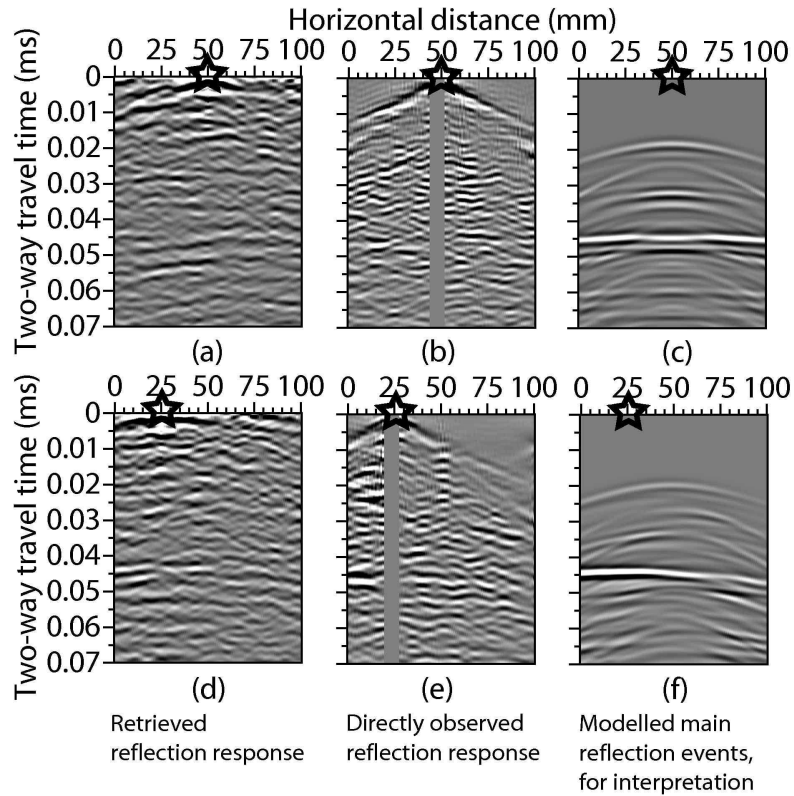


**Figure 4.4:** (a) A retrieved reflection common-source gather representing observed normal particle velocity due to a retrieved normal force source at position  $\mathbf{x}_B = (50, 0)$  mm. (b) Directly observed normal particle velocity reflection common-source gather for the same source position after  $f$ - $k$  filtering and deconvolution. (c) Numerically modelled normal particle velocity reflection common-source gather for the same source position after removing the surface waves. (d) Same as in (a) but for a source at position  $\mathbf{x}_B = (25, 0)$  mm. (e) Same as in (b) but for a source at position  $\mathbf{x}_B = (25, 0)$  mm. (f) Same as in (c) but for a source at position  $\mathbf{x}_B = (25, 0)$  mm.

sions. Due to the missing offsets and the remnants of the surface waves, it is hard to interpret the top-of-cylinder reflection in the directly observed

reflection common-source gathers. Parts of this reflection might be present for the source position at 50 mm. Another factor making the interpretation of the top-of-cylinder reflection difficult is due to interference with linear events in the directly observed data coming from the left and right walls of the granite block and remaining after the f-k filtering. Such events are easier to remove in the transmission panels and after crosscorrelation and summation their effect on the retrieved results is much smaller. On the retrieved reflection common-source gathers, the apices of the top-of-cylinder reflection are visible and the wings of the reflection can be traced from the apex until 100 mm in Figure 4.4(a) and from 0 mm until the apex in Figure 4.4(d). The back-wall reflection in the retrieved common-source gathers is at least as good as the reflection in the observed common-source gathers. In Figure 4.4(a) the retrieved back-wall reflection is even more continuous than in the directly observed reflection gather. The bottom-of-cylinder reflections are not interpretable in both the directly observed and the retrieved common-source gathers. In the retrieved reflection common-source gathers, we can

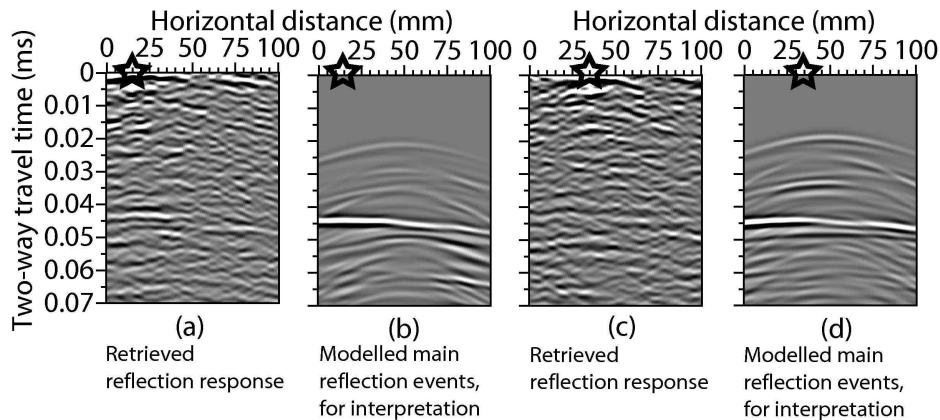


**Figure 4.5:** (a) A retrieved reflection common-source gather for a retrieved source at position  $\mathbf{x}_B = (15, 0)$  mm. (b) Numerically modelled reflection common-source gather for the same source position after removing the surface waves. (c) Same as in (a) but for a source at position  $\mathbf{x}_B = (36, 0)$  mm. (d) Same as in (b) but for a source at position  $\mathbf{x}_B = (36, 0)$  mm.



see linear ghost events, like the ones at around 0.05 ms, which are a result from the presence of the out-of-plane events in the transmission data.

The gathers in (a) and (c) in Figure 4.5 are two more examples of retrieved reflection common-source gathers for retrieved source positions at 15 mm and 36 mm, respectively. Comparing these results with the numerically modelled reflection common-source gathers in (b) and (d), respectively, for the same source positions, it can be seen that the back-wall reflection has been retrieved very well. In Figure 4.5 even the bottom-of-cylinder reflection is retrieved and can be observed from 0 mm until its apex.

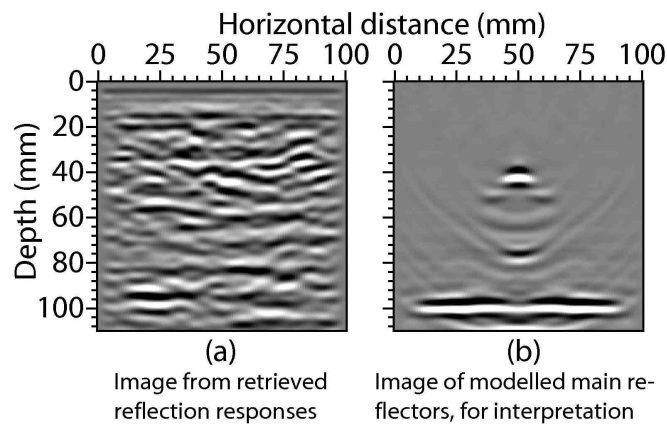


**Figure 4.6:** Comparison between images of the interior of the sample obtained from reflection events retrieved through crosscorrelation (a) and numerically modelled reflection events (b). The images were obtained using a prestack depth migration algorithm with homogeneous velocity of 4500 m/s.

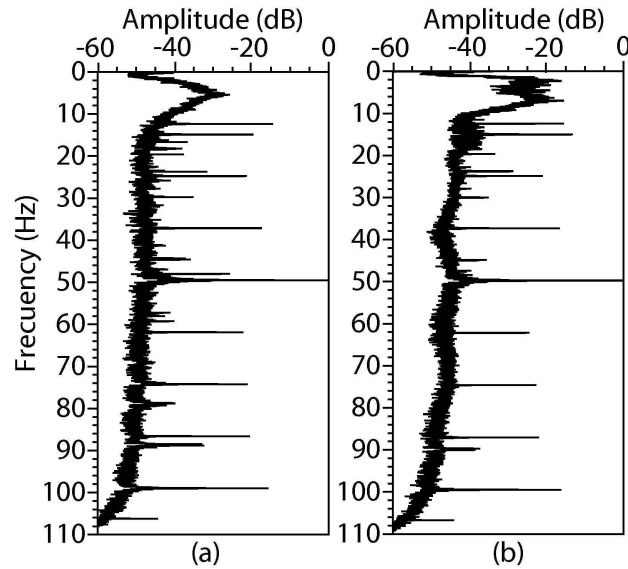
Having retrieved reflection common-source gathers for a retrieved source position at the position of every receiver, we can make use of imaging techniques to look into the interior of the granite sample. Figure 4.6(a) shows the imaging result from the application of prestack depth migration to the retrieved reflection events using a homogeneous model with a velocity of 4500 m/s, i.e., the estimated average propagation velocity of P-waves through the granite sample. The image is quite cluttered, as it can be expected for an

image of an inhomogeneous sample, and because of this it is difficult to describe it in terms of imaged grains of the granite sample, imaged epoxy cylinder, imaged back wall of the sample, and artefacts due to the out-of-plane events. To verify whether grains in the sample have been imaged, directly observed reflection measurements would be needed from a source at each of the receiver positions. Such measurements are not available. To facilitate the interpretation of the left image in Figure 4.6(a), the image obtained from the migration of the numerically modelled results is shown in Figure 4.6(b). This image can be used to identify only the main reflectors in the granite block - the epoxy cylinder and the back wall of the granite, but is not representative for imaged inhomogeneities (grains) inside the granite block. Comparing the two images in Figure 4.6, it can be seen that by using only a few sources at the back wall of the block, the top of the cylinder and the granite sample's back wall have been successfully imaged.

## 4.2 Application to field data from background-noise sources

In this section, the SI relation 2.59 is applied to field data. The data used for crosscorrelation were recorded in the Middle East in 2005 by South Rub Al-Khali Company Limited (SRAK) with Shell's technical advice and support. The experimental set-up consisted of 17 standard exploration three-component geophones arranged in a single line. The geophone spacing was 50 m and the time-sampling rate was 4 ms. The geophone array (passive array) was planted in a desert area with the idea that during the recording of the background noise the cultural noise would be minimal. An active seismic survey was available along the line of the passive array, allowing for verification of the retrieved reflections. The acquisition equipment allowed for a continuous recording of noise for 70 s. The recording was then interrupted for about 30 s to store the already acquired data, after which the recording continued. This resulted in 523 records (noise panels) with a length of 70 seconds each, amounting to about ten hours of seismic background-noise data.

The recorded background-noise data were inspected in the frequency domain. Even though the recorders were sensitive to frequencies between 1



**Figure 4.7:** Example frequency spectra of two 70-seconds-long noise panels as recorded by the vertical components of the passive array's geophones. (a) The spectrum of the noise panel in Figure 4.8. (b) The spectrum of the noise panel in Figure 4.9.

Hz and about 100 Hz, it was found that the useful information was concentrated between 2 Hz and 10 Hz (see Figure 4.7). In this frequency band, the noise panels show mainly random noise and propagating energy in the form of weak surface waves. Figure 4.8 shows the vertical particle velocity component of one such noise panel that is band-pass filtered between 2 Hz and 10 Hz. Note that the trace at 50 m is zero since the geophone at that position was not functioning. The amplitudes of the surface waves are of the same order as the amplitudes of the rest of the noise. After crosscorrelation, these events will contribute to the retrieval of the surface waves part of the Green's function.

Among the 523 noise panels, there were 35 panels in which coherent arrivals could be recognized with very high apparent propagation velocity. Figure 4.9 shows a band-pass filtered example of one such panel as recorded by the

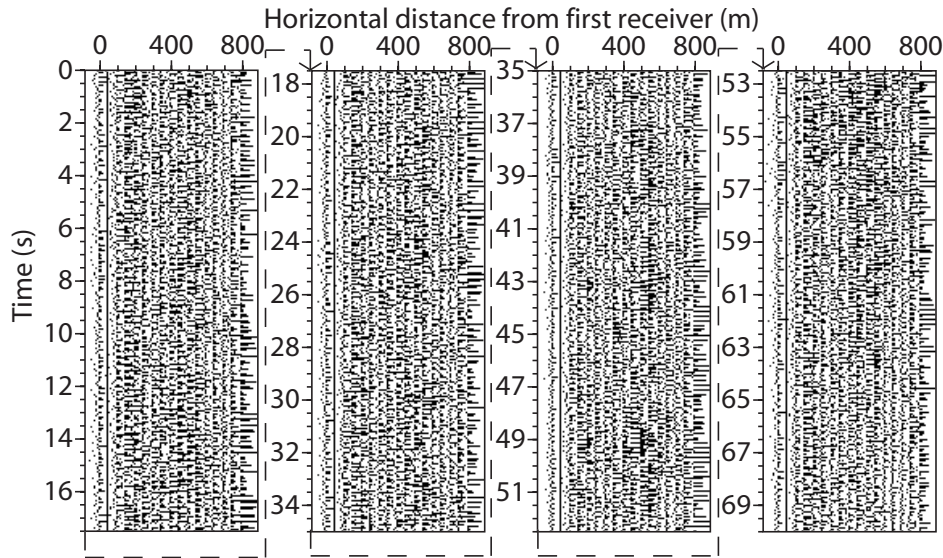


**Figure 4.8:** An example 70-seconds-long noise panel as recorded by the vertical components of the passive array's geophones and filtered between 2 Hz and 10 Hz.

vertical components of the passive array's geophones.

Figure 4.10 shows a 10-seconds-long part of the noise panel from Figure 4.9 as recorded in the frequency band between 2 Hz and 10 Hz by all three components of the geophones. On the vertical component (Z) a nearly horizontal arrival can be observed starting at about 12 seconds. Because this arrival is absent on the horizontal components (X and Y), it is interpreted as propagating energy due to body P-waves from deep sources lying vertically below the passive array. After crosscorrelation, this type of events will contribute to the retrieval of reflected arrivals in the Green's function. Most of the nearly horizontal coherent events have amplitudes in the order of the background noise from the other noise panels, like the example in Figure 4.8, i.e., the random noise and the surface waves. Only two panels exhibit nearly horizontal arrivals with much stronger amplitudes. The panel with the strongest amplitudes, approximately 100 times stronger than the background noise from the other noise panels, is the one shown in Figure 4.10.

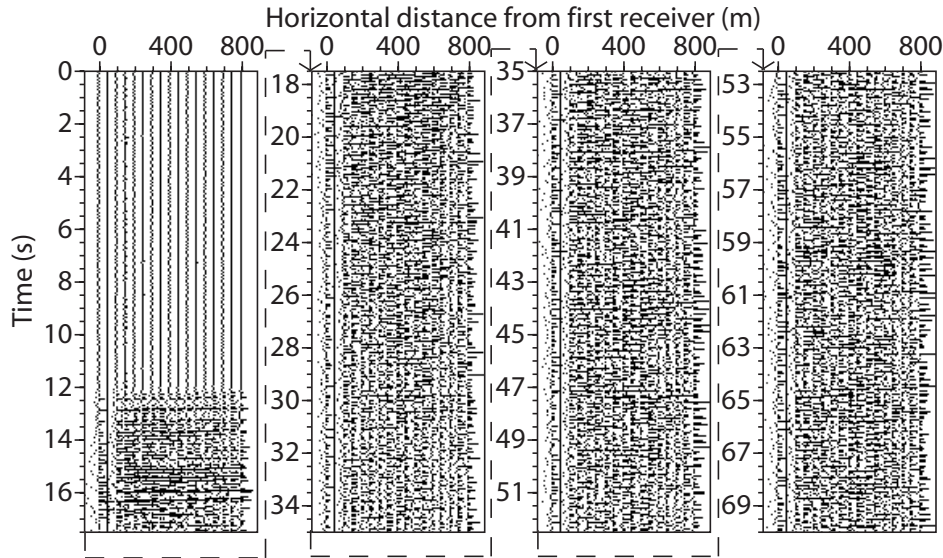


**Figure 4.9:** An example of a noise panel containing coherent arrivals with very high apparent propagation velocity. This example shows the vertical components of the passive array's geophones filtered between 2 Hz and 10 Hz. The amplitudes are clipped to bring forward later arrivals.

To try to understand the nature of the nearly horizontal arrivals, arrival times of body waves from available information of earthquakes on a global scale ( $M > 1.9$ ) are compared with the arrival times of the events in Figure 4.10. The comparison failed to show any correlation. This suggests that the nearly horizontal events are caused by a few local natural subsurface sources that may be due to, for example, local microseismicity.

Using SI relation 2.59, in order to retrieve the vertical particle velocity component of the reflection response that would be recorded by the array of geophones when there would be a force source acting in the vertical direction at the position of one of the geophones, the following procedure is used. A master trace  $v_3^{obs}(\mathbf{x}_B, t)$  is chosen at a geophone position, for example at the position of the first geophone. Since the amplitude of the noise in the different noise panels varies significantly, each noise panel is energy-normalized separately. Then the vertical component of the master trace is extracted from

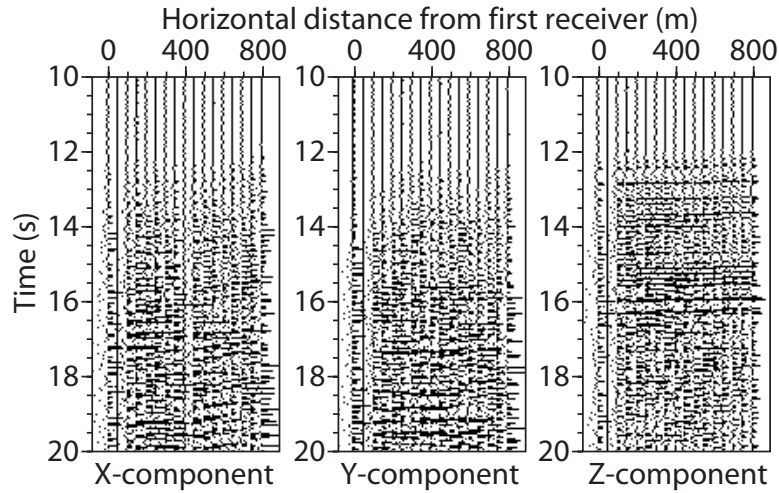


**Figure 4.10:** Part of the noise panel from Figure 4.9 around the first nearly horizontal arrival as recorded by the horizontal in-line (X), the horizontal cross-line (Y), and the vertical (Z) components of the geophones. Starting at about 12 seconds one can see coherent arrivals with very high apparent velocity resulting from body-wave arrivals (see text for explanation).

each noise panel and is correlated with the vertical components of the traces in the same panel. The vertical components of the traces in the noise panel represent  $v_3^{obs}(\mathbf{x}_A, t)$  for variable  $\mathbf{x}_A$ . The correlation results in 523 correlation panels, which are subsequently summed together. The summation result is then deconvolved, with a wavelet extracted around zero time from the autocorrelation trace, and band-pass filtered between 2 Hz and 10 Hz to obtain the causal and anti-causal parts of a common-source gather with retrieved source position at the position of the first geophone. As explained in Chapter 3, if the background-noise sources illuminate the passive array from all directions, then the retrieved causal and anti-causal parts will be the same. When the illumination is not optimal, then some parts of the Green's function might be retrieved in the causal part, while others in the anti-causal part. Because here the illumination from the background-noise sources is not known, the causal and the time-reversed anti-causal parts of the retrieved



result are summed together to obtain more complete retrieval.

The above procedure is repeated to retrieve common-source gathers with retrieved source positions at 16 geophone positions of the passive array (recall that one geophone was not functioning).

By using more noise panels in the summation process after crosscorrelation, effectively one uses longer background-noise recordings. Figure 4.11 shows the gradual build-up of the retrieved vertical particle velocity common-source gather for a retrieved vertical force source at the position of the first geophone when summing an increasing number of correlation panels, i.e., when crosscorrelating increasingly longer background-noise recordings. It can be observed that the amount of retrieved coherent events increases with increasing recording time. This is due to the fact that with longer recording times more propagating seismic energy is captured. Moreover, the underlying assumption that the background-noise sources are temporally uncorrelated is better fulfilled with longer recording times.

Figure 4.11(g) shows the retrieved common-source gather with a retrieved source position at 0 m after crosscorrelation and summation of all 523 noise panels. On this retrieved common-source gather several coherent arrivals can be identified. The inclined coherent event, starting at 0 s at zero source-receiver offset and ending in the range of 0.9 s to 1.8 s at the maximum offset, is interpreted as a dispersive surface wave. Such inclined events are present in all retrieved common-source gathers. In Figure 4.11(g) also several coherent nearly horizontal events can be observed. The events at around 0.3 s, 0.9 s, 1.25 s, and 2.15 s might be retrieved reflections and result, as explained above, from the crosscorrelation of the nearly horizontal coherent events, like the ones in Figure 4.10, present in the background-noise data.

To evaluate the quality of the results, the retrieved common-source gathers are compared with data from an active seismic reflection survey acquired at the same location. The active survey was carried out a short time before the background-noise experiment. The active survey used seismic vibrators as sources at the surface and single vertical component geophones as recorders with a geophone spacing of 25 m. The largest source-receiver offset in the active survey was much larger than the offsets in the passive array. The comparison of the retrieved common-source gathers with the active survey common-source gathers is not trivial.

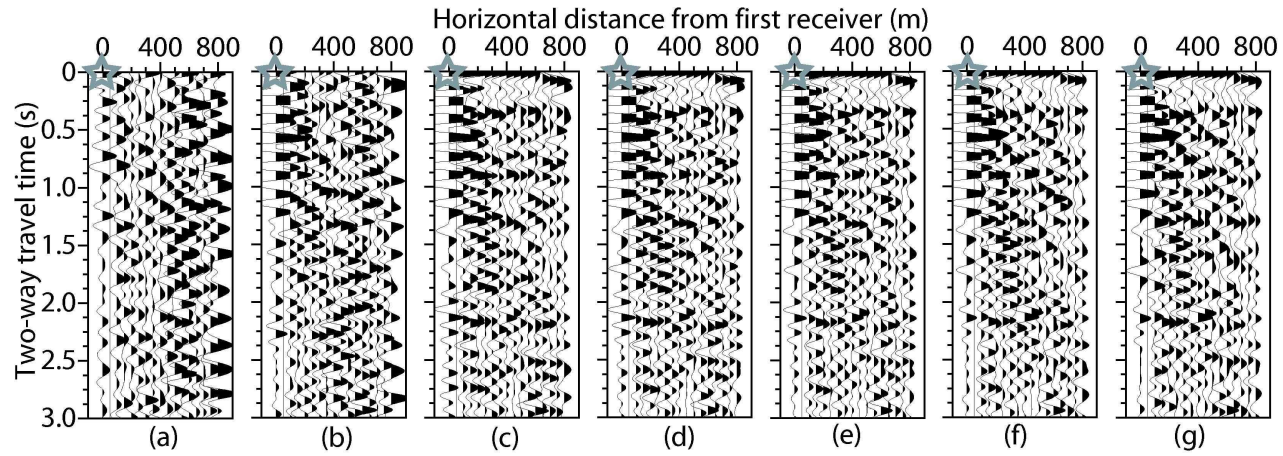


**Figure 4.11:** Gradual build-up of a retrieved common-source gather with a retrieved source position at the position of the first geophone from the passive array, i.e., at 0 m, after crosscorrelation of (a) 70 s, (b) 1 hour, (c) 2 hours, (d) 4 hours, (e) 6 hours, (f) 8 hours, and (g) 10 hours of background noise.



One problem is that the frequency content of the two data sets is different. In the active reflection data, the propagating energy was concentrated between 10 Hz and 50 Hz, while the frequency band of the propagating energy in the background-noise data was between 2 Hz and 10 Hz. As a result, separate events recorded short after one another in the active survey may appear as a single event in the retrieved common-source gathers. The surface waves in the active reflection survey are concentrated in the frequency band up to 20 Hz. This made it easier to compare them with the retrieved inclined coherent events in the retrieved common-source gathers. The conclusion is that the inclined coherent events are indeed retrieved surface wave arrivals. But it is more interesting to see whether reflection arrivals have been retrieved. The comparison of the retrieved nearly horizontal coherent events, like the ones at around 0.3 s, 0.9 s, 1.25 s, and 2.15 s in Figure 4.11(g), with reflection hyperbolae in the active data is more difficult. This is due to the different frequency bands, the different quality of the retrieved nearly horizontal coherent events in the different retrieved common-source gathers, and the fact that in the raw active common-source gathers the reflection hyperbolae are not easily observed.

To improve the clarity of reflection arrivals in both data sets, the following processing steps are performed. At the location of the passive array the subsurface geology consists of nearly horizontal layers. This means that for the considered short offset ranges – 800 m – the subsurface can be assumed to be horizontally layered. With this assumption in mind, the traces in the 16 retrieved common-source gathers are resorted into common-offset gathers. Next, the traces in each common-offset gather are summed and normalized for the number of summed traces, producing a single output trace per common-offset gather. The output traces from the different common-offset gathers are sorted into a so-called common-offset stack gather, see Figure 4.12(a). The same procedure is applied to the active data as well, using 17 common-source gathers with source positions around the corresponding locations of the geophones from the passive array.

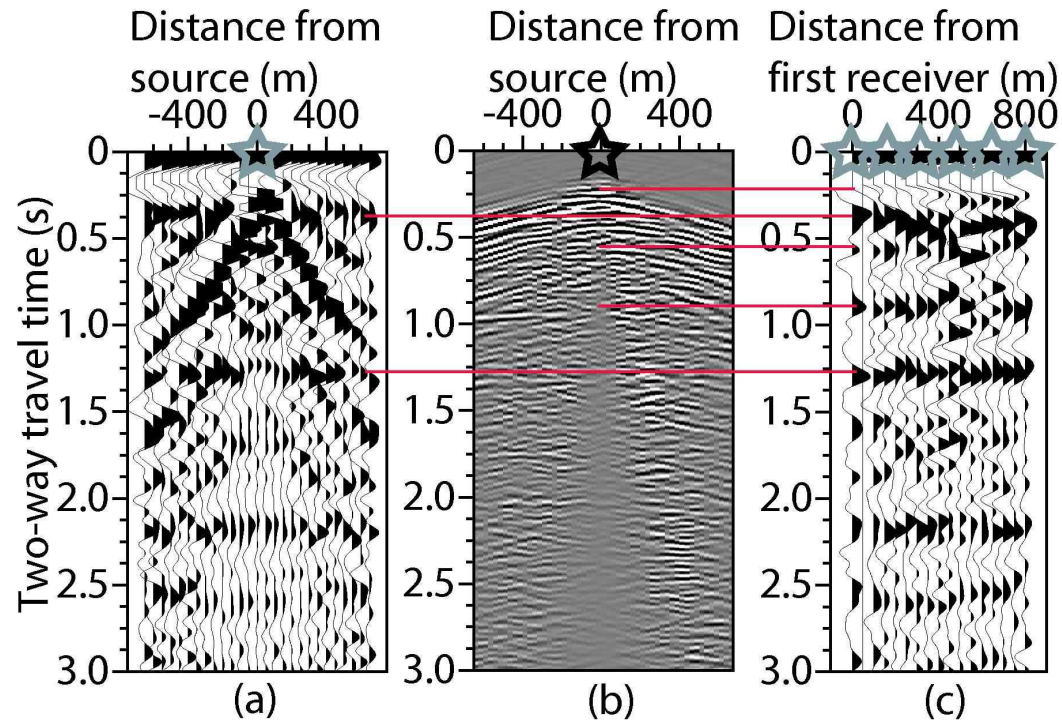


**Figure 4.12:** (a) A common-offset stack gather obtained from the common-source gathers retrieved from the passive data. (b) A common-offset stack gather obtained from the common-source gathers from the active data after surface wave elimination and band-pass filtering between 13 Hz and 33 Hz. (c) A line-source reflection response obtained by summing the common-source gathers retrieved from the passive data (brute stack). The red lines indicate travel-time correspondence between events retrieved from the passive data and reflection hyperbolae in the active data.

The resulting common-offset stack gather is further filtered in the  $f$ - $k$  domain to eliminate the surface waves and then band-pass filtered between 13 Hz and 33 Hz (see 4.12(b)). As a result of this processing, the individual coherent events have been strengthened, albeit at the expense of some loss of resolution. The above processing allows to compare the arrival times of the coherent events in (a) with the reflection hyperbolae in (b) (the comparison is indicated by the red lines). There is a very good arrival-time agreement between two retrieved events, indicated by the red lines, and corresponding reflection hyperbolae in the active data.

Even though the above processing of retrieved results has made the comparison easier, the retrieved surface waves in Figure 4.12(a) hamper the good comparison between the two datasets. Due to the very narrow frequency band of the retrieved data, it is inappropriate to use an  $f$ - $k$  filter to eliminate the retrieved surface waves. Instead, the inclined coherent events are suppressed in a different way. By simply summing the retrieved common-source gathers, a reflection response to a line source is created along the geophones of the passive array, see Figure 4.12(c). This operation is called a brute stack. As a result of this operation, the horizontal arrivals are enhanced whereas the inclined arrivals are suppressed. The comparison of the retrieved horizontal events in (c) with the reflection hyperbolae in (b) is now even easier – the retrieved coherent events show very good arrival-time agreement with the reflection hyperbolae in the active data. Only the latest coherent events in the retrieved results cannot be related to events in the active data. If though, one looks at longer offsets in the active data, even the later retrieved coherent arrivals can be related to reflection hyperbolae in the active data (see Figure 4.13). Because of the above reasons, it is concluded that the retrieved coherent events in Figure 4.13(c) are retrieved reflection arrivals.

As was mentioned at the beginning of this section, the crosscorrelation of surface wave arrivals in the background noise will contribute to the retrieval of surface waves, while the crosscorrelation of the nearly horizontal arrivals in the background noise will contribute to the retrieval of reflections. Using this fact, even better retrieved reflections can be obtained. To do this, only background-noise panels are crosscorrelated, which contain nearly horizontal arrivals in them, i.e., 35 noise panels are crosscorrelated. The result from the common-offset stack processing of the retrieved common-source

gathers and the result of the line-source (brute stack) processing are shown in Figure 4.14(a) and Figure 4.14(c), respectively. It can be seen that the retrieved reflection arrivals are now much clearer. Figure 4.14(b) repeats for comparison convenience the common-offset stack gather obtained from the active data. It can be concluded that selective crosscorrelation of parts of the seismic background noise could improve the retrieval of reflection arrivals.

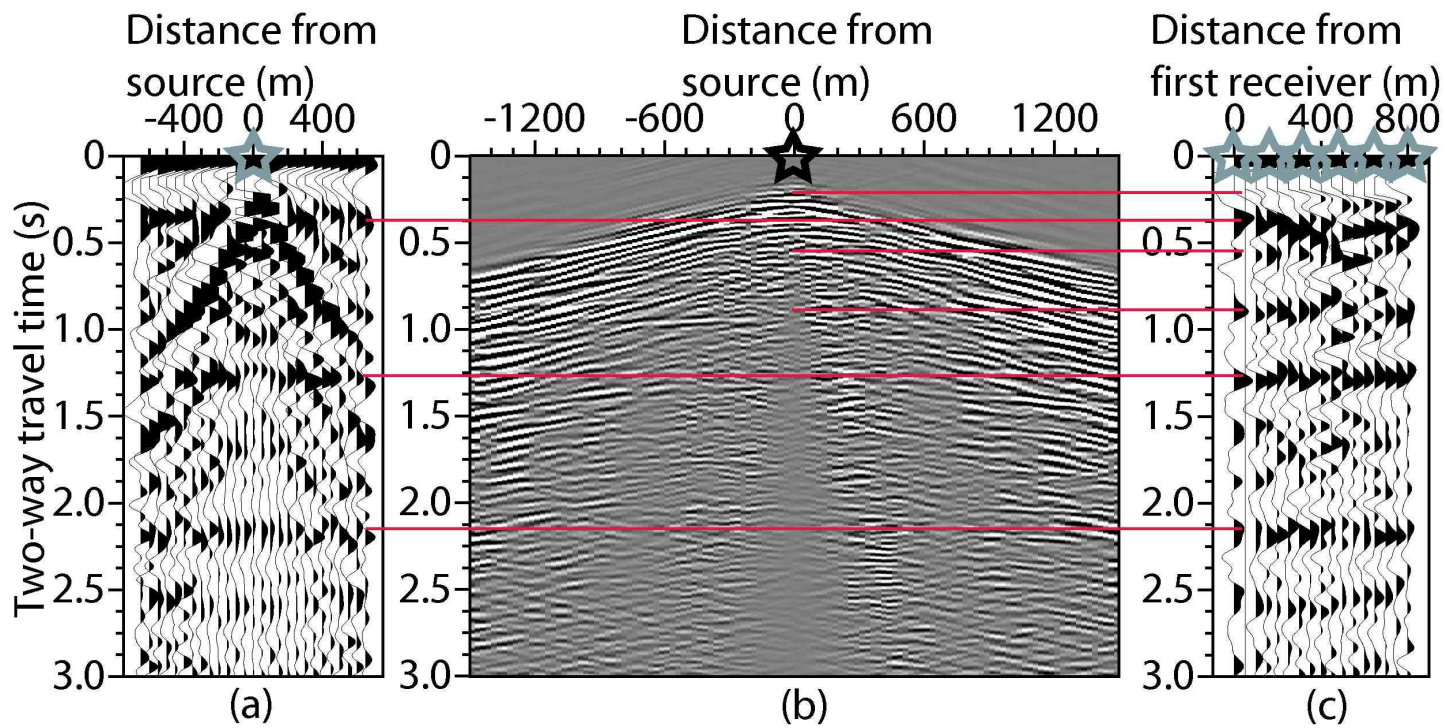


**Figure 4.13:** As in Figure 4.12, but the active data common-offset stack gather is shown for larger offsets. Now, even the later retrieved arrivals can be related to reflection events in the active data.



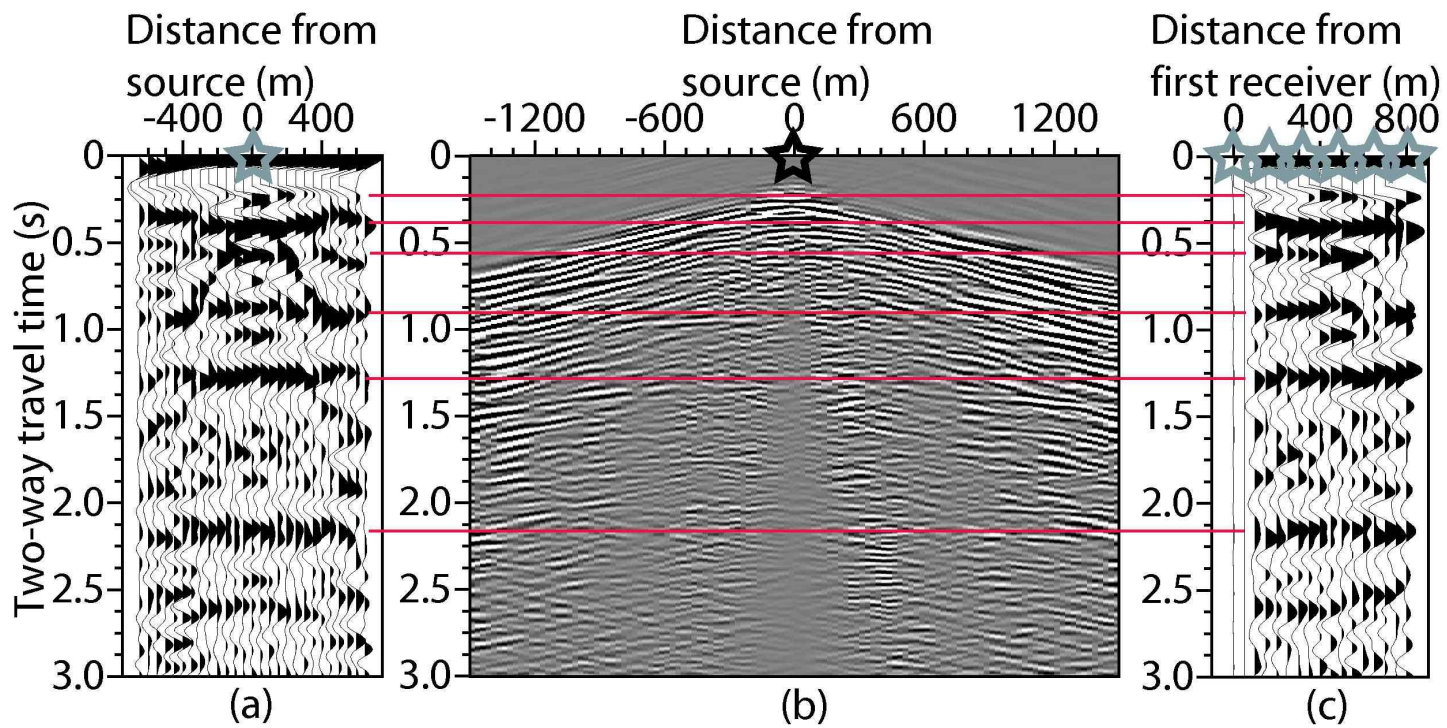


**Figure 4.14:** As in Figure 4.13, but this time the retrieved results are obtained only from crosscorrelation of noise panels, in total 35, containing nearly horizontal coherent arrivals.



## Conclusions

---

In this thesis it is shown that by crosscorrelating observed seismic or electromagnetic wavefields at two points, one can retrieve a new response of a corresponding wave type at one of the points as if there were a source of corresponding wavefields at the other point. This process is called Seismic Interferometry (SI) when observed seismic responses are crosscorrelated, or Electromagnetic Interferometry (EMI) when electromagnetic responses are crosscorrelated. Using two-way and one-way wavefield reciprocity theorems, SI and EMI relations were derived that can be used in different situations. It was shown that:

- By crosscorrelating at two points the responses, which originate from transient sources that act separately in time and which surround the two points, a transient response and its time-reversed version are retrieved at one of the points as if there were a transient source at the other point.
- When the measurements at the two points result from uncorrelated noise sources, no separate measurements from these sources are needed. By simply crosscorrelating the observed responses at the two points,



a response and its time-reversed version are retrieved at one of the points as if there were a source at the other point. The retrieved source wavelet is characterized by the autocorrelation of the noise sources.

- The crosscorrelation of observed transmission responses at two points at the Earth's surface from sources in the subsurface would retrieve the response between these two points - reflection response, surface waves, direct waves. When there are no subsurface sources lying close to the surface, the retrieved surface waves will be very weak or might even be absent.
- To retrieve the reflection response from natural subsurface noise sources, the crosscorrelated transmission observations need to be very long - in the seismic case this means hours, days, months. The longer the recorded noise, the better the retrieved reflection response.
- To retrieve the reflection response from separate measurements from transient subsurface sources, the crosscorrelated transmission observations do not need to be long - the length is dictated by the arrival time in the observed transmissions of the latest event to be retrieved.
- When the observation points are illuminated by the subsurface sources from all directions, the crosscorrelation will retrieve the complete reflection response. Moreover, the retrieved reflection response and its time-reversed version will be symmetric. When the illumination from the subsurface sources is not optimal, the retrieval result will not be complete. Some parts of the reflection response might be retrieved in the causal part and other parts - in the anti-causal part of the crosscorrelation result. In such cases, for more complete retrieval, the causal and the time-reversed anti-causal parts might be summed together.
- In the case of big gaps in the distribution of the subsurface sources as well as in the case of very few subsurface sources, the retrieved reflection response might be incomplete. Nevertheless, due to the possibility to retrieve reflection responses between any two observation points, one can make use of advanced imaging techniques. When all the retrieved reflection responses are migrated, the migration process

will remedy the incomplete retrieval and the subsurface will be correctly imaged.

The migration technique, which incorporates crosscorrelation, can be applied directly to observed transmission recordings from noise sources. The result from direct migration of noise recordings and the result of migrating retrieved through crosscorrelation responses are identical. The usage of one or the other depends on the specific application.

- The SI and EMI relations, derived in this thesis, are valid for lossless media. When losses are present, the crosscorrelation will still retrieve the reflection response. Only some of the later arrivals - later primaries, multiples, conversions - might not be retrieved. When the losses in the medium increase, ghosts may appear in the retrieved results.
- The SI and EMI relations, derived for practical field applications, make use of a medium that is homogeneous and isotropic outside the boundary, on which the sources lie. When inhomogeneities are present outside this boundary, ghost events appear in the retrieved results. When, though, the source boundary is sufficiently irregular, the ghost events in the retrieved results are strongly weakened and might even disappear.
- Reflections were retrieved from crosscorrelations of measured transmission responses in a seismic ultrasonic laboratory experiment. The transmission measurements were made on a heterogeneous Oshima granite block using separate transient P-wave and S-wave source transducers. The retrieved reflection responses were used in a migration procedure and successfully imaged the main reflectors of the granite sample.
- Reflection arrivals from body waves (as well as surface waves) were retrieved from crosscorrelation of observed seismic background noise in an exploration-scale experiment. The crosscorrelation results showed that indeed the longer the recorded background noise, the more complete the retrieved response. When for crosscorrelation are used only parts of the background noise, which contain transmission body-wave

arrivals, the retrieved responses contained much weaker retrieved surface waves. The retrieval of reflection arrivals from background-noise exploration-scale data showed that the SI method may be used for exploration purposes, for example, in frontier exploration or for exploration in environmentally sensitive areas.

# Bibliography

---

- Aki, K. and J. P. Richards, 2002, Quantitative siesmology: University Science Books, second edition.
- Artman, B., D. Draganov, K. Wapenaar, and B. Biondi, 2004, Direct migration of passive seismic data: 66th Conference and Exhibition, EAGE, Extended abstracts P075.
- Bakulin, A. and R. Calvert, 2004, Virtual Source: new method for imaging and 4D below complex overburden: 74th Annual International Meeting, SEG, Expanded abstracts, 2477–2480.
- Baskir, E. and C. E. Weller, 1975, Sourceless reflection seismic exploration: *Geophysics*, **40**, 158.
- Berkhout, A. J., 1982, *Seismic migration*: Elsevier.
- Berkhout, A. J., 1997, Imaging and characterization with CFP technology, an overview: 67th Annual International Meeting, SEG, Expanded abstracts, 1766–1769.
- Berkhout, A. J. and D. J. Verschuur, 2003, Transformation of multiples into primary reflections: 73rd Annual International Meeting, SEG, Expanded abstracts, 1925–1928.
- Berkhout, A. J. and D. J. Verschuur, 2006, Imaging of multiple reflections: *Geophysics*, **71**, SI209–SI220.
- Bojarski, N. N., 1983, Generalized reaction principles and reciprocity theorems for the wave equations, and the relationship between the time-advanced and the time-retarded fields: *Journal of the Acoustic Society of America*, **74**, 281–285.
- Campillo, M. and A. Paul, 2003, Long-range correlations in the diffuse seismic coda: *Science*, **299**, 547–549.
- Claerbout, J. F., 1968, Synthesis of a layered medium from its acoustic transmission response: *Geophysics*, **33**, 264–269.
- Claerbout, J. F., 1971, Toward a unified theory of reflector mapping: *Geophysics*, **36**, 467–481.

- Cole, S., 1995, Passive seismic and drill-bit experiments using 2-D arrays: Ph.D. thesis, Stanford University.
- Corones, J. P., M. E. Davison, and R. J. Krueger, 1983, Direct and inverse scattering in the time domain via invariant imbedding equations: *Journal of the Acoustic Society of America*, **74**, 1535–1541.
- Curtis, A., P. Gerstoft, H. Sato, R. Snieder, and K. Wapenaar, 2006, Seismic interferometry - turning noise into signal: *The Leading Edge*, **25**, 1082–1092.
- Daneshvar, M. R., C. S. Clarence, and M. K. Savage, 1995, Passive seismic imaging using microearthquakes: *Geophysics*, **60**, 1178–1186.
- de Hoop, A. T., 1988, Time-domain reciprocity theorems for acoustic wave fields in fluids with relaxation: *Journal of the Acoustic Society of America*, **84**, 1877–1882.
- de Hoop, M. V., 1992, Directional decomposition of transient acoustic wave fields: Ph.D. thesis, Delft University of Technology.
- de Hoop, A. T., 1995, *Handbook of radiation and scattering of waves*: Academic Press, Amsterdam.
- Derode, A., E. Larose, M. Tanter, J. de Rosny, A. Tourin, M. Campillo, and M. Fink, 2003, Recovering the Green's function from field-field correlations in an open scattering medium: *Journal of the Acoustic Society of America*, **113**, 2973–2976.
- Draeger, C. and M. Fink, 1997, One-channel time-reversal of elastic waves in a chaotic 2D silicon cavity: *Physical Review Letters*, **79**, 407–410.
- Draganov, D., K. Wapenaar, and J. Thorbecke, 2003, Synthesis of the reflection response from the transmission response in the presence of white noise sources: 65th Conference and Exhibition, EAGE, Extended abstracts P218.
- Draganov, D., K. Wapenaar, and J. Thorbecke, 2004, Passive seismic imaging in the presence of white noise sources: *The Leading Edge*, **23**, 889–892.

- Draganov, D. and K. Wapenaar, 2004, Passive seismic imaging with noise sources in complex medium: 7th International Symposium on Imaging Technology, Extended abstracts 150–155.
- Draganov, D., K. Wapenaar, W. Mulder, J. Singer, and A. Verdel, 2007a, Retrieval of reflections from seismic background-noise measurements: *Geophysical Research Letters*, **34**, L04305, doi:10.1029/2006GL028735.
- Draganov, D., K. Wapenaar, J. Thorbecke, and O. Nishizawa, 2007b, Retrieving reflection responses by crosscorrelating transmission responses from deterministic transient sources: Application to ultrasonic data: *Journal of the Acoustic Society of America*, **122**, EL172, doi:10.1121/1.2794864.
- Fink, M., C. Prada, F. Wu, and D. Cassereau, 1989, Self focusing in inhomogeneous media with time reversal acoustic mirrors: *IEEE Ultrasonics Symposium Proceedings*, **1**, 681–686.
- Fink, M., 1992, Time reversal of ultrasonic fields: basic principles: *IEEE Transactions on ultrasonics, Ferroelectrics and Frequency Control*, **39**, 555–566.
- Fishman, L., J. J. McCoy, and S. C. Wales, 1987, Factorizing and path integration of the Helmholtz equation: numerical algorithms: *Journal of the Acoustic Society of America*, **81**, 1355–1376.
- Fokkema, J. T. and P. M. van den Berg, 1993, *Seismic applications of acoustic reciprocity*: Elsevier.
- Haines, A. J. and M. V. de Hoop, 1996, An invariant embedding analysis of general wave scattering problems: *Journal of Mathematical Physics*, **37**, 3854–3881.
- Larose, E., O. I. Lobkis, and R. L. Weaver, 2006, Coherent backscatter of ultrasound without a source: *Europhysics Letters*, **76**, 422–428.
- Lerosey, G., J. de Rosny, A. Tourin, and M. Fink, 2007, Focusing beyond the diffraction limit with far-field time reversal: *Science*, **315**, 1120–1122.



- Lobkis, O. I. and R. L. Weaver, 2001, On the emergence of the Green's function in the correlations of a diffuse field: *Journal of the Acoustic Society of America*, **110**, 3011–3017.
- Nishizawa, O., T. Satoh, X. Lei, and Y. Kuwahara, 1997, Laboratory studies of seismic wave propagation in inhomogeneous media using laser doppler vibrometer: *Bulletin of the Seismological Society of America*, **87**, 809–823.
- Rayleigh, J. W. S., 1878, *The theory of sound*. Volume II: Macmillan and Co.
- Rickett, J., 1996, The effects of lateral velocity variations and ambient noise source location on seismic imaging by cross-correlation: Report 93, Stanford Exploration Project, 194–151.
- Rickett, J. and J. F. Claerbout, 1996, Passive seismic imaging applied to synthetic data: Report 92, Stanford Exploration Project, 87–94.
- Ruigrok, E., 2006, Global-scale seismic interferometry: numerical validation of the acoustic representation integral: Master's thesis, TU Delft.
- Scherbaum, F., 1987a, Seismic imaging of the site response using microearthquake recordings. Part I. Method: *Bulletin of the Seismological Society of America*, **77**, 1905–1923.
- 1987b, Seismic imaging of the site response using microearthquake recordings. Part II. Application to the Swabian Jura, Southwest Germany, seismic network: *Bulletin of the Seismological Society of America*, **77**, 1924–1944.
- Schuster, G. T., 2001, Theory of daylight/interferometric imaging: tutorial: 63rd Conference and Exhibition, EAGE, Extended abstracts A–32.
- Schuster, G. T., J. Yu, and J. Rickett, 2004, Interferometric/daylight seismic imaging: *Geophysical Journal International*, **157**, 838–852.
- Sivaji, C., O. Nishizawa, and Y. Fukushima, 2001, Relations between fluctuations of arrival time and energy of seismic waves and scale length of

- heterogeneity: an inference from experimental study: *Bulletin of the Seismological Society of America*, **91**, 292–303.
- Slob, E. and K. Wapenaar, 2007, GPR without a source: crosscorrelation and crossconvolution methods: *IEEE Transactions on Geoscience and Remote Sensing*, **45**, 2501–2510.
- Slob, E., D. Draganov, and K. Wapenaar, 2006a, GPR without a source: 11th International Conference on GPR, Ohio State University, Proceedings ANT.6.
- Slob, E., D. Draganov, and K. Wapenaar, 2006b, Let the FCC rule work for you: turning commercial noise into useful data: 11th International Conference on GPR, Ohio State University, Proceedings AIR.5.
- Slob, E., D. Draganov, and K. Wapenaar, 2007, Interferometric electromagnetic Green's functions representations using propagation invariants: *Geophysical Journal International*, **169**, 60–80.
- Snieder, R., 2004, Extracting the Green's function from the correlation of coda waves: a derivation based on stationary phase: *Physical Review E*, **69**, 046610–1–046610–8.
- Snieder, R., 2006, The theory of coda wave interferometry: *Pure and Applied Geophysics*, **163**, 455–473.
- Tang, X. M., Z. Zhu, and M. N. Toksoz, 1994, Radiation patterns of compressional and shear transducers at the surface of an elastic half-space: *Journal of the Acoustic Society of America*, **95**, 71–76.
- Thorbecke, J., 1997, Common focus point technology: Ph.D. thesis, Delft University of Technology.
- Van Manen, D.-J., J. O. A. Robertsson, and A. Curtis, 2005, Modeling of wave propagation in inhomogeneous media: *Physical Review Letters*, **94**, 164301–1–164301–4.
- Van Manen, D.-J., A. Curtis, and J. O. A. Robertsson, 2006, Interferometric modeling of wave propagation in inhomogeneous elastic media using time reversal and reciprocity: *Geophysics*, **71**, SI47–SI60.

- Wapenaar, C. P. A. and A. J. Berkhout, 1989, Elastic wave field extrapolation: Elsevier.
- Wapenaar, C. P. A. and J. L. T. Grimbergen, 1996, Reciprocity theorems for one-way wavefields: *Geophysical Journal International*, **127**, 169–177.
- Wapenaar, K., J. Thorbecke, D. Draganov, and J. Fokkema, 2002, Theory of acoustic daylight imaging revisited: 72nd Annual International Meeting, SEG, Expanded abstracts ST 1.5.
- Wapenaar, K., D. Draganov, J. van der Neut, and J. Thorbecke, 2004a, Seismic interferometry: a comparison of approaches: 74th Annual International Meeting, SEG, 1981–1984.
- Wapenaar, K., J. Thorbecke, and D. Draganov, 2004b, Relations between reflection and transmission responses of 3-D inhomogeneous media: *Geophysical Journal International*, **156**, 179–194.
- Wapenaar, K. and J. Fokkema, 2006, Green's functions representations for seismic interferometry: *Geophysics*, **71**, SI33–SI46.
- Wapenaar, K., E. Slob, and R. Snieder, 2006, Unified Green's function retrieval by cross-correlation: *Physical Review Letters*, **97**, 234301–1–234301–4.
- Weaver, R. L. and O. I. Lobkis, 2001, Ultrasonics without a source: thermal fluctuation correlations at MHz frequencies: *Physical Review Letters*, **87**, 134301–1–134301–4.
- Zhang, J. and D. J. Verschuur, 2002, Elastic wave propagation in heterogeneous anisotropic media using the lumped finite-element method: *Geophysics*, **67**, 625–638.



# Summary

---

## **Seismic and Electromagnetic Interferometry – Retrieval of the Earth's Reflection Response Using Crosscorrelation**

Seismic/Electromagnetic Interferometry is the process of creating new seismic/electromagnetic traces from the crosscorrelation of existing traces. This can be proven using a two-way wavefield or one-way wavefield reciprocity theorem of the correlation type.

In the case of two-way wavefields, it can be shown that in a lossless medium the Green's function, observed at one point due to a source at another point, and its time-reversed version can be retrieved from the crosscorrelation of observed Green's functions at these two points resulting from sources all around the two points. Depending on the Green's function to be retrieved - acoustic, elastodynamic, or electromagnetic case - one should correlate at the two points Green's functions resulting from monopole and dipole sources, from volume force and deformation rate sources, or from electric and magnetic currents, respectively. The retrieved in these ways Green's functions are exact, but for practical applications some simplifications are needed. Assuming that the sources, surrounding the two observation points, lie on a sphere with a sufficiently large radius and that the medium outside this sphere is homogeneous and isotropic it can be shown that the Green's func-

tion between the two points and its time-reversed version can be retrieved from the crosscorrelation of the observed Green's functions at the two points resulting from monopole sources in the acoustic case, from separate sources of P- and S-waves in the elastic case, and from sources of electric current acting in the three directions. The approximations concern mainly the amplitudes, while the phases are handled correctly. In the special case when the medium is bounded from above by a free surface, at the two observation points only measurements, resulting from sources lying along a half sphere bounded from above by the free surface, should be crosscorrelated.

In the case of one-way wavefields, it can be shown that in a lossless medium the flux-normalized acoustic reflection response at the free surface, observed at one point due to a source at another point, and its time-reversed version can be retrieved from the crosscorrelation of observed flux-normalized transmission responses at these two points resulting from sources lying along a plane in the subsurface. In the derivation the evanescent fields have been neglected. In the elastic case, the crosscorrelation of the observed flux-normalized transmission response matrixes will retrieve the reflection response matrix and its time-reversed version between the two points convolved with the free-surface reflection coefficients at the two points. The crosscorrelation result will retrieve correctly the phases as well as the amplitudes.

The above retrieval procedures require that at the observation points are available separate measurements from each of the surrounding sources (in the case of one-way seismic wavefield, separate measurements are required from sources in the subsurface). This is not always possible. If the spectra of the surrounding/subsurface sources are white and uncorrelated, then no separate measurements are required - one just needs to crosscorrelate the observed "noise" fields.

Instead of retrieving the reflection response at the surface from the crosscorrelation of observed noise fields and then migrating them to obtain a subsurface image, one can directly migrate the observed noise fields to image the subsurface. The results from the two approaches are identical.

With the help of 2-dimensional numerical modelling results, the quality is investigated of the retrieval of reflections at the Earth's surface from crosscorrelation of observed two-way seismic and electromagnetic wavefields.

In the seismic case, using separate measurements from subsurface sources

lying at the same depth level and taking the medium below the source level to be homogeneous and isotropic, the reflection response at the surface is kinematically completely retrieved including multiples and, in the elastic case, wave conversions. If the medium below the subsurface sources contains reflectors, the retrieved reflection response will contain nonphysical arrivals. If, though, the subsurface sources are randomly distributed in depth, the ghost events will be strongly suppressed. In the case of crosscorrelation of seismic noise, the complete reflection response is retrieved, but the result looks noisier. When the subsurface source distribution is not optimal, the quality of the retrieved reflections is diminished. Nevertheless, the migration of these retrieved reflections still produces correct subsurface images. In the electromagnetic case, the retrieved reflection response from the crosscorrelation of observed noise fields from sources below as well as above the Earth's surface is investigated.

The retrieval of reflections from crosscorrelation is validated with two measured data examples. The first example shows how reflection arrivals are retrieved from a crosscorrelation of measured ultrasonic transmission responses of inhomogeneous granite. The measured transmission wavefields were excited by separate P-wave as well as S-wave transducers. The second example shows how reflection arrivals are retrieved from crosscorrelation of observed seismic background noise on exploration scale. The background noise was recorded in a desert area.

Deyan Draganov





# Samenvatting

---

## **Seismische en Elektromagnetische Interferometrie – Verkrijgen van de Reflectie Responsie van de Aarde Middels Kruiscorrelatie**

Seismische/Elektromagnetische Interferometrie is het proces van het creëren van nieuwe seismische/elektromagnetische registraties middels de kruiscorrelatie van bestaande registraties. Dit proces kan mathematisch afgeleid worden van tweeweg golfveld of éénweg golfveld reciprociteit theorema van het correlatie type.

In het geval van tweeweg golfvelden, kan aangetoond worden dat in een medium zonder verliezen, de Greense functie, waargenomen op een punt als gevolg van een bron op een ander punt, en de in tijd omgekeerde Greense functie verkregen kunnen worden door de kruiscorrelatie van de waargenomen Greense functies op die twee punten. Afhankelijk van het type Greense functie dat verkregen moet worden – akoestisch, elastodynamisch, of elektromagnetisch – moeten op die twee punten de Greense functies gecorreleerd worden die behoren bij respectievelijk monopool- en dipoolbronnen, volumekracht en deformatiebronnen, of elektrische- en magnetische-stroombronnen. De op die manier verkregen Greense functies zijn exact, maar niet gemakkelijk te gebruiken in de praktijk en ze moeten dus vereenvoudigd worden. Aangenomen dat de bronnen, die de twee punten omringen, op

een bol liggen met een radius die groot genoeg is en aangenomen dat het medium buiten de bol homogeen en isotroop is, kan aangetoond worden dat de Greense functie en de in tijd omgekeerde Greense functie tussen de twee punten verkregen kunnen worden uit de kruiscorrelatie van de op die twee punten waargenomen Greense functies die zijn opgewekt door in het akoestische geval monopool bronnen, in het elastische geval aparte bronnen van P- en S-golven, en in het elektromagnetische geval elektrische stroombronnen actief in de drie richtingen. De benaderingen betreffen voornamelijk de amplitudes terwijl de fases correct worden behandeld. In het speciale geval dat het medium van boven begrensd is door een vrij oppervlak, moeten op de twee meetpunten alleen kruiscorrelaties uitgevoerd worden van metingen van bronnen die liggen op de halve bol onder het vrije oppervlak.

In het geval van éénweg golfvelden, kan afgeleid worden dat in een medium zonder verliezen de flux-genormaliseerde akoestische reflectie responsie op het vrije oppervlak, die wordt waargenomen op één punt en opgewekt door een bron op een ander punt, en de in tijd omgekeerde reflectie responsie verkregen kunnen worden middels de kruiscorrelatie van flux-genormaliseerde transmissie responsies waargenomen op de twee punten. In de afleiding zijn de exponentieel uitdovende velden niet in rekening genomen. In het elastische geval geeft de kruiscorrelatie van de waargenomen flux-genormaliseerde transmissieresponsie matrices de te verkrijgen reflectieresponsie matrix en de in tijd omgekeerde reflectieresponsiematrix tussen de twee punten, geconvolveerd met de reflectiecoëfficiënten van het vrije oppervlak.

De bovengenoemde procedure vereist dat op de waarnemingspunten aparte metingen zijn uitgevoerd van elk van de omliggende bronnen (in het geval van éénweg golfvelden zijn dit de bronnen in de ondergrond). Maar dit is niet altijd mogelijk. Als de spectra van de omliggende/ondergrondse bronnen wit zijn en ongecorreleerd, dan zijn geen aparte metingen nodig – er kunnen direct kruiscorrelaties uitgevoerd worden van de ruis velden.

In plaats van het verkrijgen van de reflectie responsie op het oppervlak middels kruiscorrelaties van waargenomen ruis, gevolgd door migratie om een beeld van de ondergronds te verkrijgen, kan de waargenomen ruis direct gemigreerd worden om dit beeld te verkrijgen. De resultaten van de twee benaderingen zijn identiek.

Aan de hand van de resultaten van tweedimensionale numerieke modelleringen, wordt de kwaliteit onderzocht van de reflecties op het aardoppervlak

verkregen middels kruiscorrelaties van opgenomen seismische of elektromagnetische golfvelden.

In het seismische geval, als er metingen worden gebruikt van ondergrondse bronnen, die op hetzelfde diepteniveau liggen, en als het medium onder het bronniveau homogeen wordt genomen, dan wordt de reflectie responsie op de oppervlak kinematisch volledig verkregen inclusief reverberaties en, in het elastische geval, golfconversies. Als het medium onder het bronniveau reflectoren bevat, dan zal de verkregen reflectie responsie ook niet-fysische aankomsten bevatten. Als de ondergrondse bronnen willekeurig zijn verdeeld in diepte, dan worden de niet-fysische aankomsten onderdrukt. In het geval dat seismische ruis wordt gekruiscorreleerd, dan wordt weer de volledige reflectie responsie verkregen, maar het resultaat bevat meer ruis. Wanneer de ondergrondse brondistributie niet optimaal is, wordt de kwaliteit van de verkregen reflectie responsie verminderd. Niettemin zal het migratieproces van de verkregen reflecties nog steeds de juiste ondergrondse beelden opleveren.

In het elektromagnetische geval wordt de reflectie responsie onderzocht, verkregen middels kruiscorrelaties van waargenomen ruisvelden van bronnen beneden zowel boven het aardoppervlak.

Het verkrijgen van reflecties middels kruiscorrelaties is geverifieerd met twee opgenomen data voorbeelden. Het eerste voorbeeld laat zien hoe reflectie aankomsten werden verkregen middels kruiscorrelaties van waargenomen ultrasone transmissie responsies van inhomogeen graniet. De waargenomen transmissie velden werden opgewekt door zowel P-golf als S-golf transducers. Het tweede voorbeeld laat zien hoe reflectie aankomsten verkregen werden uit kruiscorrelatie van waargenomen seismische achtergrondruis op exploratieschaal. De achtergrondruis werd opgenomen in een woestijn.

Deyan Draganov



# Acknowledgements

---

This research was conducted at the Section of Applied Geophysics and Petrophysics at the Department of Geotechnology, TU Delft. It was a pleasure being part of the section and I want to thank all the colleagues, former and present ones, with whom I worked together during the years. The same thanks for the work we did together to all the colleagues outside the section.

I owe particular thanks to Kees Wapenaar without whom I would not have started and finished this research; the results are as much mine as they are his. Also special thanks to Jan Thorbecke who made the modelling part happen and helped all through my research with everything I asked him for.

To all my friends – to avoid the unavoidable of missing a name, I will not mention any, because I know that when you read this each of you will fill my personal thanks for all the fun!

Karin, thank you for all the support!

And, of course, nothing would have been possible without my mother!

This research was supported by: The Netherlands Research Centre for Integrated Solid Earth Sciences ISES; the Technology Foundation STW, applied science division of the Netherlands Organization for Scientific Research NWO and the technology program of the Ministry of Economic Af-

fairs (grant DTN.4915). The measurement of the Japan laboratory data was partly sponsored by NWO through a travel grant. I would like to thank the Ministry of Petroleum and Mineral Resources of Saudi Arabia, the South Rub Al-Khali Company Limited (SRAK), and Shell Rijswijk for their permission to use the background-noise filed data.

(Thanks to the cacao trees for continuously supplying the basic material for chocolate; the chocolate is an inseparable part of this thesis.)

# Curriculum Vitae

---

## PERSONAL

Name	Deyan Draganov
Date and place of birth	December 31, 1974, Sofia, Bulgaria
Nationality	Bulgarian

## EDUCATION

2002 – 2007	TU Delft, Delft, The Netherlands PhD student. Thesis title: <i>Seismic and Electromagnetic Interferometry – Retrieval of the Earth's Reflection Response Using Crosscorrelation</i>
1999 – 2002	TU Delft, Delft, The Netherlands MSc student in Applied Geophysics
1992 – 1997	University of Mining and Geology, Sofia, Bulgaria MSc student in Applied Geophysics
1989 – 1992	Gymnasium for Mathematics and Informatics, Sofia, Bulgaria Secondary education



**EMPLOYMENT**

- 1999 – 2002 Petrogas Gas-Systems BV, Gouda, The Netherlands  
Gas Engineer
- 1997 – 1999 Gastec Bulgaria, Sofia, Bulgaria  
Gas Engineer